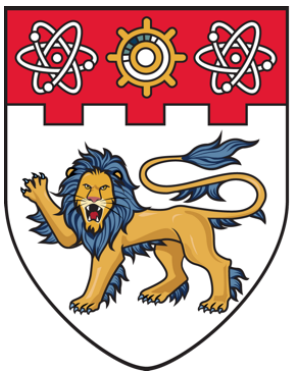

NANYANG TECHNOLOGICAL UNIVERSITY
SINGAPORE

HOW CONVERGENT AND DIVERGENT SIGNALING PATHWAYS ARE MEDIATED BY CARD-CARD INTERACTIONS

Qin Gong

SCHOOL OF BIOLOGICL SCIENCES

2019

HOW CONVERGENT AND DIVERGENT SIGNALING PATHWAYS ARE MEDIATED BY CARD-CARD INTERACTIONS

Qin Gong

SCHOOL OF BIOLOGICAL SCIENCES

A thesis submitted to the Nanyang Technological University in partial fulfilment of the requirement for the degree of Doctor of Philosophy

2019

Statement of Originality

I hereby certify that the work embodied in this thesis is the result of original research done by me except where otherwise stated in this thesis. The thesis work has not been submitted for a degree or professional qualification to any other university or institution. I declare that this thesis is written by myself and is free of plagiarism and of sufficient grammatical clarity to be examined. I confirm that the investigations were conducted in accord with the ethics policies and integrity standards of Nanyang Technological University and that the research data are presented honestly and without prejudice.

Aug. 13, 2019
Date

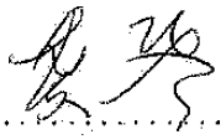
Qin Gong

Supervisor Declaration Statement

I have reviewed the content and presentation style of this thesis and declare it of sufficient grammatical clarity to be examined. To the best of my knowledge, the thesis is free of plagiarism and the research and writing are those of the candidate's except as acknowledged in the Author Attribution Statement. I confirm that the investigations were conducted in accord with the ethics policies and integrity standards of Nanyang Technological University and that the research data are presented honestly and without prejudice.

Aug 13th, 2019 .....
Date

..... Bin Wu

Authorship Attribution Statement

This thesis contains material from one paper published in the following peer-reviewed journal in which I am listed as an author.

Chapter 3 is published as Gong, Q, Long Z, Zhong F, Daniel Teo, Jin Y, Yin Z et al. "Structural basis of RIP2 activation and signaling." *Nature Communications* 9, no. 1 (2018): 4993.

The contributions of the authors are listed as follows:

- Q.G. and B.W. designed experiments.
- Q.G., Z. Long, Z.B., Y.Z., and R.Y. purified protein samples and prepared specimens for EM analysis.
- Q.G., Z.Y., and S.B. collected a preliminary cryo-EM dataset.
- Z. Li optimized the data collection procedures and collected the final high-resolution dataset.
- Y.J. and J.Z. set up the RELION 1.4, beta2.0 and 2.0 and participated in determining the helical symmetry of RIP2–CARD filament and building the initial model.
- B.W. built and refined the final atomic model.
- Z. Long conducted luciferase assays and western blot analysis.
- B.R., F.Z., and D.T. provided resources and conducted transient knockout experiments, as well as related biochemical validations.
- B.W. wrote the paper with input from all other authors.

Chapter 4 is contributed as Gong Qin, Chenrui Xu, Andrew Wong, and Wu Bin.

The contributions of the co-authors are listed as follows:

- Q.G. and B.W. designed experiments.
- Q.G. purified protein samples and prepared grids for EM analysis.
- Q.G. collected several cryo-EM datasets with help from Andrew.
- C.X. set up the RELION beta2.0 and 3.0 for 3D helical reconstruction and determined the parameters of NLRC4–CARD filament for helical symmetry and initial model building.
- C. X. and B.W. obtained and refined the final atomic model.
- C.X. did mutagenesis to validate filament model.

Aug. 13, 2019
Date

Qin Gong

Acknowledgments

Firstly, I thank my family for their upbringing and supports. Without them, I could not have completed my PhD. Mainly, I want to thank my husband, Dr Haoqi Sun, for his company and care.

Secondly, I would like to express my sincere gratitude to my supervisor, Nanyang Asst. Prof. Wu Bin for his guidance and support throughout my PhD journey. His motivation, patience, and immense knowledge impress me and encouraged me to conduct scientific research, from experimental design to publication. I thank my thesis advisory committee, Assoc. Prof. Curtis Davey and Asst. Prof. Luo Dahai, for their guidance and productive discussions during my PhD. I also thank Dr Zhongli Li, Asst. Prof. Shashi Bushan, and Dr Andrew Wong for their advice and help with the cryo-EM data collection. I thank our collaborators Prof. Bruno Reversade and Dr Franklin Chong for their support on the experiments and fruitful collaborations.

Finally, I thank all the current and previous lab members for their help and support during my PhD life; I thoroughly enjoyed working with them in such a warm and happy research environment. I thank Ms Ziqi Long for her excellent technical contribution to the work. I thank my fellow PhD students Mr Yibo Jin, Dr Kelvin Chong Han Chung, Mr Chenrui Xu, Mr Zhaozhi Boo, and Mr Jiawen Zhang for their support and moral support. I especially thank Ms Phuong Thao Huynh for her company and support in my thesis writing and my PhD journal. And I also thank Ms Yaming Zhang, Ms Audrey Chiew, Ms Chai Yoke Tin, Dr Kelvin Chong, and Dr Renliang Yang for all their support and kindness. I thank Jonathan Sigworth for his tremendous help to proofread my thesis.

Table of Contents

List of Figures

List of Tables

List of Abbreviations

Abbreviations	Full name
ALRs	absent-in-melanoma (AIM)-like receptors
AD	activation domain
AIM2	absent in melanoma 2
AMP	adenosine monophosphate
ANA	serological antinuclear antibodies
ANK	Ankyrin repeat
ASC	apoptosis-associated speck-like protein containing a CARD
ATP	adenosine triphosphate
BIR	baculovirus inhibitor repeat
CARD	caspase activation and recruitment domain
CCD	charge-coupled device
CD	Crohn's disease
CDNs	cyclic dinucleotides
cGAMP	cyclic GMP-AMP
cGAS	cyclic GMP-AMP synthase
CLRs	C-type lectin receptors
CRT	carbohydrates recognition domain
Cryo-EM	Cryonic electron microscopy
CTD	carboxyl-terminal domain
CTLD	C-type-lectin-like domain
DAMPs	danger associated molecular patterns
DD	death domain
DED	death effector domain
EAE	experimental autoimmune encephalomyelitis
EOS	early onset disease
ER	Endoplasmic reticulum
GMP	guanosine monophosphate
ID	Intermediate domain
iE-DAP	γ-D-glutamyl-meso-diaminopimelic acid
IFN	type I Interferon
IFI-16	gamma-interferon-inducible protein
IKK	IκB kinase
IRAK2	Interleukin 1 Receptor Associated Kinase 2
IRAK4	Interleukin 1 Receptor Associated Kinase 4
IRF7	interferon regulatory factor 7
ISD	interferon-stimulatory-DNA
KD	kinase domain
LGP2	laboratory of genetics and physiology 2
LPS	lipopolysaccharide
LRRs	leucine-rich repeats
MAPKs	mitogen-activated protein kinases
MAVS	mitochondrial antiviral-signaling protein

MDA5	melanoma differentiation associated factor 5
MDA5	melanoma differentiation-associated protein 5
MDP	muramyl dipeptide
MS	multiple sclerosis
MyD88	myeloid differentiation primary response 88
NAIP	neuronal apoptosis inhibitory protein
NAIP	neuronal apoptosis inhibitory protein
NF-κB	nuclear factor–kappa B
NF-κB	nuclear factor–kappa B
NLRC4	NLR family caspase activation and recruitment domain containing 4
NLRs	NOD-like receptors
NMR	nuclear magnetic resonance
NOD	nucleotide oligomerization domain
NOD1	nucleotide-binding oligomerization domain-containing protein 1
NOD2	nucleotide-binding oligomerization domain-containing protein 2
PAMPs	pathogen-associated molecular patterns
PAMPs	pathogen-associated molecular patterns
PGN	peptidoglycan
poly I:C	polyinosinc-polycytidylic acid
PRRs	pattern recognition receptors
PYD	pyrin domain
RA	rheumatoid arthritis
RAF1	proto-oncogene serine/threonine-protein kinase
RHIM	RIP homotypic interaction motif
RIG-I	retinoic acid-inducible gene I
RIP2	receptor-interacting-serine/threonine-protein kinase 2
RLRs	retinoic acid-inducible (RIG)-I-like receptors
Roc/COR	Ros of complex proteins/C-terminal of Roc domain
SEM	screening electron microscope
sgRNA	Single guide RNA
SLE	systemic lupus erythematosus
STING	stimulator of interferon genes
TAB1/2	TAK 1-binding protein 1/2
TAK1	transforming growth factor-β-activated kinase
TBK1	TANK-binding kinase 1
TEM	transmission electron microscope
TIR	Toll/interleukin-1 receptor
TLRs	Toll-like receptors
TRAF3	tumor necrosis factor receptor (TNFR)-associated factor 3
TRAF6	tumor necrosis factor receptor (TNFR)-associated factor 6
WHD	winged-helix domain

Summary

Immunity is a defense system, with which the host body protects itself against infectious organisms and other invaders. In general, the immune system is classified as an innate immune system and adaptive immune system. In innate immunity, pathogen recognition receptors (PRRs) play an essential role in detecting pathogenic infections and propagating such immune signals to downstream effectors. PRRs are germline-encoded sensors that recognize pathogen-associated molecular patterns (PAMPs) as well as damage-associated molecular patterns (DAMPs). Currently, there are several subfamilies of PRRs, that gerund include C-type lectin receptors (CLRs), RIG-I like receptors (RIRs), NOD-like receptors (NLRs), AIM-like receptors (ALRs), and Toll-like receptors (TLRs) subfamilies, etc. Dysregulation of these PRR- related signaling pathways may lead to defective pathogen detection and, in other cases, autoimmune diseases.

In humans, there are 22 known NLRs classified by their N-terminal functional domain. NLRs include nucleotide-binding and oligomerization domain-containing proteins 1 and 2 (NOD1 and NOD2), and NLR family caspase activation and recruitment domain (CARD) containing protein 4 (NLRC4). NOD1 and NOD2 are also called NLRC1 and NLRC2. They share the same adaptor protein – receptor-interacting-serine/threonine-protein kinase 2 (RIPK2 or RIP2) – that is critical for downstream signaling upon NOD1/2 activation. CARD domains of NOD1 and NOD2 are similar in both function as well as amino acid sequence; however, NOD2 contains two N-terminal CARD domains while NOD1 only has one.

The CARD domain of RIP2 (RIP2-CARD) oligomerizes to form a filamentous structure in responses to activated NOD1-CARD or NOD2-CARD. To investigate the signaling transduction process, the RIP2-CARD oligomeric complex, named RIPosome, was reconstituted and expressed. Its atomic structure was solved by cryo-EM. Finally, the structure of filamentous RIP2-CARD complex was successfully resolved at a near-atomic

resolution of 3.6 Å. With a near-atomic resolution of the structure, the mechanism of how two different CARD domains initiate RIP2 oligomerization from NOD1 and NOD2 was demonstrated. Based on the experimental data from crucial residues on CARD-CARD interfaces, the mechanism was elucidated with two different upstream signals activating RIP2 in a convergent way.

In this study, another classic NLR (NLRC4-CARD) was found to form filamentous oligomers upon activation, with the filament structure solved by a similar method as that for RIP2-CARD filament at 3.3Å resolution. The atomic-resolution structure provides important information about the functional roles of full-length NLRC4 in vivo and reveals the importance of filamentous oligomers in immune signals transduction. NLRC4 directly triggers ASC and Caspase-1 activation for different cellular activities – a typical example of a divergent signaling pathway in innate immunity.

Chapter 1. Background

1.1. History of Pattern Recognition Receptors (PRRs)

The vertebrate immune system has had to continually evolve due to the constant necessity of eliminating invading pathogens from hosts (Jerne 1973, Janeway Jr 1992, Banchereau and Steinman 1998). In this evolution, two immune systems were generated, the innate and adaptive immune system, to ensure the efficient detection and removal of invading microorganisms (Janeway 1989, Medzhitov and Janeway Jr 1997, Medzhitov and Janeway Jr 2000).

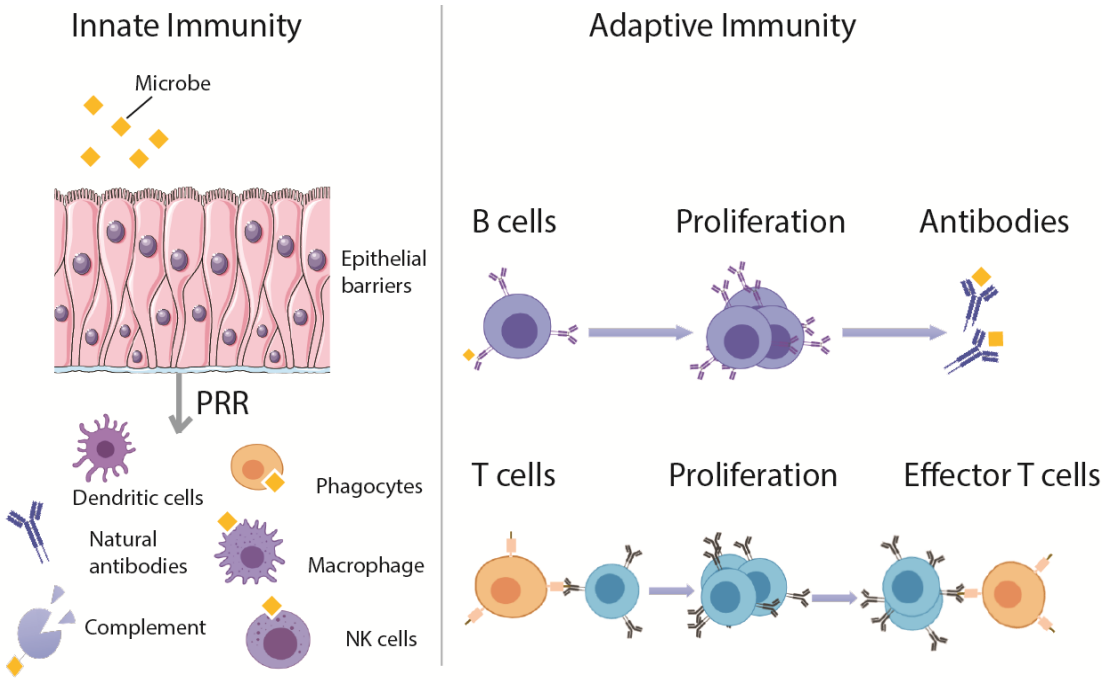

Figure 1.1. The immune responses of innate immunity and adaptive immunity. Microbes are first detected by PRRs located in the epithelial barriers, which then propagate to different effector cells, including dendritic cells, macrophages, and complement cells. Cells in innate immunity present antigen and activate both B cells and T cells for further specific immune responses.

Adaptive immunity is defined as specific immune responses where somatic recombination generated B/T cells produce specific antibodies aiming at bacteria ligands from harmful microbes (Medzhitov, Preston-Hurlburt et al. 1997, Capra, Janeway et al. 1999) (Figure 1.1). During this process, memory cells are generated and detect the same antigens in the host for fast immune responses, called immunologic memory (Demkowicz, Littaua et al. 1996). Compared to adaptive immunity, less attention had been paid in early studies to innate immunity, also known as nonspecific immunity. Innate immunity acts as the first line of defence for the host against infectious microbes. In addition, molecules in the innate immune system also detect and present a stimulus to immune cells involved in the acquired immunity, resulting in the activation of the adaptive immune system (Medzhitov and Janeway Jr 1997, Medzhitov and Janeway Jr 2000). The modern concept of innate immunity was first proposed in 1989 (Janeway 1989). The studies by Charles Janeway demonstrated that innate immunity played an important role in discriminating between self and foreign antigens, as well as building specificity for antigen recognition (Janeway Jr 1992, Medzhitov and Janeway Jr 2000). This discrimination of innate immunity relies on a family of evolutionarily conserved receptors, called pattern recognition receptors (PRRs) (Gordon 2002, Kawai and Akira 2010). PRRs recognize PAMPs and DAMPs from infectious pathogens, which are quite different from the host, allowing for the immune response (Janeway 1989). The first signaling receptor in innate immunity was discovered in 1996 from *Drosophila melanogaster*. In the paper, it was elucidated that the generation of antimicrobial molecules relied on the activation of a signal cascade mediated by Toll (Lemaitre, Nicolas et al. 1996). Subsequent studies identified a homolog gene of Toll in humans and proposed the first mammalian signal pathway mechanism for innate immunity. The mechanism is that bacterial lipopolysaccharide (LPS) triggers the detection and activation of the Toll-like receptor to induce host defense (Medzhitov, Preston-Hurlburt et al. 1997, Akira and Takeda 2004).

Table 1 Properties of Pattern Recognition Receptors

PRRs	Localization	Ligand	Origin of the Ligand
cGAS-STING			
cGAS	Plasma membrane	dsDNA	Self
STING	Endolysosome	CDNs	Self
TLR			
TLR1	Plasma membrane	Triacyl lipoprotein	Bacteria
TLR2	Plasma membrane	Lipoprotein	Bacteria, viruses, parasites, self
TLR3	Endolysosome	dsRNA	Virus
TLR4	Plasma membrane	LPS	Bacteria, viruses, self
TLR5	Plasma membrane	Flagellin	Bacteria
TLR6	Plasma membrane	Diacyl lipoprotein	Bacteria, viruses
TLR7	Endolysosome	ssRNA	Virus, bacteria, self
TLR8	Endolysosome	ssRNA	Virus, bacteria, self
TLR9	Endolysosome	CpG-DNA	Virus, bacteria, protozoa
TLR10	Plasma membrane	Lipoprotein	Bacteria
TLR11	Endolysosome	Profilin-like molecule	Protozoa,Bacteria
TLR12	Endolysosome	Profilin	Bacteria
TLR13	Endolysosome	rRNA	Bacteria
CLR			
Dectin-1	Plasma membrane	β-Glucan	Fungi
Dectin-2	Plasma membrane	β-Glucan	Fungi
MINCLE	Plasma membrane	SAP130	Fungi, self
ALR			
AIM2	Cytoplasm	dsDNA	Self
IFN16	Nucleus	dsDNA	Self
RLR			
RIG-I	Cytoplasm	dsRNA, 5'triphosphate dsRNA	RNA viruses, DNA virus
MDA5	Cytoplasm	Long dsRNA	RNA viruses
LGP2	Cytoplasm	Unknown	RNA viruses
NLR			
NOD1	Cytoplasm	iE-DAP	Bacteria
NOD2	Cytoplasm	MDP	Bacteria
NLRC4	Cytoplasm	Flagellin	Bacteria

With the improvement of genome-sequencing technology, more genes associated with PRRs were identified and organized into different groups according to their locations and structures (Akira and Takeda 2004).

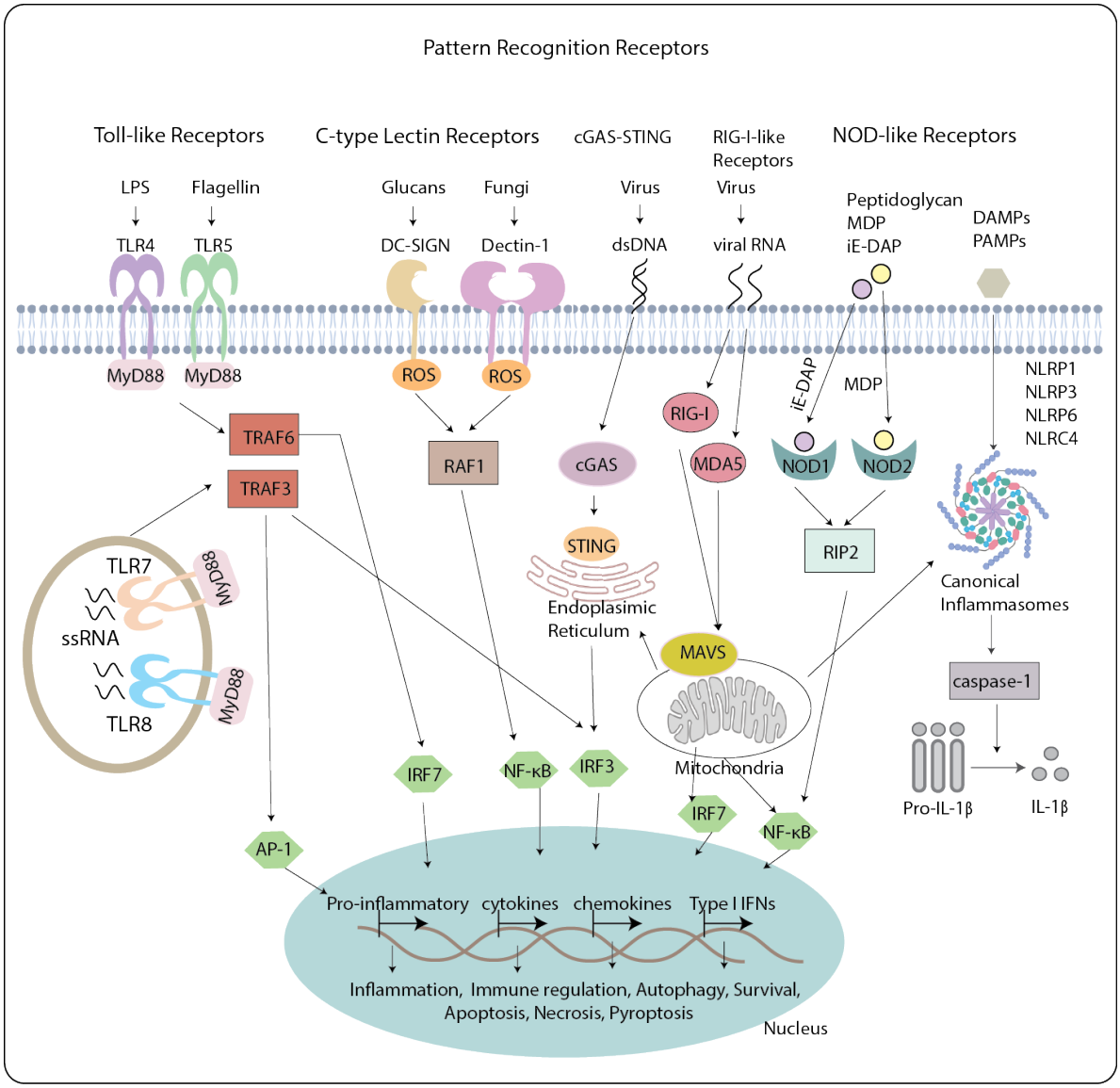

Figure 1.2. An overview of pattern recognition receptors. Several microbial antigens are detected by TLRs, CLRs, NLRs, RLRs, and cGAS-STING to induce immune responses. Different events are performed, including apoptosis, necrosis, pyroptosis, and the production of cytokines.

Until now, PRRs were well known for containing different types of receptors, including Retinoic acid-inducible (RIG)-I-like receptors (RLRs), NOD-like receptors (NLRs), Toll-like receptors (TLRs), C-type-lectin receptors (CLRs), and absent-in-melanoma (AIM)-like receptors (ALRs) (Meylan, Tschopp et al. 2006) (Table 1).

The most crucial role of PRRs is to recognize PAMPs and DAMPs, which further propagates immune signals and induces the activation of downstream signaling pathways for inflammatory responses (Medzhitov and Janeway Jr 2000, Bianchi 2007). PRRs are involved in detecting invading pathogens as well as endogenous danger or stress signals (Medzhitov and Janeway Jr 2000) (Figure 1.2). Both types of signals can stimulate inflammatory responses by the production of cytokines dependent on mitogen-activated protein kinases (MAPKs) and nuclear factor–kappa B (NF-κB) (Kopp and Ghosh 1995, Seger and Krebs 1995). These signaling pathways improve the importance of PRRs in host defence from harmful microbes and inflammatory diseases (Capra, Janeway et al. 1999, Li and Verma 2002, Brown and Mayer 2007). In humans, these PRRs are prevalently expressed in dendritic cells, macrophages, as well as in other non-professional immune cells (Gordon 2002).

cGAS – STING pathway

In addition to classic PRRs, there are other cytoplasmic DNA sensors, such as cyclic GMP-AMP (cGAMP) synthase (cGAS), that also possess inflammatory responses in innate immunity (Xiao and Fitzgerald 2013). In the past few years, it has been proposed that DNA-sensing PRRs were upstream of stimulator of interferon genes (STINGs), which contain four transmembrane helices and a globular C-terminal domain (CTD) (Yin, Tian et al. 2012). The tail of the CTD domain maintains the auto-inhibited state of STINGs and facilities the interaction with downstream kinases (Yin, Tian et al. 2012). Although several potential receptors have been linked to regulating STING activation, including Gamma-interferon-inducible protein 16 (IFI16), the mechanism of how STINGs involve a DNA recognition pathway is unclear until Chen lab reported the discovery of cGAS (Unterholzner and Bowie 2011, Wu, Sun et al. 2013). It is reported that cGAS directly binds to DNA and produces an endogenous second-messenger, cGAMP, by combining GTP and ATP (Wu, Sun et al. 2013). cGAMP was demonstrated to bind to STING and subsequently activate type I interferon

pathway (Sun, Wu et al. 2013, Wu, Sun et al. 2013) (Figure1.3).

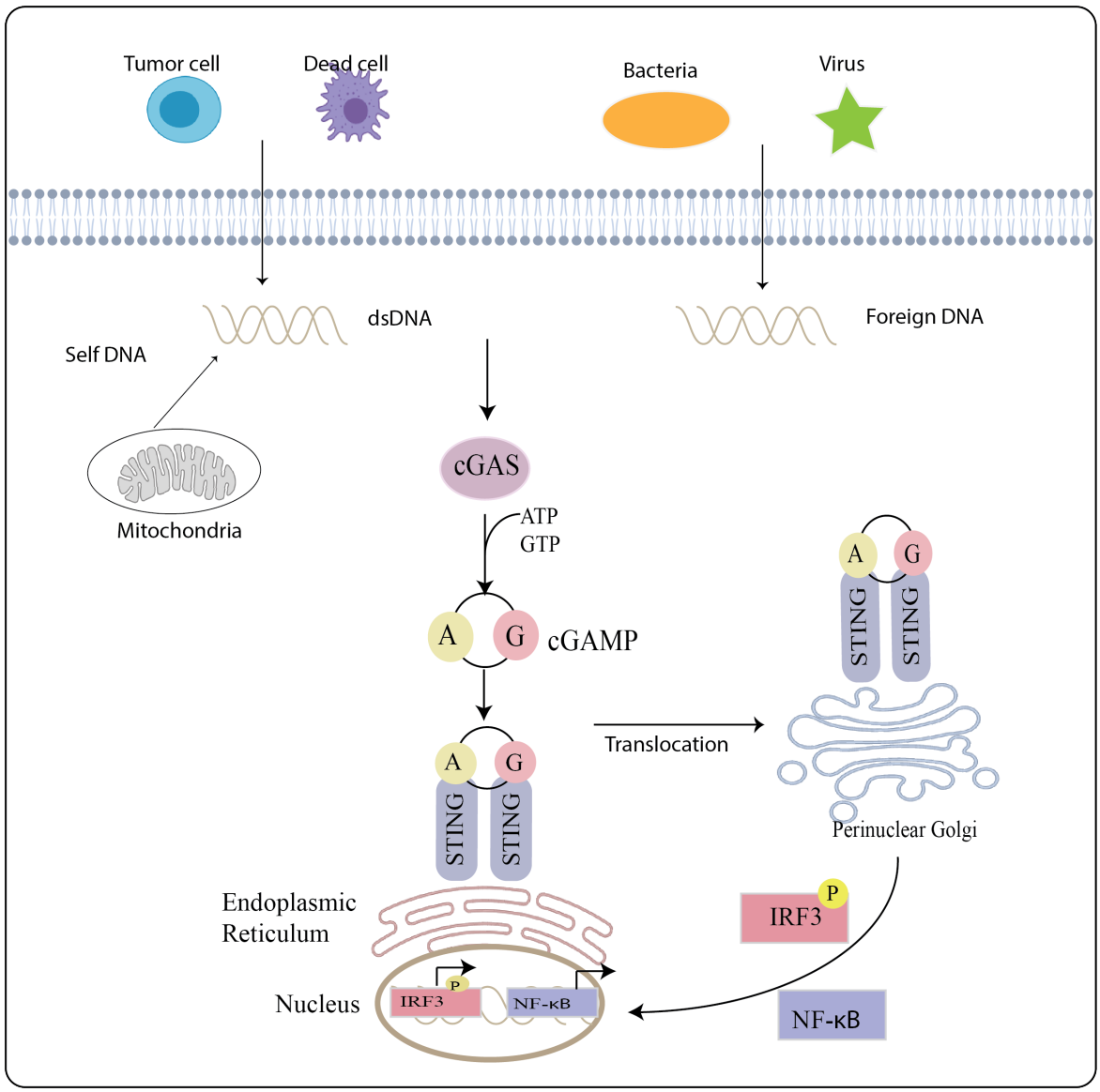

Figure 1.3. The cGAS-STING pathway of cytosolic sensing. cGAS can detect different sources of dsDNA from damaged mitochondria, dead cells, and viruses. Activated cGAS catalyzes the synthesis of 2'3'-cGAMP, which further binds to the ER adaptor STING and traffics to the ER-Golgi intermediate compartment and the Golgi apparatus. STING then triggers downstream immune signals to release inflammatory molecules. IRF7: interferon regulatory factor 7; TBK1: TANK-binding kinase 1; IKK: IκB kinase.

cGAS consists of three domains, including two DNA-binding domains and a

nucleotidyltransferase domain (Sun, Wu et al. 2013, Zhang, Wu et al. 2014). With the stimulation of microbial DNA, DNA-binding domains of cGAS directly bind to DNA and cause cGAS to undergo a conformational change from an auto-inhibited state to an active state (Zhang, Wu et al. 2014). Activated cGAS is then exposed with an active site to recruit ATP and GTP for catalytic synthesis of cyclic cGAMP (Zhang, Wu et al. 2014)(Figure 1.3). The cGMAP contains two phosphodiester bonds that facilitate the cyclization of cGMAP, producing cGAMP isomer. This isomer serves as an intermediate effector to be associated with the endoplasmic-reticulum (ER) membrane adaptor STING (Sun, Wu et al. 2013, Wu, Sun et al. 2013, Zhang, Wu et al. 2014). The whole complex was transported and exhibited binding with the Golgi apparatus (Dobbs, Burnaevskiy et al. 2015).

In this process, STING recruits kinases, including TBK1 and IKK through its N-terminal domain (Dobbs, Burnaevskiy et al. 2015). TBK1 further phosphorylates the interferon transcription factor (IRF3) (Dobbs, Burnaevskiy et al. 2015). Phosphorylated IRF3 are dimerized and translocated into the cell nucleus (Xiao and Fitzgerald 2013). Meanwhile, IKK activates downstream NF-κB pathway, as shown in Figure 1.3. These transcriptional factors function together to induce the expression of inflammatory chemokines and interferons for immune responses (Nanson, Rahaman et al. 2018).

Toll-like Receptors

Toll-like receptors (TLR) were the first PRRs to be found and studied in detail (Medzhitov and Janeway Jr 2000). In the beginning, researchers used *Drosophila* to identify developmental mutations until the first discovery of the Toll gene in *Drosophila* by German scientists (Beck and Habicht 1996). Later, Toll was identified as a mutation site for bizarre-looking flies and establishing dorsoventral polarity in the development of embryogenesis (Hashimoto, Hudson et al. 1988). In 1996, a paper showed that *Drosophila* hosts with

defective Toll proteins were sensitive to fungal infections, supporting that Toll genes were required in the insect immune process to produce antifungal molecules (Lemaitre, Nicolas et al. 1996). Alignment with the sequence of Toll protein, other homology and similar proteins were identified and classified as Toll-like receptors based on the database in the Human Genome (Medzhitov, Preston-Hurlburt et al. 1997, Rock, Hardiman et al. 1998).

To further ensure and confirm the importance of TLRs in innate immunity, mouse models were adopted to provide evidence for the functional assay of TLRs (Poltorak, He et al. 1998). In 1998, some scientists delicately proved that mice with a loss-of-function mutation of TLR4 were resistant to sepsis induced by LPS. In this way, TLR4 was identified and confirmed as a receptor to detect bacterial LPS and activate immune responses (Poltorak, He et al. 1998). Until now, 10 TLRs (TLR1-TLR10) in humans and 13 TLRs (TLR1-TLR13) in mice have been identified by database searches (De Nardo 2015). TLRs localize to the plasma membrane or intracellular compartments, such as the endosome, ER, lysosome, or endolysosome, and they detect lipid, nucleic acid, protein and lipoprotein PAMPs (De Nardo 2015). Based on their localization, they are classified into two subfamilies: cell surface TLRs and intracellular TLRs (Pandey, Kawai et al. 2015). Cell surface TLRs include TLR1, TLR2, TLR4, TLR5, TLR6, and TLR10. Intracellular TLRs include TLR3, TLR7, TLR8, TLR9, TLR11, TLR12, and TLR13 (Kawai and Akira 2010).

Cell surface TLRs mainly detect membrane microbial membrane components including lipids, lipoproteins, and proteins. TLR1/2/6 recognizes a wide variety of PAMPs including lipoprotein, peptidoglycan, and lipoteichoic acid (Kawai and Akira 2010) (Table 1). TLR4 detects bacterial lipopolysaccharide (LPS). TLR5 recognizes bacterial flagellin (Kawai and Akira 2010) (Figure 1.4). Human TLR10 collaborates with TLR2 to recognize ligands from listeria (Regan, Nally et al. 2013).

Intracellular TLRs can detect nucleic acids from bacteria, viruses, and damaged cells (Blasius and Beutler 2010). TLR3 recognizes viral dsRNA, small interfering RNAs, and RNAs from damaged cells (Blasius and Beutler 2010, De Nardo 2015, Pandey, Kawai et al. 2015).

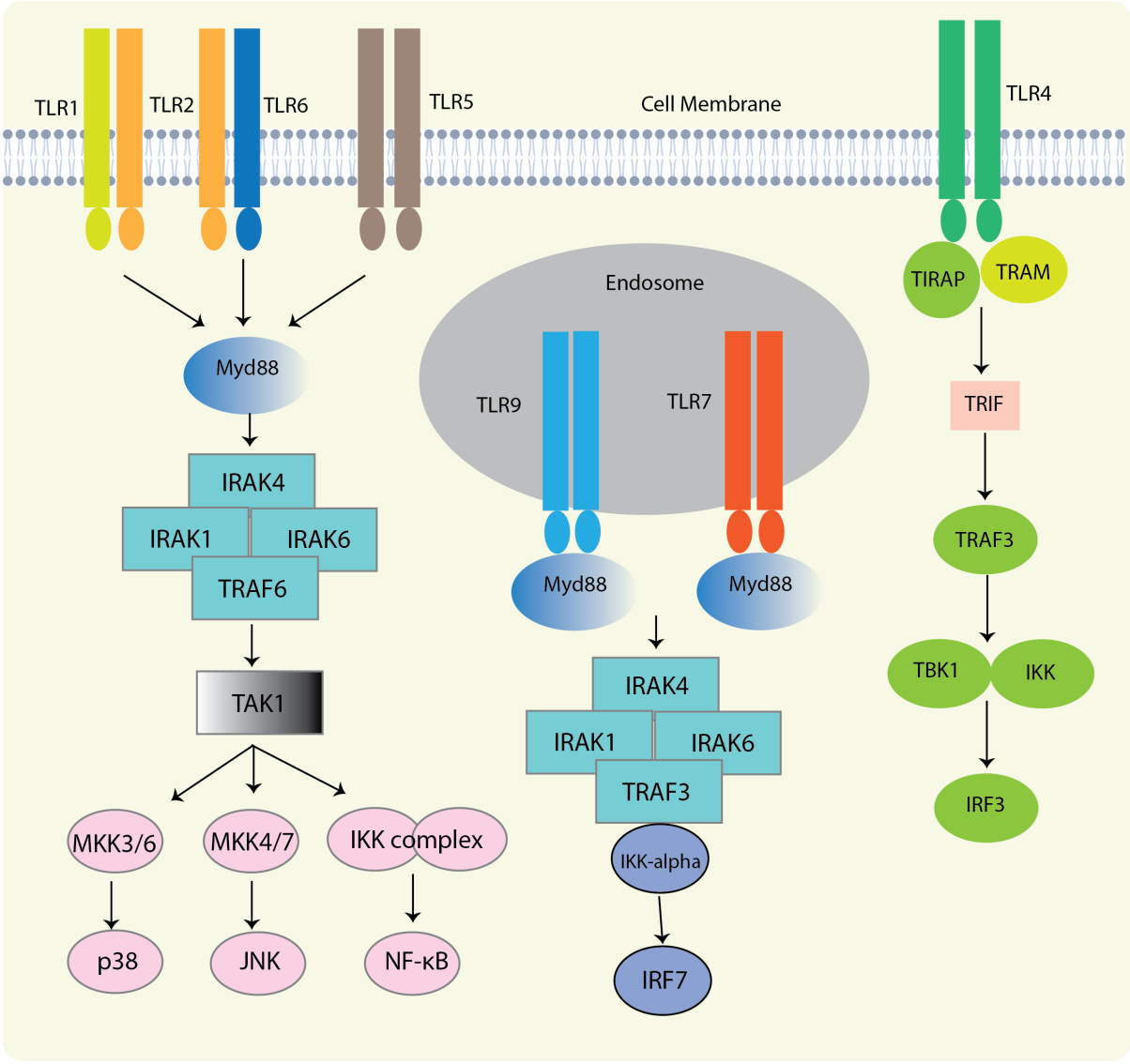

Figure 1.4. TLR signaling cascade. Activation of TL1, TLR2, TLR5, and TLR6 on the cell surface or TLR7/9 in endosomes leads to the recruitment of MyD88 and initiation of the MyD88-dependent signaling pathways. TLR4 triggers the activation of TRAF3, leading to the activation of important pro-inflammatory transcription factors, NF-κB p38 and JNK for cytokine production.

TLR7 recognizes ssRNAs from viruses (De Nardo 2015). Human TLR8 responds to viral and

bacterial RNA (Guiducci, Gong et al. 2013). TLR9 detects bacterial and viral DNA that is rich in unmethylated CpG-DNA motif (Coban, Igari et al. 2010); ectodomains of TLR7 and TLR9 have to be cleaved in the endolysosome to recognize microbial ligands (Ewald, Lee et al. 2008). TLR11 recognizes flagellin or a profiling-like molecule from bacteria at the location of endolysosome (Yarovinsky, Zhang et al. 2005). Similar to TLR11, TLR12 also recognizes profilin from *T.gondii* (Koblansky, Jankovic et al. 2013). TLR13 recognizes bacterial 23S rRNA (Li and Chen 2012).

Transmembrane domains are the fundamental structures of TLRs, aligned with their location in the cell membranes, as well as those of endosomes, lysosomes, and plasma (Medzhitov 2001). After TLRs are stimulated by invading pathogens, they quickly recognize and integrate signals to induce immune responses in host cells (Wu, Su et al. 2017). In this process, stimulated TLRs first undergo conformational change and then dimerize to establish a signal platform to recruit more effectors, such as myeloid differentiation primary-response protein 88 (Myd88) (Deguine and Barton 2014). Activated Myd88 recruits more downstream adaptors, including IL-1R-associated kinase 2/4 (IRAK2/4), to form signaling complexes that further magnify and propagate signals with the help of transforming growth factor-β-activated kinase (TAK1), TAK 1-binding protein 1/2 (TAB1/2), and tumor-necrosis-receptor-associated-factor 6 (TRAF6) (De Nardo 2015). During this process, dimerized TLRs recruit Myd88 to allow for the association and phosphorylation of IRAK1 or IRAK4 (De Nardo 2015). Later, TRAF6 is recruited by phosphorylated IRAKs to form signaling complexes that dissociate from IRAK4. Dissociated complexes move to the plasma membrane and bind with TAK1, TAB1/2 to form new inflammatory complexes (De Nardo 2015). The complexes are translocated to cell cytoplasm for binding with ubiquitin ligases, leading to TRAF6 ubiquitination and TAK1 activation (Pandey, Kawai et al. 2015, Rogero and Calder 2018). Activated TAK1 contributes to the translocation of NF-κB to the nucleus, allowing the

production of immune molecules (Akira and Takeda 2004, De Nardo 2015).

C-type lectin receptors

Since the 1860s, C-type lectins (CLRs) have been gradually understood, as when lectins from snake venom were first described (Kilpatrick 2002). Later, researchers suggested that lectins should be classified into different groups. The C-type lectin group is organized with Calcium-dependent lectins, sharing similar structural similarity with asialoglycoprotein receptors (Drickamer 1988). More CLRs have been found and classified into 17 groups based on their difference in structure and phylogeny. CLRs prefer binding with carbohydrates due to their evolutionarily conserved residues present on carbohydrates recognition domain (CRT) and C-type-lectin-like domain (CTLD) (Zelensky and Gready 2005, Hoving, Wilson et al. 2014). CLRs are further divided into three subfamilies based on their roles in different signaling pathways: active CLRs with ITAM domains, inhibitory CLRs with ITIM domains, and CLRs without clear ITAM and ITIM domains (Hoving, Wilson et al. 2014). Like PRRs, CLRs can detect different kinds of microbes, including bacteria, Helminths, protozoa, viruses, and fungi (Zelensky and Gready 2005). Activated CLRs participate in immune responses by indirect signaling and direct signaling (Zelensky and Gready 2005). Macrophage-inducible C-type lectin, for example, is an indirect signaling CLR associated with ITAM-containing proteins such as DAP12 (Hoving, Wilson et al. 2014). For direct signaling, Dectin-1 and DNGR-1 are two good examples involved in direct signaling by CLR tails in the cytoplasm that lead to the activation several immune effectors, including NF-κB, MAPK, and even some immune responses (Hoving, Wilson et al. 2014).

In innate immunity, the best known CLR is Dectin-1, which is responsible for the detection of fungal infection (Zelensky and Gready 2005). Ligand β-glucan from fungi is recognized by Dectin-1 and activates multiple signaling pathways by its signaling domain located at the cell

cytosol. (Dambuza and Brown 2015). The infectious rate of colitis, induced by dextran sodium sulphate, was significantly increased for mice lacking Dectin-1 when they were exposed to specific fungal species (Dambuza and Brown 2015).

AIM-like receptors (ALRs)

ALRs were first discovered in mice, functioning as genes to induce the production of interferons (Kingsmore, Snoddy et al. 1989). Until recent years, ALRs were characterized by a systematic proteomic screen for direct binding with DNA (Bürckstümmer, Baumann et al. 2009). In this screening, AIM2 was known to bind to cytoplasmic double-stranded DNA and recruit downstream adaptors for the inflammasome formation involving ASC, which is similar to the activation mode of NLRs (Bürckstümmer, Baumann et al. 2009). Since then, several ALRs have been identified as containing a DNA-binding HIN domain and a PYD (Albrecht, Choubey et al. 2005, Gray, Winship et al. 2016). One ALR has been previously discovered in cows, four in humans (PYHIN1, IFI16, MNDA, and AIM2) and thirteen in mice (Gray, Winship et al. 2016). According to the results of phylogenetic analysis, there is no homology in mammalian ALRs except for AIM2 (Brunette, Young et al. 2012). Although AIM2 is described as a crucial DNA sensor that activates inflammasome, other ALR receptors remain unclear in their functions (Brunette, Young et al. 2012, Gray, Winship et al. 2016). Multiple studies support that ALRs are essential in the activation of the interferon-stimulatory-DNA (ISD) pathway (Gray, Winship et al. 2016). Some ALRs are reported to bind with viral DNA, according to the results fron immunoprecipitation experiments (Brunette, Young et al. 2012). The IFN expression level in mice is significantly decreased with defective ALRs in the presence of microbes (Li, Chen et al. 2013). However, other studies have shown that mouse ALRs were unnecessary for the production of IFN in response to pathogenic DNA by the generation of all $ALR^{-/-}$ defective mice (Gray, Winship et al. 2016). More research studies need to be conducted to explore the functions of ALR

receptors.

RIG-I-like Receptors

RIG-I-like receptors (RLRs) were first identified as genes associated with leukemia cells (Sun 1997). The following studies characterized a gene named retinoic acid-inducible gene I (RIG-I), which was associated with a disease called porcine reproductive and respiratory syndrome (Zhang, Wang et al. 2000). This study demonstrated that the RIG-I gene was possibly related to viral infections (Zhang, Wang et al. 2000). Four years later, a research group showed that RIG-I gene was associated with the activation of IRF-regulated reporter gene in the response of double-strand RNA and polyinosinc-polycytidylic-acid (poly I: C) (Yoneyama, Kikuchi et al. 2004). It was confirmed that RIG-I participated in the regulation of antiviral immunity to remove invading viruses (Yoneyama, Kikuchi et al. 2004). Presently, it is well established that RIG-I belongs to a family of RNA helicase and functions as a viral RNA sensor for the host surveillance to detect viral infection (Onoguchi, Yoneyama et al. 2011). The mammalian genome encodes the other two genes related to RIG-I, including laboratory-of-genetics-and-physiology 2 (LGP2) and melanoma-differentiation-associated-factor 5 (MDA5) (Yoneyama, Kikuchi et al. 2005).

The architecture of RIG-I contains three parts: a CTD domain, a central helicase domain, and two amino-terminal CARD domains (Figure 1.5). The helicase domain of RIG-I is required to detect viral infections, while RIG-I tandem CARD domains are responsible for the signals propagation (Yoneyama and Fujita 2009) (Figure 1.5). The previous study showed that adenosine triphosphate (ATP) binds with the lysine residue located in the helicase domain of RIG-I. In this case, RIG-I forms a negative inhibitor once lysine is substituted for alanine, which indicates that ATP is required to activate RIG-I induced signals (Yoneyama and Fujita 2009). MDA5 was identified by subtraction hybridization in human melanoma cells to be

induced during differentiation and apoptosis (Kang, Gopalkrishnan et al. 2002). The amino acid similarity of MDA5 and RIG-I takes up 23% of the N-terminal 2CARD domains and 35% of CTD domain (Yoneyama, Kikuchi et al. 2005). Functional analysis demonstrated that

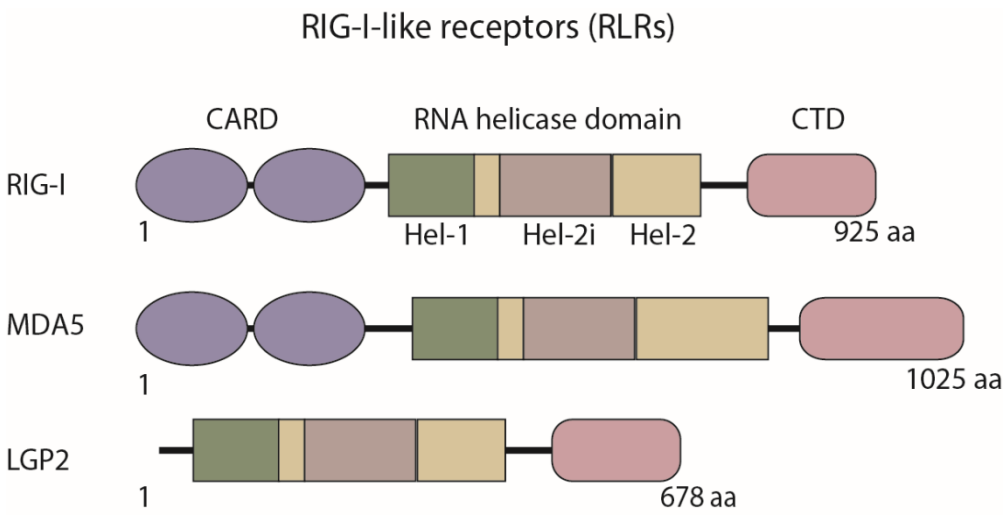

Figure 1.5. Architecture of RLR receptors including Retinoic-acid inducible gene I (RIG-I), melanoma differentiation-associated 5 (MDA5) and laboratory of genetics and physiology 2 (LGP2). All three RLRs contains a C-terminal domain (CTD) and an RNA helicase domain. RIG-I and MDA5 consist of two N-terminal CARD domains to recruit downstream adaptors.

MDA5 shares a similar function to RIG-I as a virus defender, while they recognize different kinds of viruses (Yoneyama, Kikuchi et al. 2005). RIG-I prefers to recognize dsRNAs with blunt ends or ssRNA hairpins, which can both be found in Mengo virus, encephalomyocarditis virus, and Theiler's virus (Yoneyama and Fujita 2009). For MDA5, long-duplex RNAs are usually preferred, particularly the genome and DNA replication intermediates of dsRNA viruses, such as Sendai virus, Newcastle disease virus, and respiratory virus (Yoneyama and Fujita 2009). LGP2 belongs to RLRs located in the gene locus of STAT3/5 by computational analysis (Cui, Li et al. 2001). LGP2 consists of only a helicase domain and CTD. The helicase domain of LGP2 has an amino acid sequence similarity of 41% to RIG-I and 31% to MDA5, respectively (Yoneyama and Fujita 2009).

According to previous studies, LGP2 acts as an inhibitor to regulate the signaling pathways mediated by MDA5/RIG-I (Rothenfusser, Goutagny et al. 2005, Komuro and Horvath 2006). Studies demonstrated that LGP2-deficient mice were resistant to the viral infection caused by vesicular stomatitis virus (Venkataraman, Valdes et al. 2007). This indicates that LGP2 cooperates with MDA5 or RIG-I to sense viral RNA under physiological conditions (Kato, Takahasi et al. 2011).

RLRs are prevalently distributed in many tissues and a variety of cell types in which RLRs perform their functions as innate immunity receptors. (Yoneyama, Kikuchi et al. 2005). During this process, RLRs participate in signaling pathways to mediate the transcriptional upregulation of type I interferons (IFNs). MDA5 and RIG-I share similar domain architecture and possess a similar function in innate immunity. They both consist of two N-terminal CARD domains that can recruit MAVS by homotypic CARD-CARD interactions for activation of the antiviral signaling pathway (Wu and Hur 2015).

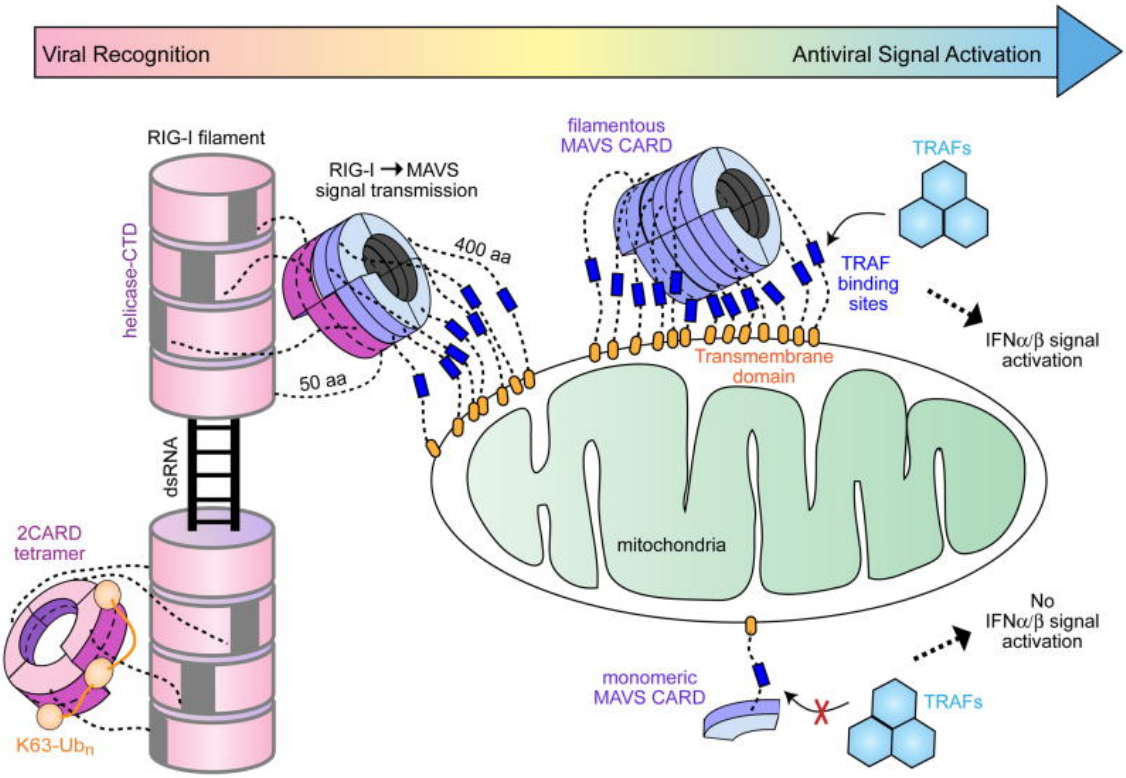

Figure 1.6. A model of immune responses participated by RIG-I and MAVS, adapted from (Wu, Peisley et al. 2014). In the presence of dsRNA, the helicase-CTD domain of RIG-I polymerizes to filamentous oligomers. These oligomers bring together RIG-I CARD into proximity to form a tetramer, stabilized by K63-Ub_n. The RIG-I CARD tetramer serves as are a helical template to induce the formation of MAVS CARD filament. MAVS CARD filament with multiple TRAF binding sites recruits TRAF molecules and activate downstream signaling pathway.

To examine how RIG-I induces the immune response, Wu and his colleagues proposed a model of how RLRs mediate signal activation (Figure 1.6) (Wu, Peisley et al. 2014). With ATP existence, the helicase-CTD domain of RIG-I recognizes viral dsRNA by detecting its 5'ppp and blunt end, which makes RIG-I form active oligomers (short filaments) along the length of dsRNA during ATP hydrolysis (Wu, Peisley et al. 2014). In this process, short filaments tightly put together 2CARD domains of RIG-I. Due to the long linker (50 amino acids) between the RIG-I CARD domain and the core filament, this can induce the formation of a RIG-I CARD tetramer (Wu, Peisley et al. 2014). Furthermore, the tetramer can be stabilized by K63-Ubn to connect adjacent CARDs and wrap around the tetramer (Wu, Peisley et al. 2014). According to previous structural data, the first helical turn is organized and formed by the first CARD domain of RIG-I, then subsequently extended and tightly stabilized by the second CARD (Wu and Hur 2015). The helical structure of RIG-I CARD domains allows the tetramer to act as a helical template to recruit CARD domain from downstream adaptor MAVS to form a long filament. (Wu, Peisley et al. 2014, Wu and Hur 2015). An amino acid linker anchors MAVS filaments to mitochondria. Multiple TRAF binding sites can be generated when MAVS CARD filaments are formed, recruiting TRAF molecules for the activation of IFNα/β pathways (Wu, Peisley et al. 2014).

NOD-like Receptors

NOD-like receptors (NLRs) were the first PRRs found in plants, where they act as essential molecules to fight against microbial and parasite pathogens (Jones and Dangl 2006). Since then, other homologs were discovered and identified in many species, including sea urchins (Hibino, Loza-Coll et al. 2006). This finding in sea urchins pushed the evolutionary origin of NLRs forward to an ancient age, with NLRs potenially in basal metazoans (Inohara and Nuñez 2001). The evolutionary conservation of NLRs from primitive organisms to vertebrates demonstrates that NLRs are important for host defence (Inohara and Nuñez 2001). In vertebrates, NLRs originated in teleost fish (Laing, Purcell et al. 2008). Until now, 23 NLR genes have been found in humans and more than 34 NLR homologies are present in mice (Franchi, Warner et al. 2009) (Figure 1.7). Nucleotide oligomerization domain (NOD) is highly conserved in all NLRs and is prevalent among intracellular PRRs (Kim, Shin et al. 2016). The architecture of NLRs consists of three different functional domains: (1) an amino-terminal effector binding domain providing protein-protein interaction sites including activation domain (AD), baculovirus inhibitor repeat (BIR), pyrin domain (PYD), caspase activation recruitment domain (CARD), and X (function not defined); (2) an evolutionarily conserved NOD domain required for self-oligomerization and binding with nucleotides; and (3) a batch of C-terminal leucine-rich repeats (LRR) domain, recognizing conserved pathogenic ligands to regulate NLR activity (Franchi, Warner et al. 2009, Kim, Shin et al. 2016) (Figure 1.7). NLRs have functional domains in the N-terminus (Chen, Shaw et al. 2009). Based on different types of functional domains in the N-terminus, NLRs are divided into four subfamilies including NLRP (PYD containing NLR), NLRB (BIR containing NLR), NLRC (CARD containing NLR), and NLRX (unknown domain-containing NLR) (Ting, Lovering et al. 2008). NLRX1 is one NLR example that is located on mitochondria (Inohara and Nuñez 2001). Different N-terminal domain regulates different cellular functions (Inohara

and Nuñez 2001). The majority of NLRs contain CARD or PYD, and more than 50% are present in humans or mice.

The NLRC subfamily includes NLRC1 (NOD1), NLRC2 (NOD2), NLRC3 (NOD3), NLRC4, NLRC5, and NLRX1 (Figure 1.5). NLRC subfamily members are classified by their common characteristics and N-terminal CARD domains, which were associated with the recruitment of caspase1 or kinase to modulate signalling pathways in innate immunity (Kim, Shin et al. 2016). NLRC3, NLRC5, and NLRX1, contain an undefined N-terminal domain instead of a CARD domain; however, they are grouped in the NLRC subfamily due to their structural similarity and homology relationship with other well-defined NLRCs (Proell, Riedl et al. 2008, Ting, Lovering et al. 2008).

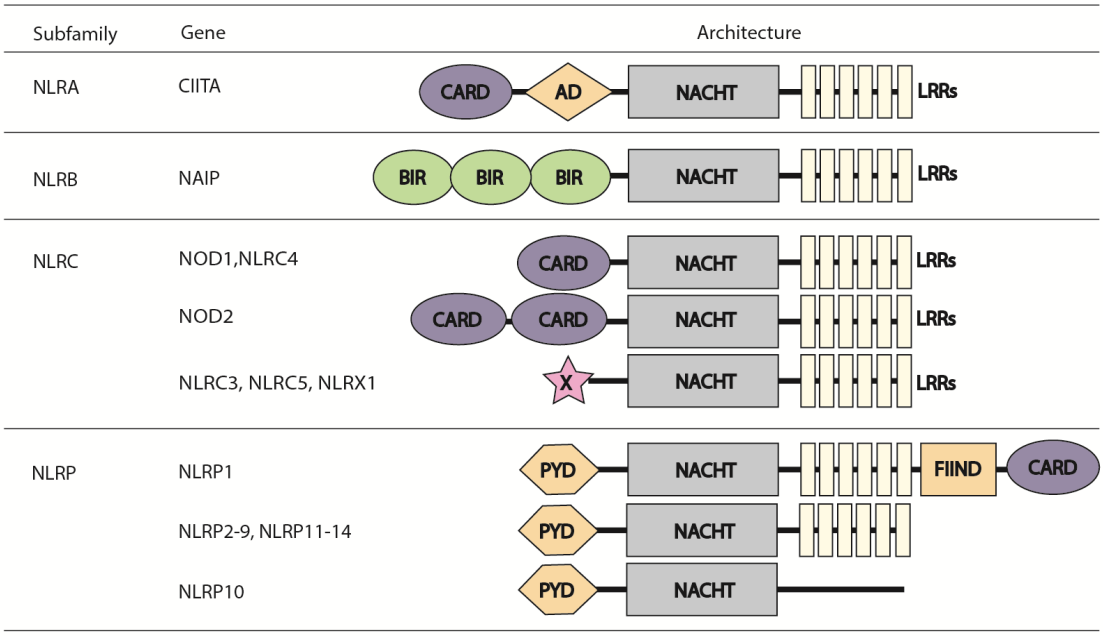

Figure 1.7. Nucleotide-binding oligomerization domain (NOD)-Like receptors (NLRs) structure. The general structure of NLRs consists of three domains, including functional domain, nucleotide-binding and oligomerization domain (NACHT), and Leucine-rich repeats domain (LRRs). NLRs have four subfamilies: NLRA, an acidic transactivation domain (AD); NLRB, a baculovirus inhibitor of apoptosis protein (IAP) repeat (BIR); NLRC, a caspase

recruitment and activation domain (CARD); and NLRP, a pyrin domain (PYD). In the NLRC subfamily, the X displays an unknown domain. For NLRP1, the FIIND displays the function-to-find domain.

NOD1 and NOD2 can recognize invading Gram-negative bacteria and Gram-positive bacteria by detecting their peptidoglycans (Motta, Soares et al. 2015). They are mainly distributed in the intestine - the first line of defence against harmful microbes - and they also play an important role in maintaining gut homeostasis (Motta, Soares et al. 2015). To maintain a balance between fighting against invasive pathogens and preventing overactive immune responses, NOD1 and NOD2 defend the host from microbial infection and prevent excess immune activity for symbiotic bacteria at the same time (Motta, Soares et al. 2015). NOD1 and NOD2 polymorphisms and mutations have been related to auto-immune disease, including Crohn's disease (CD) and other auto-immune diseases (Kim, Shin et al. 2016) (Figure 1.7). NLRC3 has been reported to inhibit the activation of T-cell regulators and TRAF6 (Schneider, Zimmermann et al. 2012). NLRC5 is related to the expression of MHC class I and regulates inflammatory responses (Benko, Magalhaes et al. 2010). Some studies show that NLRCX1 regulates the immune response against viral infection located on mitochondria, while mice with defective NLRCX1 do not exhibit the immune response against viruses mediated by NLRCX1 (Moore, Bergstralh et al. 2008) (Figure 1.6). NLRC4 is a classic member of the NLRC subfamily with an N-terminal CARD domain to mediate inflammasome formation and activation of immune responses (Zhao, Yang et al. 2011).

NLRP are proteins that are classified by their functional N-terminal domain PYD. Compared to NLRC receptors, the number and homologs of NLRP vary greatly between different species (Ting, Lovering et al. 2008). With scientific development, a multitude of NLRP receptor functions have been discovered (Figure 1.7). Despite their distributions in different types of cells, NLRP1, NLRP3, and NLRP6 all form inflammasomes to induce immune

responses. These inflammasomes act as signal platforms to recruit caspase 1 for the maturation and release of IL-18 and IL-1β. (Zhou, Yazdi et al. 2011, Levinsohn, Newman et al. 2012, Wang, Zhu et al. 2015). Different from other NLRPs, NLRP10 lacks an LRR domain, as shown in Figure 1.7. NLRP10 was reported to negatively mediate the formation of inflammasome complexes and help to initiate adaptive immune responses (Eisenbarth, Williams et al. 2012). NLRP2 has been reported to be required for early embryonic development of mice and act as an inhibitor to mediate NF-κB pathways (Fontalba, Gutierrez et al. 2007, Peng, Chang et al. 2012). NLRP12 can inhibit the noncanonical NF-κB pathway and AKT pathway to suppress colon inflammation and tumorigenesis (Allen, Wilson et al. 2012). NLRP4 negatively regulates the process of autophagy by binding with beclin1 (Jounai, Kobiyama et al. 2011). NLRP5 and NLRP7 are linked to mitochondrial function and lipopeptides recognition, respectively (Fernandes, Tsuda et al. 2012, Khare, Dorfleutner et al. 2012). NLRP11 participates in attenuating TLR-dependent signals by degrading TRAF6 with the help of ubiquitin ligase (Wu, Su et al. 2017). According to different studies, NLRP subfamilies have evolved with a strong selection constraint, which limits their functional diversity (Vasseur, Boniotto et al. 2012). NLRP receptors may be crucial for cellular homeostasis. There is only one NRLP, called MHC-II transactivator (CIITA), that belongs to the NLRA subfamily (Figure 1.7). As its name suggests, CIITA is a regulator for MHC-II expression. The last NLRP subfamily member is NLRB, which features the amino-terminal BIR domain. The only subfamily member that has been identified to date in humans is NAIP, while in mice there are six members, named as NAIP1-6. In humans, NAIP receptors are known to bind with NLRC4 to form inflammasome complexes that respond to microbial ligands from type III secretion system (T3SS) (Vance 2015). NAIP receptors in mice can detect more stimuli, including flagellin and T3SS (Vance 2015).

When NLR protein LRRs detect and encounter pathogenic ligands, NLRs undergo

conformational rearrangements from an auto-inhibited state (monomer) to an active state (oligomer) (Kim, Shin et al. 2016). During this process, LRRs disassociate from the NOD domain to activate NLRs (Kim, Shin et al. 2016). The binding site of NLRs is exposed to recruit CARD/PYD containing proteins for activation and oligomerization to form inflammatory complexes for propagating signals to downstream pathways (Kim, Shin et al. 2016). Subsequently, the stimulated NLRs activate downstream signaling pathways to release proinflammatory cytokines and chemokines for host defense against invading pathogens (Kim, Shin et al. 2016). To date, three major activation targets for NLR mediation of signaling pathways have been identified, including MAPKs, NF-κB, and caspase-1 in immune activities (Kim, Shin et al. 2016).

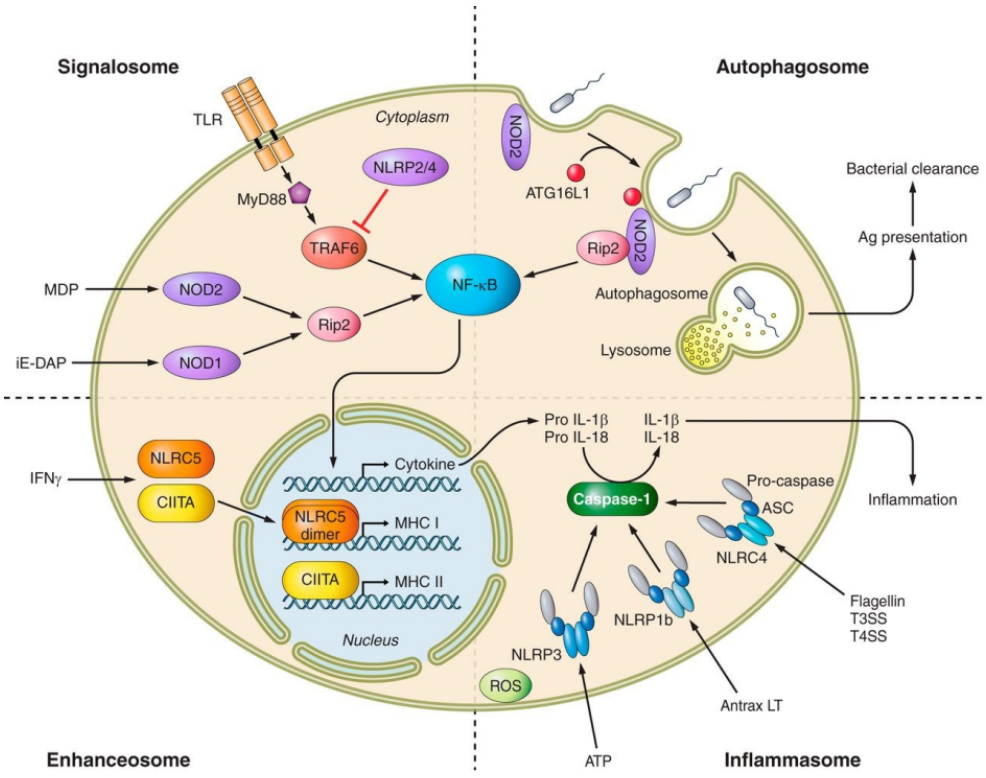

Figure 1.8 The overview of NLR mediated signaling pathways, adapted from (Motta, Soares et al. 2015). NLRs are classified into four functional categories: signaling transduction, autophagy, transcriptional actiation, and inflammame. NOD1 and NOD2 are known to activate NF-κB. Some other NLRs are known to regualte this signal, such as NLRP2 and NLRP4. NOD2 is also known to recruit ATL16L1 for autophagy. Various NLRs can be triggered to form inflammasome. CIITA and NLRC5 are reported to be transactivators for MHC I and MHC II.

In NLRs, NOD1 was the first identified and most studied NLR. By homology searching, NOD2 was the second recognized and well-characterized NLR (Ogura, Inohara et al. 2001). Upon detection of specific agonists, NOD1 and NOD2 initiate their conformational changes, followed by self-oligomerization to recruit and activate their shared adaptor, receptor-interacting serine/threonine-protein kinase 2 (RIP2 or RICK). RIP2 activation further triggers both NF-κB and MAPKs pathways to produce cytokines (Ogura, Inohara et al. 2001, Caruso, Warner et al. 2014) (Figure 1.8). Another important pathway modulated by NLRs is mediated by ASC adaptor protein. Activated ASC forms specks and recruits pro-caspase-1 for production of mature caspase-1, which mediates the cleavage and maturation of IL-1β and IL-18 from pro- IL-1β and pro-IL-18 (Srinivasula, Poyet et al. 2002, He, Mekasha et al. 2010). NLRP1, NLRP3, and NLRC4 are typical examples of inflammasome formation that depend on ASC through PYD-PYD interactions (He, Mekasha et al. 2010, Zhao, Yang et al. 2011). CARD-CARD or PYD-PYD protein-protein interaction is a hallmark for ASC dependent pathway to form large macromolecular complexes and serve as a signalling platform to induce oligomerization and recruitment of effector proteins to activate caspase-1, termed as the inflammasome (Mariathasan, Newton et al. 2004, Zhou, Yazdi et al. 2011, Rathinam, Vanaja et al. 2012). In this way, adaptor protein ASC bridges transmit signals from NLRs to caspase-1 (Rathinam, Vanaja et al. 2012). NLRB subfamily members without

CARD or PYD have been demonstrated to bind with NLRC4 to recruit caspase-1 for immune defence (Vance 2015).

The Implication of PRRs in Immune Diseases

Being crucial members in innate immunity, PRRs recognize foreign pathogens to protect the host by inducing acute inflammation, and meanwhile suppress overactive immune responses that might lead to autoimmune diseases, such as Crohn's disease (CD), encephalitis, arthritis, or systemic lupus erythematosus (SLE) (Wu, Tang et al. 2015, Cao 2016).

Systemic lupus erythematosus is a systemic chronic autoimmune disease and is characterized by the loss of tolerance for self-nuclear antigens (Herrmann, Voll et al. 1998). SLE is diagnosed by the accumulation of serological anti-nuclear antibodies (ANA) against nucleic acids released from dead cells (Kruse, Janko et al. 2010). About 40% of SLE patients exhibit defects in the clearance of dead cells (Kruse, Janko et al. 2010). The inefficient clearance of damaged cells leads to increased release of DNA and RNA, which can be detected by TLRs, and induces the production of type-I interferons and autoantibodies (Wu, Tang et al. 2015). It is well known that TLR7, TLR8, and TLR9 recognize nucleic acids to trigger immune responses. TLR7/8/9 polymorphisms contribute to SLE susceptibility (Celhar, Magalhaes et al. 2012, Dos Santos, Valverde et al. 2012). There are various agents under development for the treatment of SLE that target TLRs at different stages in immune signaling pathways (Wu, Tang et al. 2015). For example, small molecular inhibitors, including hydroxychloroquine sulfate (HCQ), are designed to target TLR7/8/9 to suppress their activation (Wu, Tang et al. 2015). It is also reported that cGAS-STING pathway is associated with SLE by upregulation type-I interferon production (Ding, Dong et al. 2015). Besides SLE, TLRs have been reported as central to be other chronic autoimmune diseases, including rheumatoid arthritis (RA), multiple sclerosis (MS), and experimental autoimmune encephalomyelitis (EAE) (Fairhurst,

Wandstrat et al. 2006, Goh and Midwood 2011). TLRs are important for innate immunity and also direct the induction of adaptive immunity. What results is the exploitation of TLR agonists as adjuvants for autoimmune diseases, cancer vaccines, and immunotherapies for tumours (Dunne, Marshall et al. 2011). TLR ligands and TLR agonists have been assessed as adjuvants in cancer vaccines (Dunne, Marshall et al. 2011).

Inflammatory diseases are defined as clinical inflammatory disorders with symptoms of inflammation mediated by cells and molecules of innate immunity. Gain-of-function mutations in PRRs are correlated with autoinflammatory diseases (Cao 2016). For example, there are three autoinflammatory diseases which are related to the gain-of-function NLRP3 variants, including familial-cold-autoinflammatory syndrome (FCAS), Muckle-Wells syndrome (MWS), and neonatal-onset-multisystem-inflammatory disease (NOMID) (Hoffman, Mueller et al. 2001, Aksentijevich, Nowak et al. 2002, Feldmann, Prieur et al. 2002). The common symptoms of these inflammatory diseases are urticarial and recurrent fever caused by excessive production of IL-1β and other inflammatory cytokines. Compared to gain-of-function PRR variants, loss-of-function mutations make the host more susceptible to foreign pathogens. Loss-of-function mutations are also associated with immune diseases. It is well known that the polymorphisms of NOD2 are the most potent genetic factors for the development of CD. Three NOD2 variants, including L1007insC, G908R, and R702W, are reported to make a significant contribution to the development of CD (Eley, Sugden et al. 2004, Maharana, Dehury et al. 2015). The risk of CD increases slightly for the patients with only one NOD2 variant, while a 20-40 fold risk is observed in individuals with a combination of NOD2 variants (Vasseur, Sendid et al. 2011). The environment plays an essential role in immune regulation. The link between NOD2 variants and CD suggests that NOD2 variants impair the ability to detect and clear invading bacteria, which leads to the aberrant inflammation in the NOD2-independent pathways (Inohara, Ogura et al. 2003). In addition to

NLRs, it is also important for the host to be able to remove pathogens by TLR-mediated microbial recognition. Similar to NLRs, excess immune responses induced by TLRs would result in inflammatory diseases, including lethal septic shock syndrome (Takeuchi and Akira 2010, Hagar, Powell et al. 2013).

In a healthy host, upon microbial infection, multiple PRRs are activated simultaneously to protect the host. Thus, the presence of loss-of-function and gain-of-function variants of PRRs may lead to the development of various immune diseases (Palm and Medzhitov 2009, Takeuchi and Akira 2010). As a result, to gain a better understanding of these immune diseases, it is necessary for the functions and molecular structures of PRRs to be studied carefully.

1.2. Comparison of Different Death Domain-Containing Proteins

The death domain (DD) superfamily is the most prominent domain family. It is classified into four subfamilies – death effector domain (DED), CARD, death domain (DD), and PYD containing subfamilies – according to their interaction properties and sequence similarity (Park, Lo et al. 2007) (Figure1.9). DD superfamily proteins are primarily conserved in mammals, drosophila, *C. elegans*, and other multicellular organisms during evolution (Park, Lo et al. 2007). According to human genome analysis, there are potentially 32 death domain-, 7 DED-, 28 CARD-, and 19 PYD-containing proteins (Park, Lo et al. 2007). Interestingly, interactions have only been observed among proteins within the same subfamilies, with no cross interactions between proteins from different subfamilies (Kwon, Yoon et al. 2011).

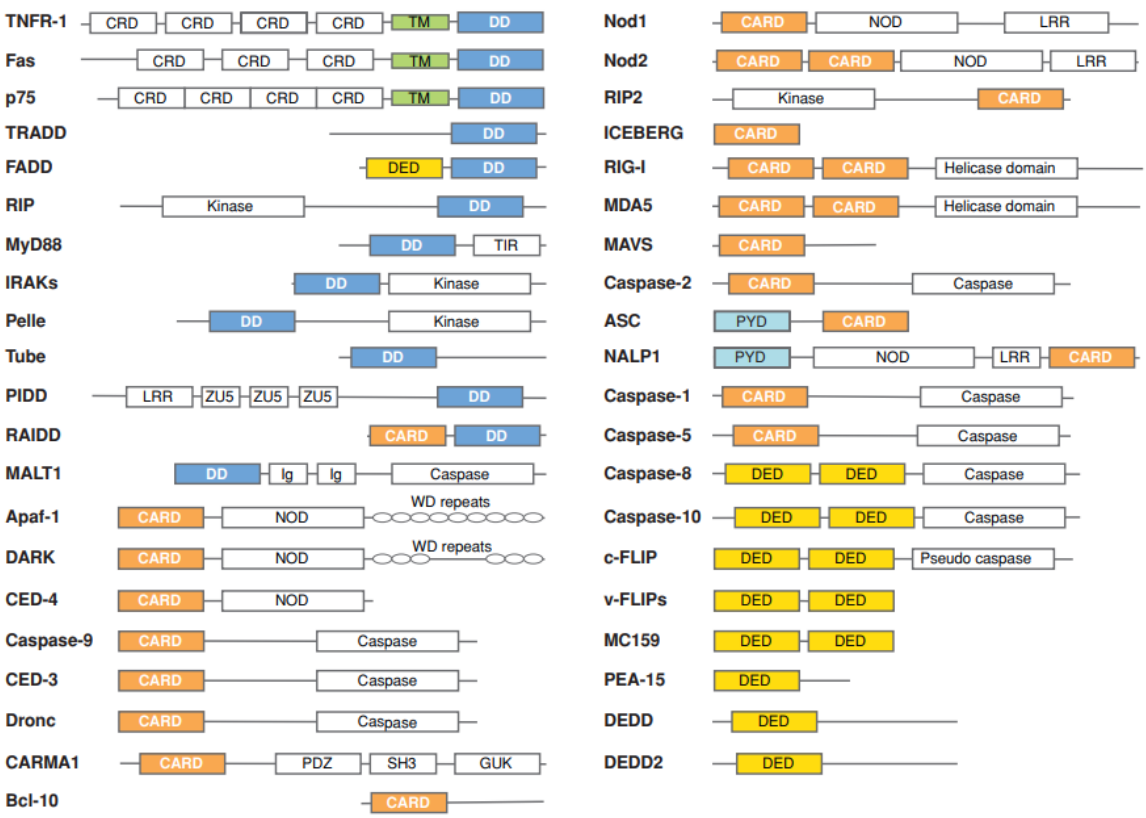

Figure 1.9. Selective list of death domain superfamily, adapted from (Park, Lo et al. 2007). CARD, caspase-activation and recruitment domain; DD, death domain; DED, death effector domain; GUK, guanylate kinase-like; LRR, leucine-rich repeat; NOD, nucleotide-binding and oligomerization domain; PYD, pyrin domain; TIR, Toll/interleukin-1 receptor; CRD, cysteine-rich domain; TM, transmembrane domain.

A typical feature of DD family members is that they consist of six antiparallel α-helices (Ferrao and Wu 2012) (Figure 1.10a). In the DD domain superfamily, low sequence similarity, short length, and orientation of helices yield a flexible surface for their interactions within yet restricted to the subfamily (Ferrao and Wu 2012).

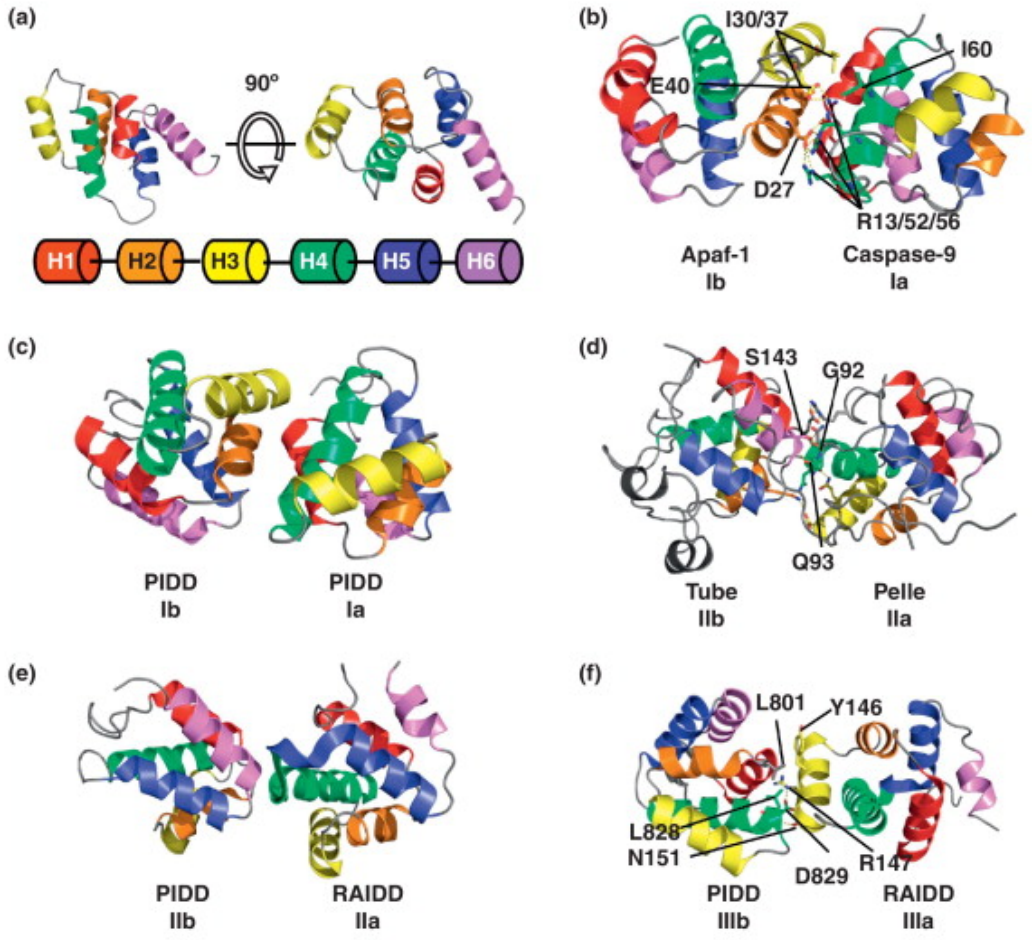

Figure 1.10. Three different types of representative interactions formed by DD domain , adapted from (Ferrao and Wu 2012). (a) The NMR structure of Fas DD containing six α-helices architecture. (b) Heterodimeric structure from caspase-9 and Apaf-1 interactive domains. (c) DD domains of PIDD including type-I interaction. (d) Type II interface was observed among the dimeric structure of Pelle and Tube. (e) RAIDD and PIDD interaction was supported by type II interaction. (f) Heterodimer of PIDD and RAIDD DD domains, demonstrating type III interfaces.

These death domain containing proteins interact with each other to form macro complexes via three interface types within the subfamily, identified according to their interaction mode as types I, II, and III (Ferrao and Wu 2012). Type I (Ia/Ib) is a heterodimer formed by the

CARD domains of Apaf-1 and caspase-9, commonly known as the first structure of a death domain (Qin, Srinivasula et al. 1999).

This dimer is an asymmetrical structure and representative of type I interaction (Qin, Srinivasula et al. 1999) (Figure 1.10b). Type Ia interface of caspase-9 – formed by positively charged helices 1 and 4 – interacts with type Ib surface Apaf-1 – formed by negatively charged helices 2 and 3 (Weber and Vincenz 2001). The stability of Apaf-1 and Caspase-9 heterodimer is mainly due to two residues (E40 and D27) from Apaf-1 CARD and three residues (R56, R52 and R13) from Caspase-9 CARD (Ferrao and Wu 2012). In short, the crystal structure of PIDD homodimer was confirmed to be supported by the type I interaction (Figure 1.10c).

Type II interaction (IIa/IIb) was first found in the homodimer of Tube and Pelle DDs, and was different from the interaction observed in the crystal structure of Apaf-1/caspase-9 heterodimer (Ferrao and Wu 2012). The type IIa interface is located at Pelle DD, formed by the loop of H4-H5 and the last several residues of H4 (Xiao, Towb et al. 1999). IIb interface of Tube consists of a groove contributed by H6 on one side and the H1-H2 corner on one side (Xiao, Towb et al. 1999) (Figure 1.10d). With the PIDDosome structure solved, type IIa/IIb interaction was further confirmed in the structure (Park, Logette et al. 2007)(Figure 1.10e).

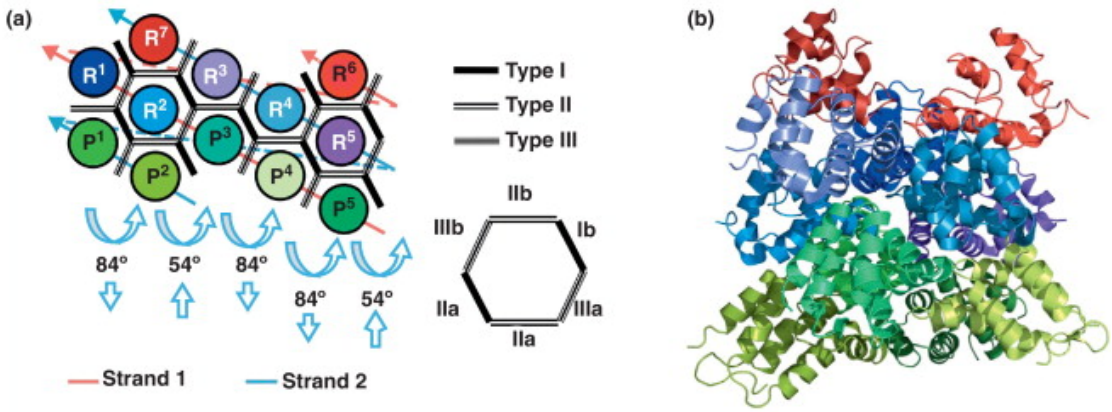

Figure 1.11. Structure of PIDDosome consisting of PIDD and RAIDD DDs, adapted from (Ferrao and Wu 2012). (a) Planar schematic of PIDDosomes by three different interfaces. (b) PIDDosome structure solved by crystallization and colored as in (a).

The last pair interaction of IIIa/IIIb was first observed in the structure of PIDDosome, which demonstrates how these binary interactions form an oligomeric DD complex (Figure 1.11a). It was reported that 7 RAIDD DDs and 5 PIDD DDs assembled and organized into a ternary structure (Figure 1.11b). The lower layer was formed by 5 death domains of PIDD, with a second layer consisting of 5 death domains of RAIDD, and 2 death domains from RAIDD to form a top layer. The type IIIa/IIIb pair is supported by the interactions between the H1-H2 formed grove and loops located at H3-H4 helices (Park, Logette et al. 2007). The IIIa/IIIb interface contains polar interactions, charged residues, and hydrophobic interactions. In the PIDDosome structure, type I and type III interactions exist between the dimeric structures of RAIDD: RAIDD, PIDD: PIDD, and RAIDD: PIDD, while type II interactions are observed only between RAIDD: PIDD and RAIDD: RAIDD (Ferrao and Wu 2012).

Like in PIDDosome oligomeric complexes, the strong interactions of type I/II/III from death domain-containing proteins are highly conserved in all oligomeric signaling complexes, acting as the mechanism for how DDs polymerize to macromolecules (Ferrao and Wu 2012). Although the overall structure of DDs is conserved, there are many variations in residues that contribute to each interaction interface (Ferrao and Wu 2012). Below are some examples of how DDs mediate interactions for helical oligomers.

RIG-I and MAVS interaction by homotypic CARD-CARD

MDA5 and RIG-I are a typical type of PRRs that are able to recognize viral RNAs at the early stage of infection. Their activation initiates immune responses by triggering downstream signaling pathways for the production of cytokines and interferons (Yoneyama,

Kikuchi et al. 2005). In the presence of viral RNAs, the interaction between the helicase domain of RIG-I (or MDA5) and its CARD domain competes with viral RNA at the same binding site (Yoneyama, Kikuchi et al. 2005). Activated RIG-I releases its tandem CARD domains to form a tetramer, which brings MAVS CARD into proximity and serves as a template for MAVS to form a filamentous structure (Wu and Hur 2015). Looking into the structural detail of the MAVS CARD filament, it exhibits a helical symmetry of an axial rise of 5.13 Å and a rotation angle of 101.1º (Wu, Peisley et al. 2014).

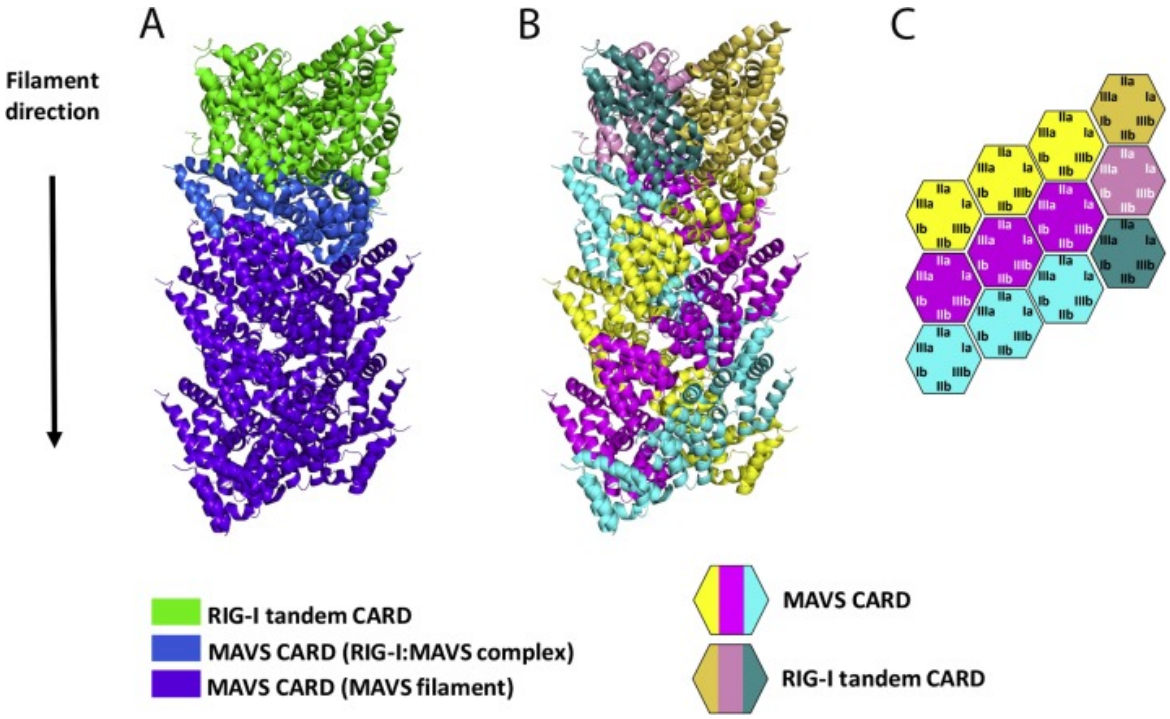

Figure 1.12. Helical assemblies of RIG-I and MAVS DDs, adapted from (Wu, Peisley et al. 2014). (A) Tetrameric RIG-I 2CARD forms a template for MAVS CARD polymerization. The death domains from RIG-I 2CARD: MAVS CARD crystal structure is coloured green and blue. (B) The single-stranded helix structure of DDs of RIG-I and MAVS. The three strands are illustrated by different colours: yellow, magenta, and cyan. (C) Planar illustration of DDs helical assemblies.

Each MAVS CARD in the filamentous assembly has the identical conformation as the

monomeric MAVS CARD (Wu, Peisley et al. 2014). Like the RIG-I 2CARD tetrameric structure, each MAVS CARD in the filament interacts with six neighboring subunits by its six different surfaces (Ia, Ib, IIa, IIb, IIIa, and IIIb). Three types of interactions are observed including interstrand interaction by Ia:Ib and IIa:IIb interfaces as well as intrastrand interactions by IIIa:IIIb surface areas, which are similar to the interactions in the RIG-I 2CARD tetrameric structure (Figure 1.12C). The structures of MAVS CARD filament and RIG-I 2CARD tetramer are superposed together to analyze their helical assemblies. The result showed that the two structures are highly aligned and share the same helical geometry (Wu, Peisley et al. 2014).

The CARD domains of MAVS and RIG-I were fused and crystallized to form a single-stranded left-handed helical tetramer, which gives us more insights about the mechanisms of transient interaction in signal transduction (Wu, Peisley et al. 2014) (Figure 1.12A). It showed that MAVS CARD- and RIG-I CARD-fused proteins form a helical oligomer by IIa/IIb interactions. In the oligomeric structure, RIG-I CARD forms the basic helical tetramer, acting as a template for the assembly of MAVS CARD by stacking on top of RIG-I CARD. This symmetry aligns with the parameters of K65-Ubn linked RIG-I CARD structure (Wu, Peisley et al. 2014). In a comparison of interactions between MAVS CARD oligomer and MAVS CARD: RIG-I 2CARD-fused tetramer, the residues located in the interfaces of Ia, IIa, and IIIa of MAVS CARD are the same to interact with Ib, IIb, and IIIb interfaces of MAVS CARD and the second CARD of RIG-I. Sequencing alignment demonstrated that the residues are different and flexible in the surfaces of Ib, IIb, and IIIb between MAVS CARD and the second CARD of RIG-I, implying that the surface of MAVS CARD is plastic and capable of interacting with different surface residues (Wu, Peisley et al. 2014).

MyD88 and IRAK2/4 Complex by Death Domain Interaction

In the TLR signaling pathway, Toll/IL-1R (TIR) domains of TLR receptors recruit downstream TIR-containing proteins, such as Myd88, once TLR proteins bind with PAMPs to initiate immune responses (Yamamoto, Sato et al. 2003). The dysfunction of this signaling pathway is related to many human diseases, including allergy and autoimmune diseases (Yamamoto, Sato et al. 2003). Recognizing DAMPs and PAMPs is the start of the TLR pathway to recruit Myd88, TIRAP, and TRIF-containing TIR domains (Yamamoto, Sato et al. 2003). Myd88 contains an intermediate domain (ID) and an amino-terminal death domain (Yamamoto, Sato et al. 2003). MyD88 interacts with IRAKs, which include IAK1, IRAK2, and IRAK4. The architecture of IRAKs consists of two typical domains: an N-terminal death domain and a Ser/Thr kinase or kinase-like domain (Lin, Lo et al. 2010).

Recently, the crystal structure of Myd88-IRAK4-IRAK2 DD complex was reported at a resolution of 3.4 Å (Lin, Lo et al. 2010). The group demonstrates that the ternary and four-layer Myddosome complex formed by a total of 14 death domains is a three-layer structure with 70 Å in diameter, 110Å in height, a rotation angle of 98±2 º, and a helical axis of about 6 Å (Lin, Lo et al. 2010). The bottom contains two layers formed by 6 death domains of Myd88, followed with 4 death domains of IRAK4 in the middle layer and 4 death domains IRAK2 at the top layer (Figure 1.13b). Myd88 and IRAK DDs first form a binary Myddosome complex, which further recruits IRAK2 to form a ternary Myddosome complex. The MyD88-IRAK4-IRAK2 complex is a single helical structure with left-handedness (Lin, Lo et al. 2010).

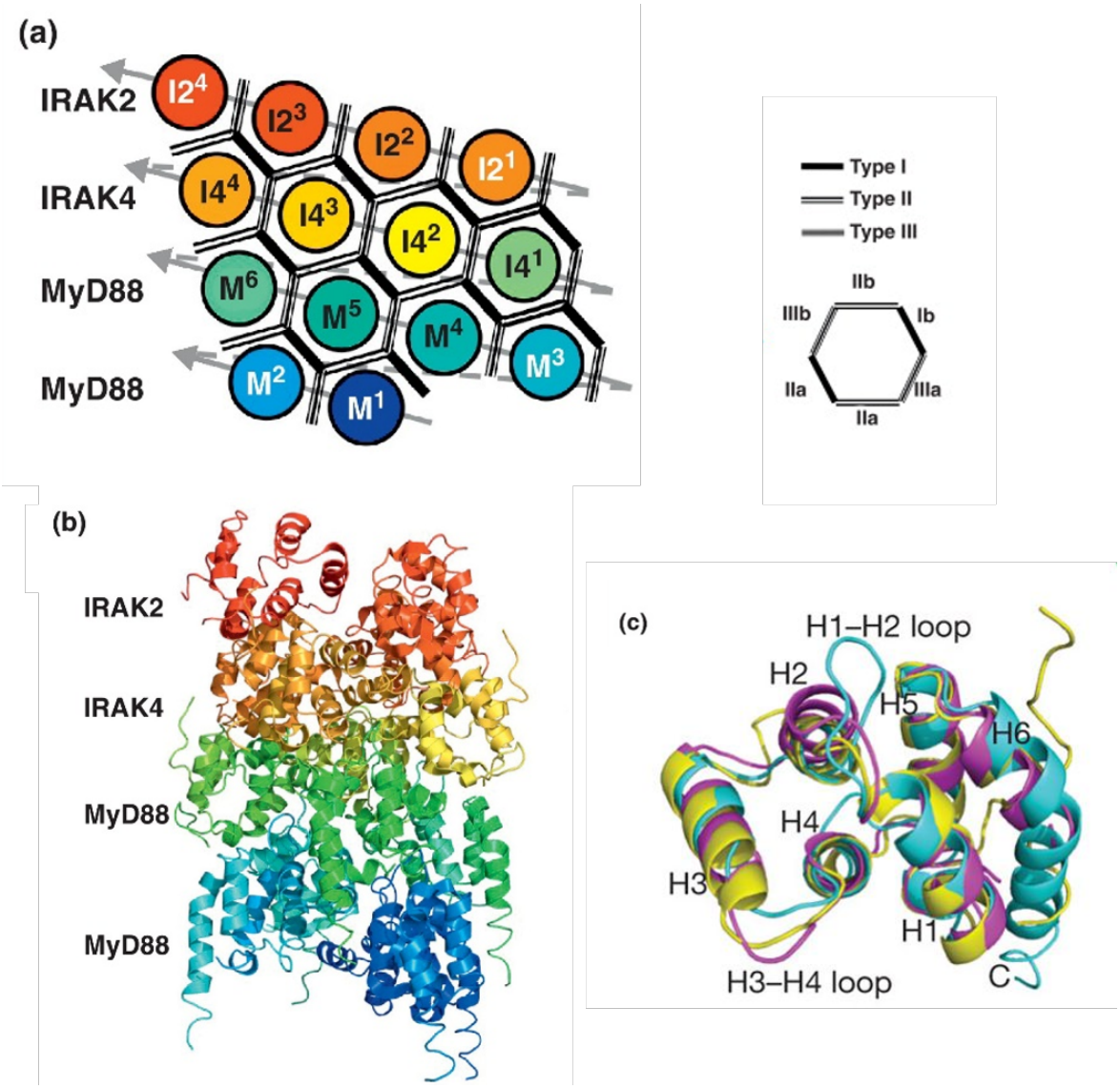

Figure 1.13. Diagram of Myddosome structure, formed by DDs from Myd88, IRAK2, and IRAK4, adopted from (Ferrao and Wu 2012). (a)Planar schematic of the Myddosome ternary complex. The Myddosome is an oligomeric complex consisting of four DDs of IRAK2, four DDs of IRAK4, and four DDs of Myd88 DD. (b) The crystal structure of Myddosome, coloured as in (a). (c) Superposition DDs of Myd88 (cyan), IRAK4 (yellow), and IRAK2 (magenta).

All Myd88, IRAK4, and IRAK2 death domains are formed by 6 α-helices, H1 to H6, with different structural features. Compared to death domains of IRAK4 and IRAK2, the third helix of Myd88 is short, and the sixth helix is extraordinarily long with 19 residues (Lin, Lo

et al. 2010). Comparring their loop regions, the longest H1-H2 loop belongs to Myd88, the longest H2-H3 loop belongs to IRAK4, the shortest H3-H4 loop belongs to Myd88, and the longest HE-H5 loop belongs to Myd88 (Lin, Lo et al. 2010). Similar to other CARD domains, Myddosome complex is supported by three different interaction types: Ia/Ib, IIa/IIb and IIIa/IIa. Based on the structure of Myddosome, the interactions between different layers are mediated by Ia/Ib and IIa/IIb interactions, and the IIIa/IIIb interaction exists in adjacent death domains of the helical spiral symmetry. The monomeric structures of IRAK2, IRAK4, and Myd88 have incredibly high similarity after superpositioning monomers (Lin, Lo et al. 2010) (Figure 1.13c). For a more in-depth analysis of the interaction of Myddosome, three different types of interface interactions are examined in detail. Ia and Ib interfaces consist of the second and third helixes on one death domain and the first and fourth helixes on another death domain (Lin, Lo et al. 2010). The IIa/IIb interface interaction is formed by two opposing edges of death domains at the centre of the H4 to H5 area loop and the H1–H2 area loop (Lin, Lo et al. 2010). The third helix and the area located at H3-H4 loops make a significant contribution to the formation of type III interaction (Lin, Lo et al. 2010). Due to their more rigid and tight structures, Ia:Ib and IIa:IIb interfaces interact more prevalently than IIIa:IIIb interfaces (Lin, Lo et al. 2010). According to the structural analysis of Myddosome on shape complementarity and interface charge, both the top and the bottom surfaces of Myd88 layers have much lower scores compared to IRAK death domains (Yamamoto, Sato et al. 2003, Deguine and Barton 2014). In the Myddosome, death domain of IRAK4 recruits IRAK2 due to their good shape and charge complementarities. The reason why there is only one layer of IRAK2 assembled into Myddosome is that the top surface of IRAK2 is incompatible with its bottom surface (Ferrao and Wu 2012).

1.3. NOD1/2 and RIP2 Induced Signaling Pathway

NOD1 is the first member of NOD-like receptors. By homology searching, NOD2 is

characterized based on its high similarity in architecture and function with NOD1 (Ogura, Inohara et al. 2001). NOD1 and NOD2 share the same structural architecture that consists of an N-terminal CARD, an intermediate NOD, and an array of C-terminal LRRs (Ogura, Inohara et al. 2001). It was previously shown that NOD1 and NOD2 participate in the activation of transcriptional factors for the NF-κB family, involving the removal of peptidoglycan fragments (Motta, Soares et al. 2015). NOD1 and NOD2 are widely expressed in the intestine to maintain gut homeostasis by fighting against bacterial infections (Kim, Shin et al. 2016). It was demonstrated that NOD1 senses bacterial ligand iE-DAP, found in the surface of all $Gram^-$ bacteria and some $Gram^+$ bacteria (Motta, Soares et al. 2015) (Figure 1.14). MDP is the best-known ligand to stimulate NOD2 activation, and is widely distributed among $Gram^-$ and $Gram^+$ bacteria (Motta, Soares et al. 2015) (Figure 1.14). In the presence of a respective stimulus, NOD1 and NOD2 oligomerize through NOD domains and recruit their common adaptor protein RIP2, a crucial protein for immediate downstream signalling pathway (Caruso, Warner et al. 2014), by homotypic CARD-CARD interaction.

The mechanism for how peptidoglycan (PGN) fragments enter cells and activate NOD1/2 is still not clear, but several entry routes have been suggested (Caruso, Warner et al. 2014). One study reported that phagosomes perform phagocytosis by internalizing bacteria and detecting the presence of muramyl dipeptide (MDP) in their endosome membranes (Nakamura, Lill et al. 2014). Other transport methods are demonstrated by other research, such as pore bacterial secretion systems or membrane vesicles (Caruso, Warner et al. 2014, Thay, Damm et al. 2014).

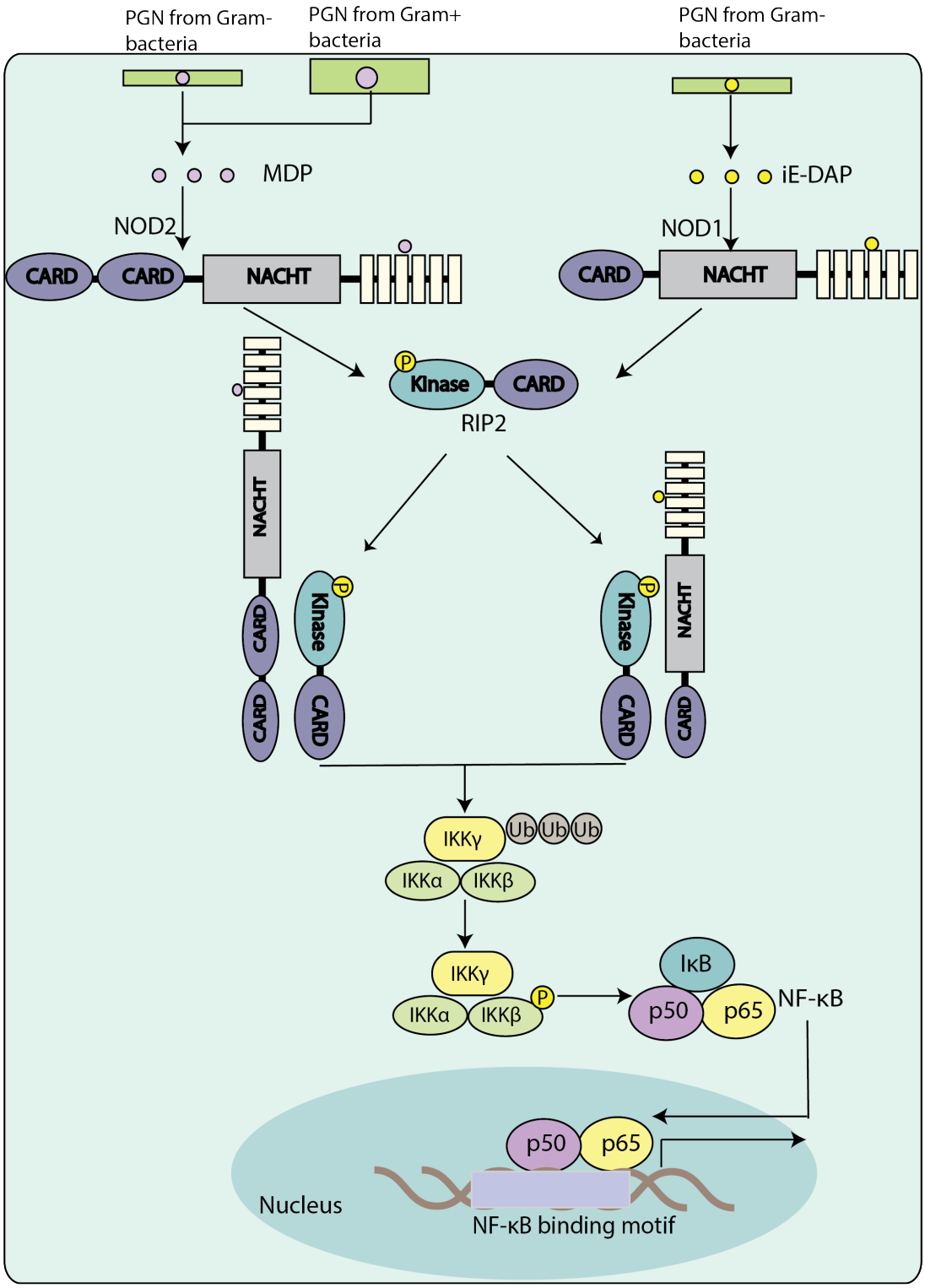

Figure 1.14. Recognition of muramyl dipeptide (MDP) and γ-D-glutamyl-meso-diaminopimelic acid (iE-DAP) by leucine-rich repeat (LRR) domains activate NOD2 and NOD1, respectively. Stimulated NOD1 and NOD2 recruit receptor-interacting serine/threonine kinase 2 (RIP2) by CARD-CARD interactions. Activated RIP2 leads to K63-

linked ubiquitination of IKKγ, which further recruits and phosphates IKKα and IKKβ to form IKK complex. This complex phosphorylates IκB and further releases nuclear factor-κB (NF-κB) for translocation to the nucleus to regulate expression of inflammatory genes.

To confirm whether NOD1/2 respond directly to PGN fragments or indirectly by some intermediate molecules, much work has been done. With the appearance of experimental evidence via Surface Plasmon Resonance (SPR), the direct interaction between MDP and NOD2, Tri-DAP, and NOD1 has been recognised (Laroui, Yan et al. 2011) (Figure 1.14). It is necessary to consider the architecture and structure of NOD1/2 to have a better understanding of the mechanism of NOD1/2 activation. The intermediate NOD domain of NOD1 and NOD2 consists of two helix domains (HD1 and HD2), a nucleotide-binding domain (NBD), and a winged-helix (WH). Like mouse NLRC4ΔCARD, rabbit NOD2Δcard (residues 1-194, 245-251 deleted) was purified and crystallized, and exhibited a similar sensitivity as wild-type NOD2 in the presence of MDP (Maekawa, Ohto et al. 2016). The inactivated state of NOD1/2 is inhibited and maintained by the specific interaction between NBD and WH, which is occluded by LRRs for further stabilizing the monomeric form of NOD1/2 (Figure 1.15). For the closed and inactive form of NOD2, Adenosine diphosphate (ADP) binding makes a contribution to stabilizing the NACHT domain (Maekawa, Ohto et al. 2016). Once LRRs detect the invading pathogens, HD2 initiates the conformational change in NOD domain, allowing the exchange of ADP to ATP. With ATP hydrolysis, NOD1 and NOD2 self-oligomerize to expose activation sites for following immune signals (Maekawa, Ohto et al. 2016).

In the presence of their respective stimulus, active NOD1 and NOD2 oligomerize and recruit RIP2 and RICK – key proteins for immediate downstream signaling pathways –=by homotypic CARD-CARD interaction (Figure 1.14). Active RIP2 recruits and activates

serine/threonine kinase TAK1 via proximity to IκB kinase (IKK) complexes (Caruso, Warner et al. 2014). TAK1 recruitment is required for the activation of IKK complex, which determines the phosphorylation of IκBα. The co-localization of IKK complexes and TAK1 initiates the phosphorylation of IκKβ and degradation of IκBα through the proteasome, which allows the nuclear translocation of NF-κB and influences the expression of downstream target genes (Caruso, Warner et al. 2014)(Figure 1.14).

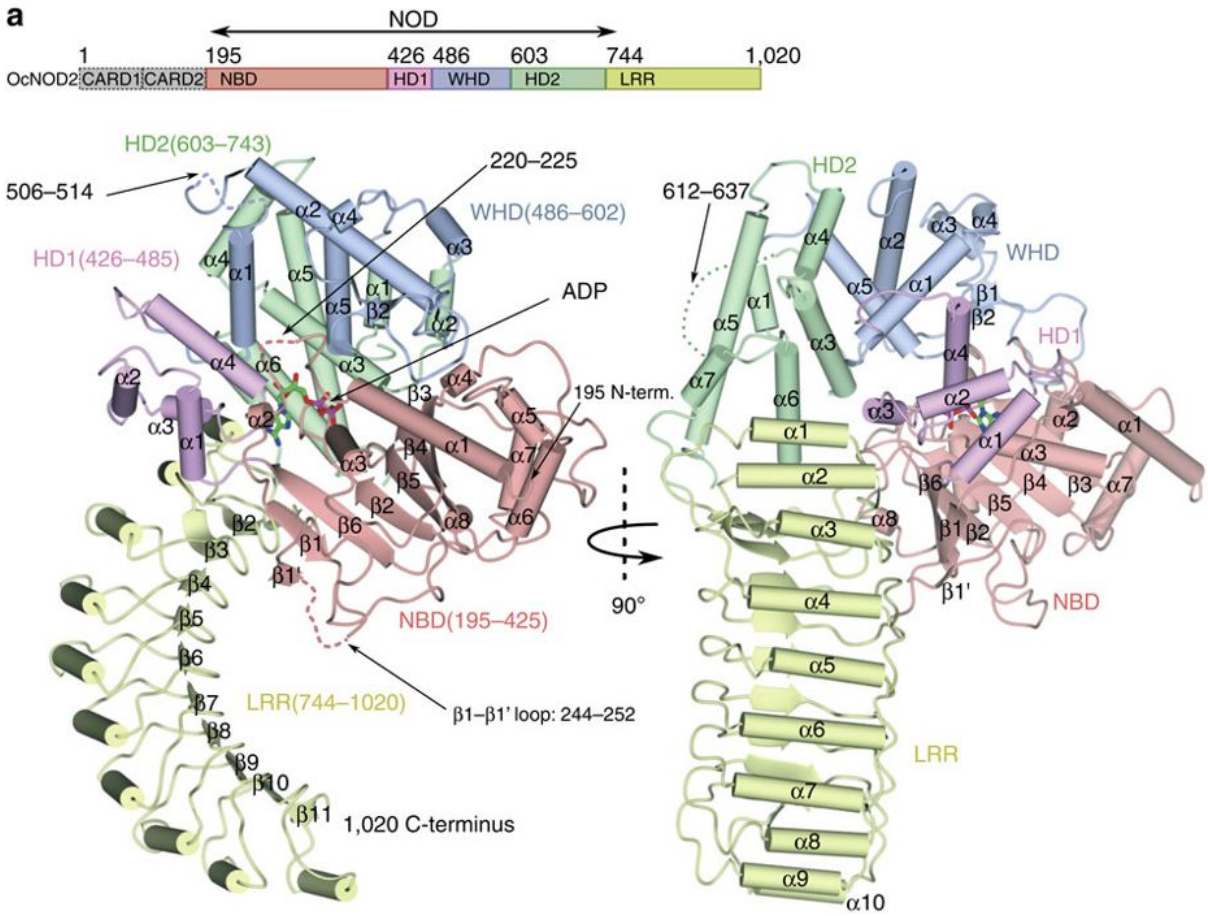

Figure 1.15. Structure of OcNOD2ΔCARDΔloop, adapted from (Maekawa, Ohto et al. 2016). The architecture of OcNOD2 and the crystal structure of ADP-bound OcNOD2 without CARD domain.

NF-κB activates transcriptional factors of cytokines and chemokines to release TNF-α, IL-1β, and IL-18 from immune cells to defend the host from attacking pathogens (Caruso, Warner et al. 2014). A recent study shows that NOD1/NOD2 sensing PGN fragments is the initial step

of autophagy, which does not require the activity of RIP2 protein or activation of the NF-κB pathway (Travassos, Carneiro et al. 2010). Additionally, ATG16L1-induced autophagy for invading pathogens is reportedly located at the plasma membrane and activated by NOD1 and NOD2 (Travassos, Carneiro et al. 2010). Some studies have exhibited NOD1 and NOD2 as important mediators to induce inflammation when mouse or human cells are in an ER-stress state (Keestra-Gounder, Byndloss et al. 2016). The mechanism is that IL-6 can be made NOD1/2-dependent when host cells detect the presence of ER-stress inducers dithiothreitol or thapsigargin, which potentially explains how ER-stress induced inflammation is associated with the innate immune system (Keestra-Gounder, Byndloss et al. 2016).

In innate immunity, harmful microbes are detected by several PRRs for different or the same ligands. *In vivo*, the influences on pathogen removal are limited for defective NOD1 and NOD2 (Caruso, Warner et al. 2014). For example, it is redundant for TLRs and NOD1/2 to detect invading bacteria for immune responses by the production of cytokines, given that they both lead to the activation of MAPK and NF-κB pathways (Akira and Takeda 2004). It was demonstrated that the roles of NOD1 and NOD2 are important for innate immunity when TLR-induced signals are decreased or absent (Kim, Park et al. 2008, Caruso, Warner et al. 2014). In the modified epithelial cells, although they are insensitive to ligands recognized by TLR, NOD1 and NOD2 ligands are still detected and activate the immune response in order to protect cells (Kim, Lee et al. 2004). NOD1 and NOD2 have a different distribution in human cells. NOD2 is only distributed in some cells, such as hematopoietic cells, whereas NOD1 is found to be expressed in endothelial, epithelial, and other immune cells (Ogura, Lala et al. 2003, Park, Kim et al. 2007). In epithelial cells, NOD1 stimulates ligands, inducing the production of immune cytokines and release of signals to recruit acute inflammatory cells for inflammation (Masumoto, Yang et al. 2006). In line with previous experiments, when epithelial cells are infected with bacteria such as *Helicobacter pylori*, NOD1 makes a

contribution to the activation of immune defence (Allison, Kufer et al. 2009, Kim, Jeong et al. 2010). In the intestinal tract, NOD2 is distributed in Paneth cells to detect different types of peptidoglycans (Hasegawa, Yang et al. 2006), aligned with the result that NOD2 encourages the host to clear *Citrobacter rodentium* by activation of immune responses in the intestine and *Staphylococcus aureus* in the skin (Hruz, Zinkernagel et al. 2009, Kim, Kamada et al. 2011). To evade detection by NOD1/2 and clearance by the host, pathogens have evolved mechanisms to modify PGN via *N*-deacetylation (Boneca, Dussurget et al. 2007). Besides their function in the innate immune system, NOD1 and NOD2 influence adaptive immune responses by promoting the priming of immune cells, including T helper cells-type 1 (Th1) and T helper cells-type 17 (TH17) (Fritz, Le Bourhis et al. 2007, Magalhaes, Fritz et al. 2008).

NOD1 and NOD2 are associated with many immune diseases. It is reported that NOD2 polymorphisms are the most potent genetic factor for the development of Crohn's disease (Caruso, Warner et al. 2014). The mechanisms of NOD2's effect on CD pathogenesis are still unclear, although several researchers have proposed several hypotheses. The first hypothesis suggests that the ability of variant NOD2 to detect MDP ligand is impaired, resulting in a "loss-of-function" phenotype (Inohara, Ogura et al. 2003). The second hypothesis suggests that NOD2 polymorphisms of Crohn's disease are defective to recruit ATG16L1 for bacteria-induced autophagy (Travassos, Carneiro et al. 2010). The last hypothesis claims that NOD2 variants lose the ability to regulate TLR signaling, resulting in enhanced inflammation (Kim, Shin et al. 2016). Presently, many efforts have been made to modulate signaling pathways that are dependent on NOD1 and NOD2 for maintaining homeostasis between excess inflammation and pathogen clearance, which can be applied to diseases such as CD and early onset disease (EOS) (Caruso, Warner et al. 2014). Small molecules are being developed to counter inflammatory diseases by modulating signalling pathways, including periodontitis

and asthma (Caruso, Warner et al. 2014).

Several studies have exhibited the crystal structure of ubiquitin-bound NOD1 CARD, consisting of 6 alpha-helices, in addition to that of rabbit NOD2ΔCARD (Ver Heul, Gakhar et al. 2014). A hydrophobic core is formed by NOD1 CARD helices containing highly conserved hydrophobic residues of NOD2 CARD (Ver Heul, Gakhar et al. 2014). In NOD1 CARD structure, an antiparallel bundle is formed by 4 helices from the second to the fifth helix. The other two helices, helix 6 and helix 1, are located at the top of the fourth and fifth helix (Ver Heul, Gakhar et al. 2014). Even now, the Tandem CARD structure of NOD2 is still unknown, although NOD2 Tandem CARD shares a high structural similarity with NOD1 CARD to recruit RIP2 by CARD-CARD interaction. The molecular mechanism for how NOD1/2 interacts with RIP2 remains unclear.

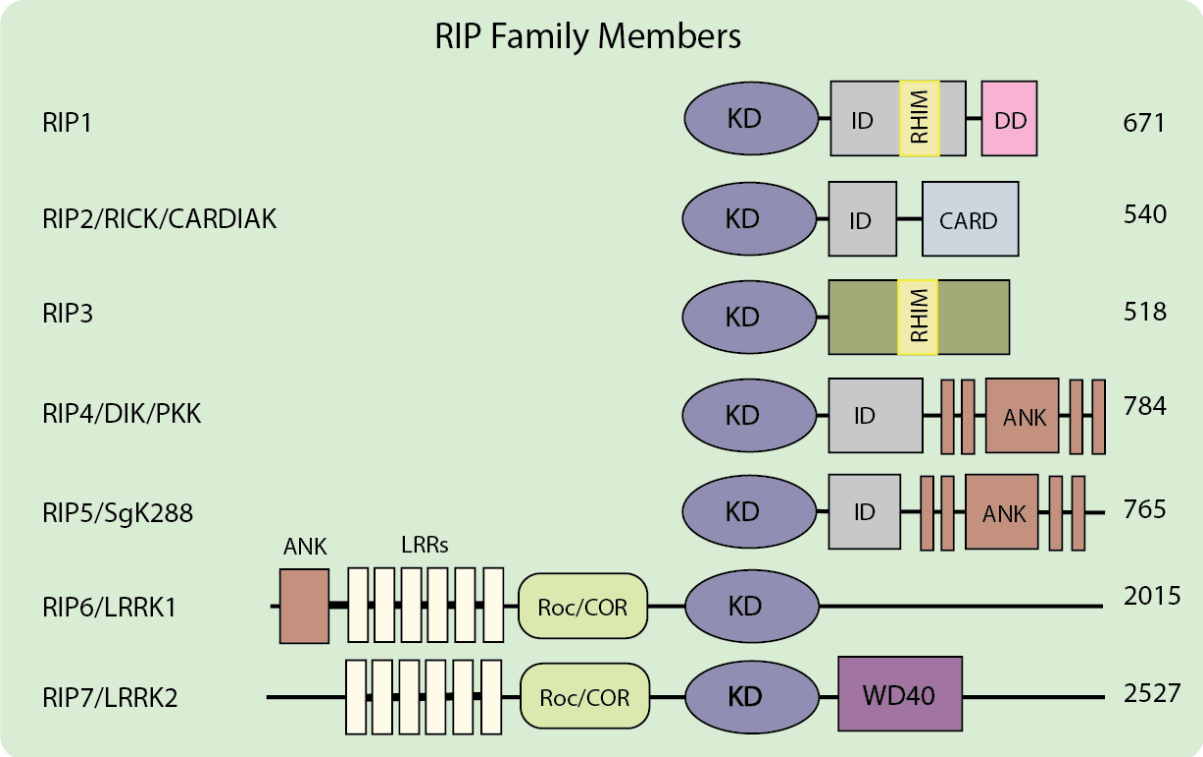

Figure 1.16. Architecture of RIP family members. Abbreviations: KD, kinase domain; ID: intermediate domain; DD, death domain; RHIM, RIP homotypic interaction motif; CARD,

caspase activation and recruitment domain; ANK, ankyrin repeat; LRR, leucine rich repeat; Roc/COR, Ros of complex proteins/C-terminal of Roc domain;

RIP2, as the common adaptor of NOD1/2, contains an amino-terminal serine/threonine kinase domain and a C-terminal CARD domain, belonging to RIP kinase family (Figure 1.16). The seven family members all consist of a conserved kinase domain and other domains for different roles in cellular function. RIP homotypic interaction motif (RHIM) is identified in both RIP1 and RIP3. The RHIM domain is the mediator between the protein-protein interactions, required for the interaction between RIP1 and RIP3. RIP2 has a CARD domain to be recruited by NOD1/2 for signaling pathway. RIP4 and RIP5 share the same structural architecture with an array of C-terminal Ankyrin repeats. RIP6 and RIP7 consist of a leucine-rich repeat motif located in the N-terminus for the recognition of PAMPs and DAMPs. Like other members, RIP2 kinase domain is not necessary for the NF-κB activation, but is for protein stability (McCarthy, Ni et al. 1998). RIP2 kinase (1-310) was purified by *spodoptera frugiperda* (sf9) cells and crystallized to achieve a resolution of 2.4Å (Charnley, Convery et al. 2015). There are two RIP2 kinase molecules that form a dimeric structure in the asymmetric unit of the crystal (Charnley, Convery et al. 2015). The dimer is formed by N-terminal head-to-head interactions. They form an anti-parallel beta strand and C-terminal back-to-back interactions (Charnley, Convery et al. 2015). For RIP2 CARD, the structure is solved by solution NMR, containing six α-helices followed with one short 3_{10}-helix and a C-terminal tail (Lin, Tann et al. 2015). However, the active form of RIP2 CARD is still unknown. The molecular mechanisms of RIP2 activation is required for illustrating how RIP2 induces the downstream signaling.

1.4. NLRC4

NLRC4 was originally identified as an apoptotic protein that activated caspase-1 and named

ICE-protease activating Factor 1 (IPAF1) (Poyet, Srinivasula et al. 2001). After its domain structure was classified into NLR proteins, it was renamed NLRC4 (Sutterwala, Mijares et al. 2007). According to several mouse experiments, NLRC4 could be stimulated by *flagellin* and the inner rod proteins belonging to T3SS found in *S.Typhimurium* (PrgJ), *E.coli* (EprJ), *B.pseudomallei* (BsaK), *Shigella flexneri* (MxiI), and *Pseudomonas aeruginosa* (PscI) (Miao, Alpuche-Aranda et al. 2006, Miao, Mao et al. 2010); however, the direct detection by NLRC4 of these ligands was not observed.

Later, members of the neuronal apoptosis inhibitory protein (NAIP) family – responsible for the detection of pathogens – were identified as being upstream of NLRC4 (Kofoed and Vance 2011). Conserved bacterial ligands such as PrgJ and flagellin are good stimulators to bind with NAIPs, after which activated NAIPs help to form NLRC4-induced inflammasomes (Zhao, Yang et al. 2011). Seven NAIP paralogs are encoded in the mouse genome and only one NAIP in the human genome (Yang, Zhao et al. 2013). NAIPs and NLRC4 share similar architecture, consisting of N-terminal function domain (BIR and CARD), NACHT domain, and C-terminal LRRs (Vance 2015). NAIP1 and NAIP2 are responsible for the detection of the inner rod protein from bacterial T3SS. NAIP5 and NAIP6 prefer to detect bacterial flagellin, including *Salmonella typhimurium* FliC (Zhao, Yang et al. 2011)(Figure 1.17). Cellular roles and functions of NAIP3, NAIP4, and NAIP7 remain to be discovered. Human NAIP detects the needle protein of T3SS from PrgI (Figure 1.17). NAIP proteins sense the existence of T3SS from infectious bacteria and trigger the formation of NLRC4-dependent inflammasomes, which further recruit caspase-1 to induce an inflammatory cell death, called pyroptosis, or process the cleavage and maturation of cytokines for immune responses.

Until now, NLRC4 homologues NAIP2 and NAIP5 have been demonstrated to activate NLRC4 (Gong and Shao 2012). Two types of inflammasomes have been associated with

NLRC4, including PrgJ primed NAIP2/NLRC4 and flagellin stimulated NAIP5/NLRC4 complexes, which further recruit procaspase-1 and thus cause pyroptosis independent of ASC (Zhao, Yang et al. 2011) (Figure 1.17).

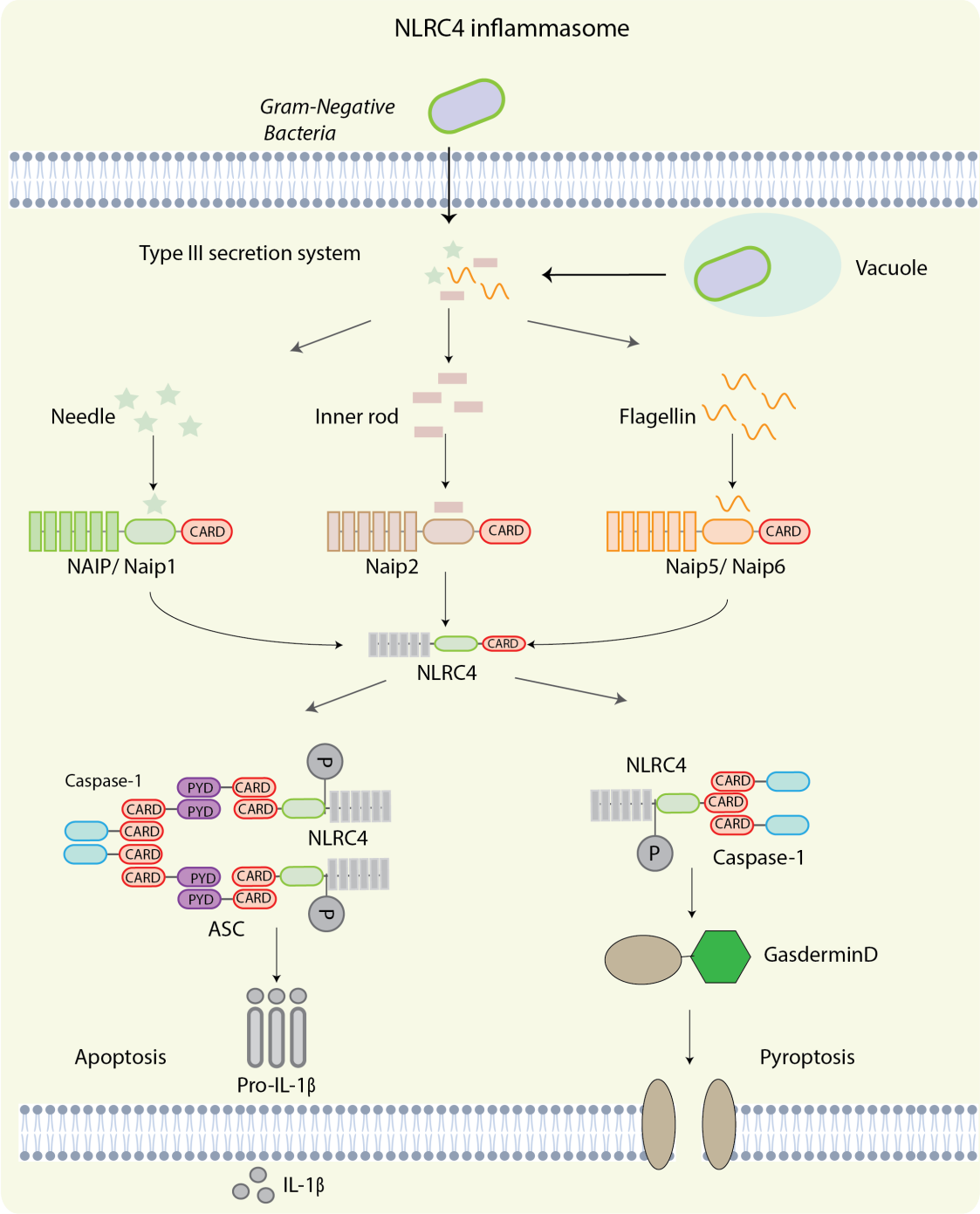

Figure 1.17. Activation of NAIP-NLRC4 inflammasome. The Type III secretion system is secreted by bacteria to invade cells. The T3SS needle proteins, inner rod protein, and

flagellin are detected by NAIPs to activate the NLRC4 inflammasome, which results in the pyroptosis and the maturation of IL-1β via an ASC-dependent mechanism.

Like other NLRs, NLRC4 directly interacts with ASC to induce the formation of ASC specks that recruit caspase-1 for proteolytic cleavage of IL-18 and IL-1β (Miao, Mao et al. 2010). It is still uncertain that Pkcδ, for NLRC4 inflammasome assembly in the presence of T3SS pathogens, induces the phosphorylation of NLRC4 at the site of Ser533 (Qu, Misaghi et al. 2012, Suzuki, Franchi et al. 2014).

According to three human genetic studies, NLRC4 gain-of-function mutations contributed to enterocolitis and auto-inflammation syndromes (Canna, de Jesus et al. 2014, Kitamura, Sasaki et al. 2014, Romberg, Al Moussawi et al. 2014). In the first report, there were several patients from the same family who suffered from syndromes of autoinflammation and enterocolitis caused by NLRC4 mutation of p.V341A, located at the HD1 domain (Romberg, Al Moussawi et al. 2014). In the second report, a patient had a p.T337S mutation of NLRC4 located in the NBD domain and experienced recurrent fever, splenomegaly, and other syndromes (Canna, de Jesus et al. 2014). The last report featured five patients of the same family who suffered from dermatitis and arthritis, and had heterozygous missense mutations (Kitamura, Sasaki et al. 2014). These three reports show that gain-of-function NLRC4 variants lead to spontaneous or excess activation of NLRC4-dependent inflammasome formation for, and enhanced production of chemokines in, monocytes and macrophages (Rathinam, Vanaja et al. 2012). These reported NLRC4 variants indicate that it is meaningful to understand the molecular mechanisms for how NLRC4 regulates innate immune responses.

Since 2015, several structures associated with NAIP/NLRC4 complex have been solved. In the work of L. Zhang, they assembled two complexes, including Flic-activated NAIP5/NLRC4 complex and PrgJ-activated NAIP2/NLRC4 with CARD-deleted NLRC4

(NLRC4Δ) complex (Zhang, Chen et al. 2015). The EM micrograph of NAIP/NLRC4 inflammasome showed that the majority of FliC/NAIP5/NLRC4Δ complexes and PrgJ/NAIP2/NLRC4Δ complexes formed complete disk-like particles, with a single NAIP in each complex, as confirmed by the labeling of Ni-NTA gold particles with NAIP (Li, Fu et al. 2018) (Figure 1.18b).

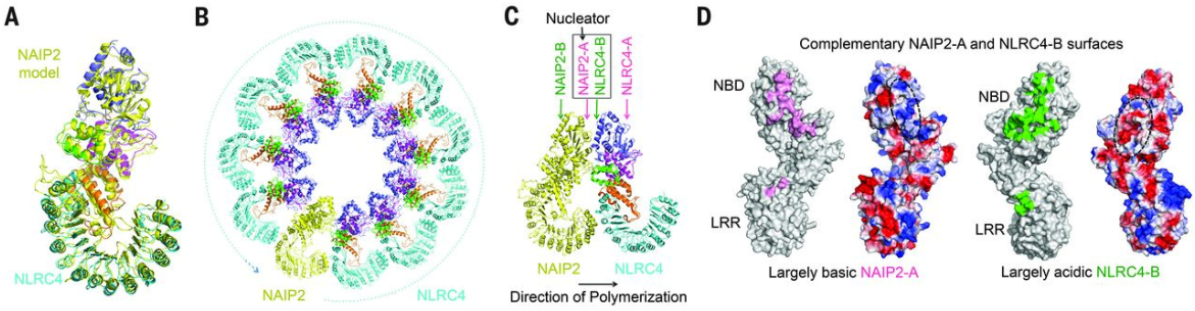

Figure 1.18. Structure of NAIP2/NLRC4ΔCARD inflammasome, adapted from (Zhang, Chen et al. 2015). (A) Superposition the active conformation of NAIP2ΔBIR and NLRC4ΔCARD. (B) The 11-bladed NAIP2-NLRC4 inflammasome disk model. (C) The A and B surface locations in NAIP2 and NLRC4. (D) Charged surface of NAIP2-A and NLRC4-B for interaction direction.

Cyro-EM was used to collect data from PrgJ/NAIP2/NLRC4Δ due to its highest NLRC4Δ ratio and more complete disks (Li, Fu et al. 2018). After data analysis, most of the PrgJ/NAIP2/NLRC4Δ disks were 11-bladed, with some 12- and 10- bladed complexes. 3D classification yielded three different symmetries – C10, C11, and C12 – with C11 symmetry achieving the highest resolution of 4.7 Å (Zhang, Chen et al. 2015). The final PrgJ / NAIP2 / NLRC4Δ model showed that the complex contained an inner ring and an outer ring (Zhang, Chen et al. 2015). However, due to low resolution and a similar domain of NAIP2 and NLRC4Δ, the 11 individual blades did not show the evident difference (Zhang, Chen et al. 2015) (Figure 1.26A). Compared to inactive NLRC4Δ, active NLRC4Δ undergoes a

conformational change to form the 11-bladed inflammasome (Zhang, Chen et al. 2015). Via alignment of these two states of NLRC4Δ by NBD-WH1 region, it is clearly observed that an obvious rotation of about 87.5° occurs for the domains of WHD-HD2-LRR along an axis at the junction between HD1 and WHD. The conformational change makes intramolecular interactions possible for the NBD-HD1 module and WHD (Zhang, Chen et al. 2015). To understand how NAIP2 and NLRC4 interact with each other in the disk, the surface area per unit was calculated and showed that the NAIP2-A (one surface), which is mainly acidic (NBD and WHD), interacted with NLRC4-B (opposing surface containing NBD, HD1 and WHD) (Zhang, Chen et al. 2015) (Figure 1.18c). The directional formation of an inflammasome disk was initialized by their interaction and decided by the different charged interfaces A/B (Figure 1.18D).

To further understand the full-length NLRC4 inflammasome, cryo-electron tomography was used to get a good resolution of flagellin-induced NAIP5/NLRC4 multimers at 4 nm Å (Zhang, Chen et al. 2015). Eleven or twelve units of particles formed the disk-like multimers with varied length in a left or right-handed helical symmetry (Diebolder, Halff et al. 2015). In the multimers, NLRC4 CARD was located in the center to form a helical structure (Figure 1.18). The density map showed that the averaged right-handed 3D-class had the highest resolution and provided sufficient structural information for determining and refining helical symmetry parameters (Diebolder, Halff et al. 2015). The final density map exhibited the parameters of the right-handed multimer of Flic/NAIP5-PKG/NLRC4 complex with a diameter of 28nm and a pitch of 6.5nm. The helical parameters were determined and refined with a twist of 5.57±0.34Å and 30.9° of rotation angle for single helical symmetry, which was aligned with the observation of 11 or 12 units in the disks for 11.65 units per turn (Diebolder, Halff et al. 2015). The averaging density map revealed that the center of the structure contains a rod-shaped core that is formed by NLRC4 CARD; due to insufficient resolution,

the details of the rod are unclear (Diebolder, Halff et al. 2015). The outer helical rim consists of the NACHT domain and LRR domain of the NLRs (Figure 1.19).

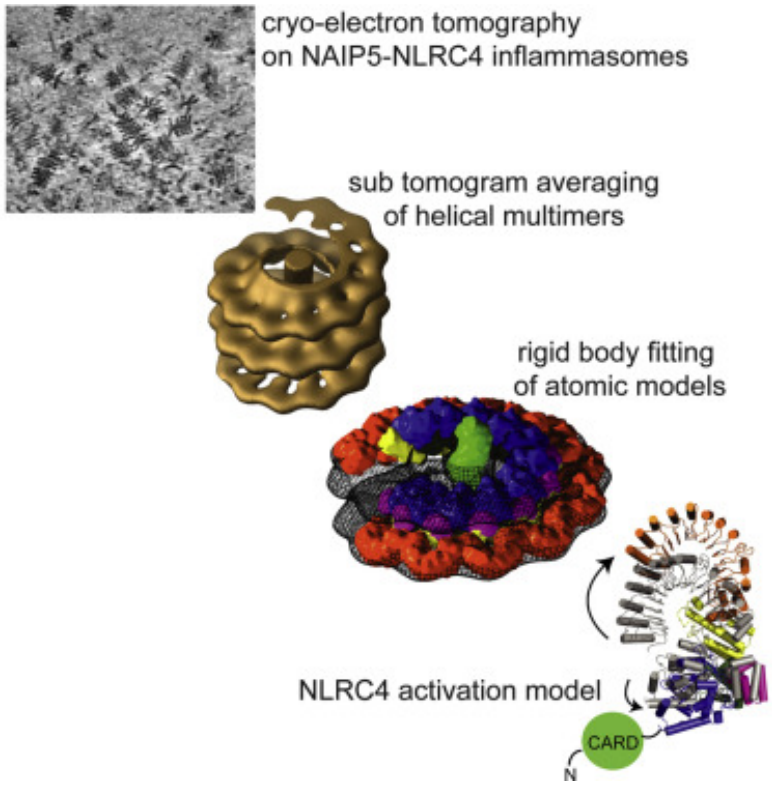

Figure 1.19. Activation model of NAIP5-NLRC4 inflammasome, adapted from (Diebolder, Halff et al. 2015). The raw images of NAIP5-NLRC4 inflammasomes by cryo-TM, averaged to form helical multimers. Different colors are used to differentiate the location of NLRC4 domains in the inflammasome.

In this model, NLR subunits are conformationally changed from a dormant to active state, according to the EM density map, which aligns with the results of the PrgJ/NAIP2/NLRC4Δ disk model (Diebolder, Halff et al. 2015, Zhang, Chen et al. 2015). Compared to a dormant state, active NLRC4 in the model reveals significant structural differences: the LRR domain is rotated 49 degrees, and the NBD-HD1 segment is also rotated 21 degrees when compared to the WHD-HD2 fragment (Zhang, Chen et al. 2015). This conformational change creates an "open lock" within the NACHT domain of NLRC4 for the formation of inflammasomes,

which is different from that in the formation of apoptosomes (Diebolder, Halff et al. 2015).

Here, we further discuss the molecular structure of NLRC4. In 2013, the crystal structure of a mouse NLCR4 mutant with the CARD (1-89) and the internal deletion (622-644) called mNLRC4Δ was obtained to achieve a resolution of 3.2Å (Hu, Yan et al. 2013). According to the experimental data, the mouse NLRC4 can be activated and functional with the internal deletion (Hu, Yan et al. 2013). The structure of mNLRC4Δ resembles an inverted question mark (Hu, Yan et al. 2013). According to the observation of mNLRC4Δ crystal structure, the interaction between NBD and WHD is mediated by ADP binding, which is key for stabilizing the dormant state of NRLC4 (Hu, Yan et al. 2013). Plus, the NBD domain is tightly occluded with LRRs to maintain NLRC4 in a monomeric state, and NLRC4 can be activated by either disruption of ADP-mediated NBD-WHD or NBD-LRR interactions (Hu, Yan et al. 2013). This crystal structure provides insight into the autoinhibition mechanism of NLRC4 (Hu, Yan et al. 2013). However, the information about the molecular structure of active NLRC4 is still unclear. For a better understanding of NLRC4 associated diseases, one must determine how the active state of NLRC4 mediates downstream signaling pathways. NLRC4 CARD acts as the driving force to form oligomeric state NLRC4; therefore, it is crucial to solve the oligomeric structure of NLRC4 CARD.

1.5. Development and Principles of Electron Microscope

During my PhD research, my approach to studying PRRs is through biochemical and structural studies of the protein complex in immunity, and in particular, helical reconstituting the signal complexes. Activated and overexpressed PRRs are purified to observe under the electron microscope (EM). To achieve high-resolution structures of active PRRs, cryo-EM method is adopted to obtain data of high quality for helical reconstruction. As such, it is vital to have a study about development and principle of electron microscopy. The basic principle

of EM is that a beam of accelerated electrons passes through the specimen to form an image. Electrons encounter with the specimen, and their interaction scatters electrons depending upon the thickness or refractive index of different parts of the specimen. These scattered electrons carry with information of the specimen and form a final magnified image with condensers and objective lenses, which lays a foundation for high-resolution structures.

Cryonic electron microscopy

Cryonic electron microscopy also called as cryo-EM is based on the principle that sample is imaged by a transmission electron microscope (TEM) under cryogenic conditions (Fernandez-Leiro and Scheres 2016). In structural biology, the researchers have been dedicated about more than forty years to establish the electron microscopy system including electron-magnetic condensers, CCD camera, and software (Milne, Borgnia et al. 2013). With their efforts, modern cryo-EM is built to obtain high-resolution structures of many proteins and molecules. Presently, the structures solved by cryo-EM is growing in an exponential order recently. The most significant advantage of cryo-EM is to deal with complicated complexes with large size, flexible regions or heterogeneous proteins which cannot be solved by NMR or X-ray crystallization (Bai, McMullan et al. 2015).

The electron gun consists of a cathode and an anode to form thermionic emission from a filament, which is heated by the passage of a current above 2800k and remains at a high negative potential to the anode (Humphreys, Beanland et al. 2014). Electrons emitted from the filament are accelerated by the acceleration anode towards the microscope column, which is then controlled by lenses and condensers (Humphreys, Beanland et al. 2014). In the electron gun, the electrons are accelerated across a potential difference of tens or hundreds of kilovolts to generate a beam of electrons of controlled energy (Humphreys, Beanland et al. 2014). The accelerated electrons are controlled by electromagnetic lenses to obtain a parallel beam (Humphreys, Beanland et al. 2014). The parallel beam hits on the specimen, different

interaction between electrons and specimen can occur (Figure 1.20).

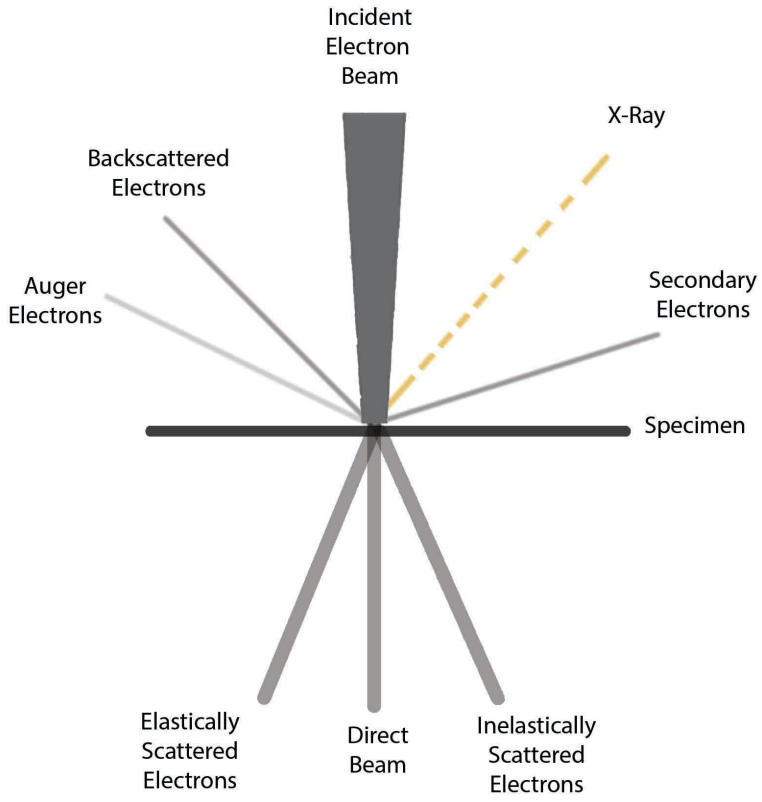

Figure 1.20. Scheme of different electrons arising from the impact of an electron beam onto a specimen. The incident electrons are refracted and scattered to different types of electrons including elastically scattered electrons, direct beam, inelastically scattered electrons, auger electrons, backscattered electrons, X-ray, and secondary electrons.

The interactions are classified into two different types called elastic and inelastic interactions (Krumeich 2011). For elastic interactions, there is no energy transferred from the electron to the sample. No energy is transferred if the electron passes the specimen without any interaction. These electrons contribute to the direct beam, which contains all the electrons in the direction of the incident beam (Figure 1.20). The energy transferred to the specimen can be transformed into different signals including X-rays, Auger electrons, secondary electrons and backscattered electrons (Krumeich 2011). Due to the scattering, the phase and amplitude of the electron waves vary, which is the prerequisites for the imaging of TEM (Krumeich

2011).

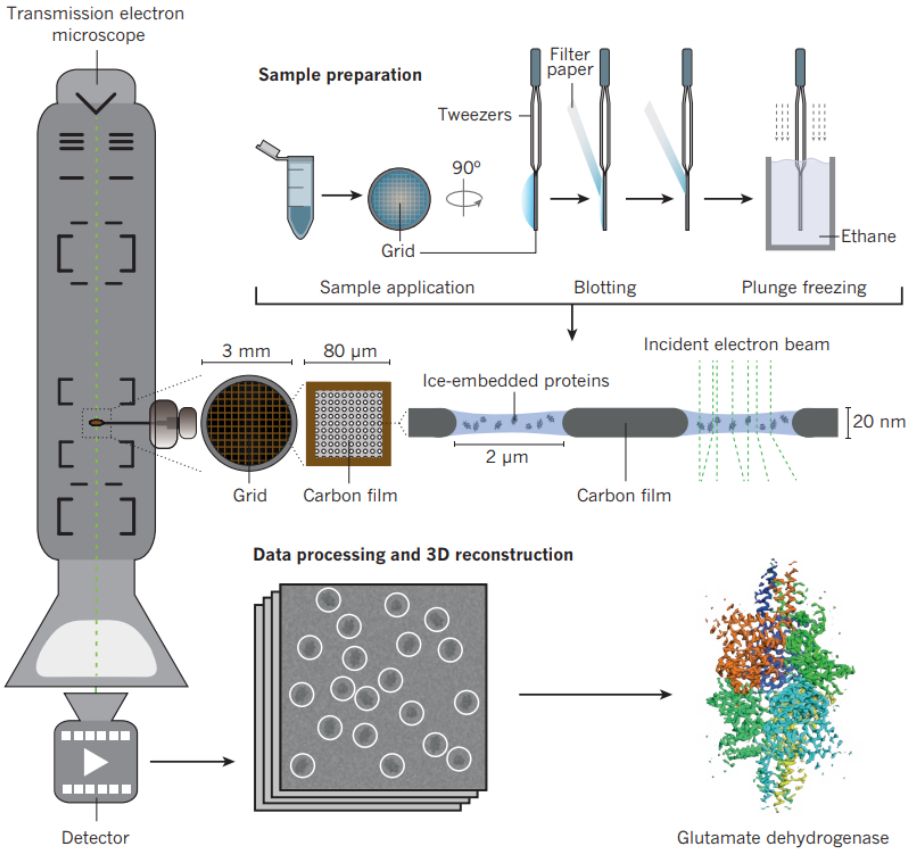

Figure 1.21. Stages of protein structure determination by cryo-EM, adapter from(Fernandez-Leiro and Scheres 2016). A purified protein solution is applied to a grid, which is plunged into liquid ethane to form vitreous ice. The cryo-grid is imaged, and data is collected for a 3D reconstruction of the protein's structure.

The electron waves exit from the specimen contains sample information is used to form an image. The observed image depends on the amplitude of the beam and the phase of the electrons(Williams and Carter 1996, Krumeich 2011). At high magnification, high-resolution imaging requires thinner samples and higher energies of incident electrons because samples are modelled as an object to modify the phase of the incoming electron waves (Williams and Carter 1996). In order to improve the contrast in the image, the TEM is usually operated at a

slight defocus to enhance contrast, due to convolution by the contrast transfer function of the TEM (Humphreys, Beanland et al. 2014).

It is a delicate way to prepare a sample for cryo-EM. The sample of cryo-EM is frozen extremely rapid to embed samples in vitreous ice evenly (Fernandez-Leiro and Scheres 2016). Water is crystallized to form ice-crystal if the freezing speed is slow or the temperature is increased above the devitrifies point about -137ºC (Fernandez-Leiro and Scheres 2016). Furthermore, the quality of the ice is not satisfied if the temperature is above -160ºC. The area of cryo-grid is severely compromised by crystalline ice, resulting in poor quality micrographs (Fernandez-Leiro and Scheres 2016). In total, it is necessary for obtaining good cryo-grids to control environmental factors and blotting conditions (Dobro, Melanson et al. 2010). A thin layer of ice allows particles to be seen clearly by eye and have a good contrast between the molecules and the surrounding ice layer by minimizing the different heights of the molecules in the ice layer, which can help reduce the defocus spread, determining the resolution of structure (Al‐Amoudi, Chang et al. 2004) (Figure 1.21).

The cryo-grid is transferred into an electron microscope for imaging and data collection. The data are processed to combine images of the same protein into a 3D reconstruction of the protein's structure. Presently, there are two kinds of ways to do reconstruction, including single-particle reconstruction and helical reconstruction.

Single particle reconstruction

Presently, the most popular structural analysis method for cryo-electron microscopy is single-particle reconstruction. Many efforts have been put to explore the structural reconstruction of EM data until the publication of *Escherichia coli* ribosome at a resolution of 25Å (Frank, Zhu et al. 1995, Stark, Mueller et al. 1995). For the 3D reconstruction of biological molecules, the theory is based on the different orientations of identical structure to reconstruct a density with

iterative runs for the best parameters (Frank 2009). The 3D reconstruction is achieved by processing numerous 2D projection images to average the same copies of different orientations of protein complexes (Frank 2009). Different 2D classes are combined to rebuild a 3D reconstruction model of protein assemblies based on their common lines in Fourier space (Frank 2009). In order to obtain a good dataset from single particle cryo-EM, it is crucial to collect good quality of micrographs which contain molecules at a high density and with different orientations (Frank 2009). With the development of direct detectors and the movie frames recording, a lot of algorithms and software packages are designed and adopted to yield near-atomic resolution protein models including SPIDER, EMAN2, SPARX and RELION (Frank 2009, Scheres 2012).

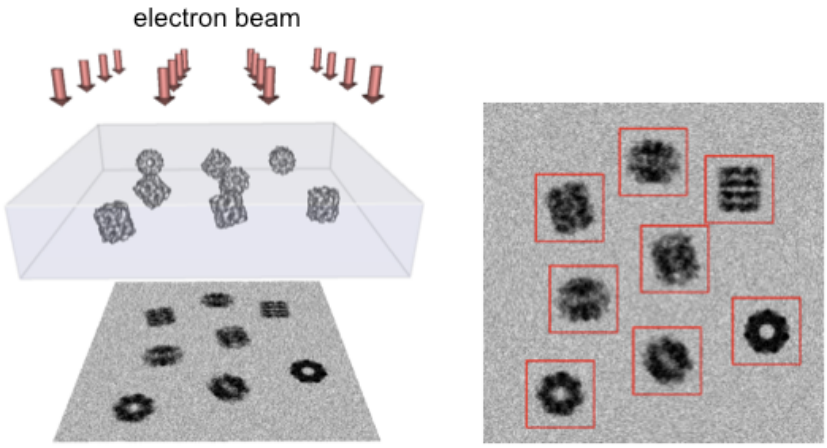

Cryo-EM imaging (left) and boxing (right)

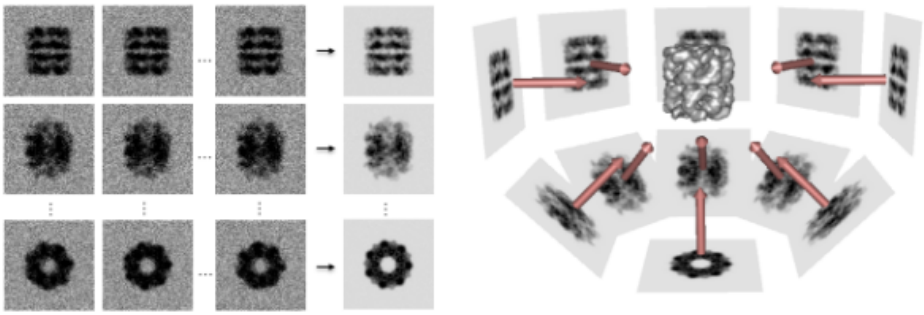

Cryo-EM clustering (left) and back-projection (right)

Figure 1.22. The schematic of single-particle 3D reconstruction, particle imaging, particle selection, 2D classification and 3D reconstruction, adapted from (Yu, Yan et al. 2015). Particles are embedded in the grids and imaged with different orientations. Different orientations are classified into different 2D classes, which further are used to reconstruct 3D classes.

Before a reconstruction is performed, the individual particles embedded in the vitreous ice have to be selected by the program for particle selection manually or automatically (Ludtke, Baldwin et al. 1999) (Figure 1.22). With corresponding coordinates, these programs extract the small regions of micrographs to classify into particle images (Sigworth 2016). In order to obtain a better signal-to-noise ratio of molecules, similar particles are clustered, a process called 2D classification. In general, secondary-structure elements like α-helix and other obvious features can be observed in the averaged images with good datasets (Sigworth 2016). The commonly used software of 2D classification is Relion2 which is based on the theory of maximum likelihood (Scheres 2012).

The 2D classification starts with a 'reference' image, computed with each particle images in its rotation, translation to form the data of probabilities. The average images are formed by the combination of the translated and rotated particle images and are regarded as the new references to select particles again from the previous data pool. In order to obtain the optimized classes, this process is iterated again and again until the representative images are shown. By this way, 2D classification gives an initial overview of the quality of a dataset and provides with different viewing directions of particles (Scheres 2012) (Figure 1.22).

In principle, the classification of 3D models is based on statistical weighting, similar to the 2D classification of images (Sigworth 2016). There is a problem that each particle image contributes to several different 3D densities based on the probability theory (Shatsky, Hall et

al. 2010). Individual particle image is assigned back to the three-dimensional model by multiple iterations of refinement (Shatsky, Hall et al. 2010), which might still be unambiguous. Different from 2D classification, it is required to input the number of 3D model for data analysis. In order to achieve the best density, several iterations of 3D classification are required to select the best coordinates of particles (Shatsky, Hall et al. 2010).

Helical reconstruction

PRRs contain a lot of helical assemblies of proteins, which perform functions in the innate immune system. In order to obtain a high-resolution density of helical complexes, it is vital to know how to do helical reconstruction with a cryo-EM dataset. In the history of 3D reconstruction, the first biological molecular structure was a helical object, the tail of T4 bacteriophage (De Rosier and Klug 1968, DeRosier and Moore 1970) (Figure 1.23). Compared to asymmetrical molecules, helical objects are much easier to do 3D reconstruction since every single projection contains sufficient information (He and Scheres 2017).

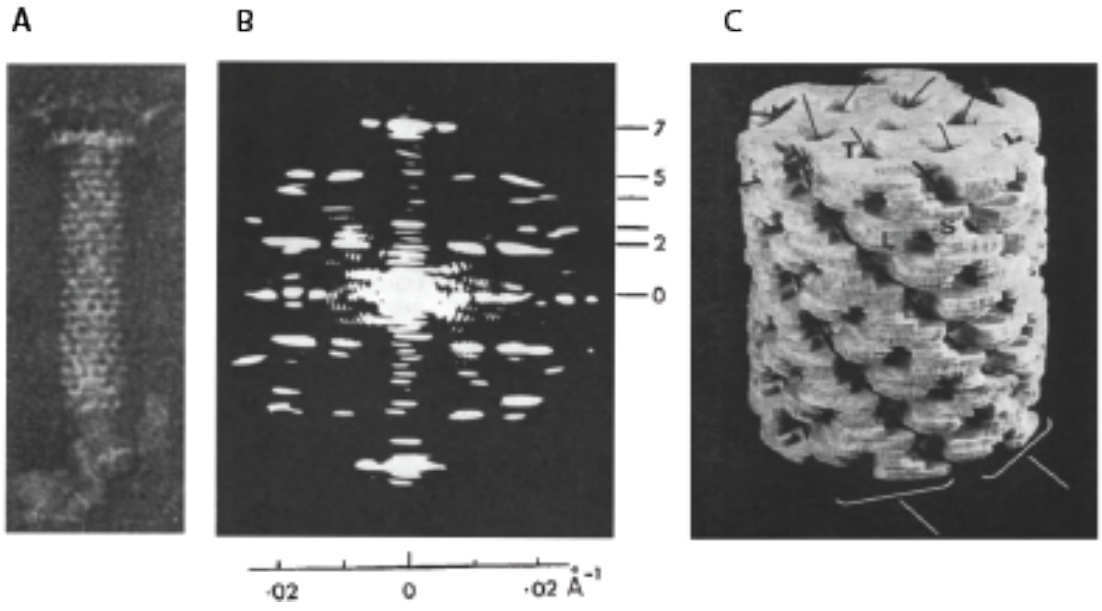

Figure 1.23. The cryo-EM structure of the tail of T4 bacteriophage, adapted from (De Rosier and Klug 1968). (A) Micrographs of a tail of T4 bacteriophage by negative stain. (B) Diffraction pattern of the tail object in image A. (C) the helical model of T4 bacteriophage tail.

Theoretically, the number of parameters required by a helical reconstruction is significantly reduced compared to single-particle reconstruction with no or only one symmetry. Specifically, the orientations of single particles for 3D reconstruction are all independent, while asymmetrical subunits in the helical assembly are fixed and have relative orientations (He and Scheres 2017). With suitable helical symmetry, signal to noise ratio is largely improved for helical reconstructions by averaging a massive number of asymmetrical subunits. Different from single particle reconstruction, helical reconstruction is exempted from the preferred orientation problem by lying flat on the specimen support with a 360º range of views (Egelman 2015).

In order to achieve helical real-space reconstruction, it was introduced in 1997 to cut helical filaments into short segments by a method of Fourier-Bessel reconstructions (Beroukhim and Unwin 1997). In 2000, the iterative helical real-space reconstruction (IHRSR) algorithm is developed for a better achievement of segmentations (Egelman 2000). In this approach, filaments are segmented by overlapping boxes at equal intervals with a suitable width. By this way, segments are applied to iterative algorithms in single-particle analysis for 3D helical reconstructions (Egelman 2000). When representative 2D images from all segments are determined, good particles are selected and aligned for helical 3D reconstruction by back-projection for several iterations (He and Scheres 2017). During this process, the vital parameters of helical rise and twist are determined and iterated for the best pairs (He and Scheres 2017). In this way, 3D density can be obtained for refinement.

1.6. Aims of the Thesis

In the human immune system, bacterial and viral pathogens are detected by corresponding PRRs. Once the substrates are sensed by PRRs, they amplify and propagate the danger signals to their downstream adaptors proteins to induce inflammatory responses. In the presence of bacteria ligands, NOD1/NOD2 respond to the signals and further recruit their common adaptor protein RIP2 by CARD-CARD homotypic interactions for signal propagation. In this way, they form a signaling platform to integrate the signals from more than one upstream PRRs and induce the activation of downstream effector proteins. Whereas, NLRC4 activates at least two downstream adaptors, ASC and Caspase-1 after recognition of invading pathogens. So there are two typical and distinct types of signaling pathways, convergent and divergent signaling, both via CARD-CARD interactions. In this thesis, I focus on the NLRs family, including NOD1/2, and NLRC4 to characterise their different signalling pathways by via the following aims.

Specific aims:

1) Provide structural and functional characterisation of NOD1/2 common adaptor RIP2 to understand how RIP2 is activated by NOD1/2 and propagates immune signals to downstream signaling pathways.
2) Provide structural and biochemical characterisation of NLRC4 CARD oligomer to demonstrate how NLRC4 oligomerizes to activate caspase-1 and ASC by CARD-CARD interaction.

Chapter 2. Materials and Methods

2.1. Molecular Cloning and Site Directed Mutagenesis

Mammalian cell expression plasmids

NOD1 full-length (1-953, synthesized by Creative Biogene), NOD2 full-length (1-1040, synthesized by Creative Biogene) and RIP2 full-length (1-540, cDNA from MegaMan Human Transcriptome Libraries) were cloned into pcDNA3.1 vector between the HindIII and XhoI restriction sites. For CARD domain cloning work, NOD1-CARD (residues 1-110)-SNAP, NOD2-CARD (residues 28-220)-SNAP and SNAP-RIP2 CARD (residues 432-540) were inserted into pcDNA3.1 vector by HindIII and XbaI restriction sites. For all the cloning work in the thesis, their primers were listed in the appendix. To clone these constructs, Q5 PCR KITS (provided by New England Biolabs) was used to set up a PCR reaction from Integrated DNA Technologies (IDT) to amplify targeted DNA inserts. The 50ul reaction volume contains ~50ng DNA template plasmid, 1 ul of forward and reverse primers at 10 uM, 11.5 ul Q5 KITS reagents and topped up with water. The template double DNA strands were separated by heat to 98ºC for 3 to 5 minutes, following with 20-30 amplification cycles. The cycle includes 10 seconds denaturation at 95ºC, 30 seconds annealing at Tm temperature ± 5 ºC and 1-2 minutes extension at 72 ºC. The final extension was at 72 ºC for 10 minutes. After PCR, the reaction sample was loaded into 10% agarose gel to check its size and homogeneity. The right band of the gel was cut out for further purification. The purified inserts are digested with restriction enzymes for 2 hours in 37 ºC incubator. The digested inserts were purified again and then ligated with digested backbones, which were transformed into transformation competent *E. coli* - DH5α. The transformation reaction was recovered by adding 0.5ml LB and incubated at 37 ºC for 1 hour. The sample was plated on LB agar plate supplemented with respective antibiotic and incubated at 37 ºC overnight. The positive

colonies were picked and grown within LB for overnight with respective antibiotics. The plasmids were extracted and sent for sequencing.

Recombinant protein plasmids

To generate the CARD-SNAP fused constructs, SNAP-tag was inserted between the EcoRI and XhoI restriction site into Pet47b (provided by Novagen). The NOD1-CARD, NOD2-CARD, RIP2 CARD and NLRC4 CARD (1-102) were inserted between the XmaI and EcoRI restriction sites. To obtain single straight RIP2 filament instead of bundles for better structural analysis, two approaches were taken including add 13 extra amino acids-VDEALREAQTKSA-named 13aa to the N-terminal of RIP2-CARD and remove the flexible C-terminal tail of RIP2 CARD (residues 432-529). The optimized 13aa-RIP2 CARD (432-529) gene was cloned into pSnap-tag (T7)-2 vector (provided by New England Biolabs) between the EcoRI and NotI restriction sites after the SNAP-tag. For NLRC4 CARD filamentous structure, a flag-tag was inserted between NLRC4 and SNAP to make NLRC4 CARD more flexible to form a filament. These constructs were cloned in the same way as described above.

Plasmids mutagenesis

For all the mutagenesis work in this thesis, KAPA Hifi PCR KITS (KAPA Biosystems) was used to set up PCR reaction with primers from IDT and targeted template plasmids. The 13 ul reaction volume contains ~50ng template plasmid, 0.5 ul of forward and reverse primers at 10 uM, 3 ul KAPA KITS reagents and topped up with water. The template double DNA strands were separated by heat to 95ºC for 3 to 5 minutes, following with 20-30 amplification cycles. The cycle includes 30 seconds denaturation at 95ºC, 45 seconds annealing at Tm temperature ± 5 ºC and 5 minutes extension at 72 ºC. The final extension was at 72 ºC for 10 minutes. After PCR, 1ul Dpn1 enzyme (New England biolab) was added to 5ul reaction sample with

10ul water and incubated at 37 ºC for two hours. The reaction was transformed into transformation competent *E. coli* - DH5α. The transformation reaction was recovered by adding 0.5ml LB and incubated at 37 ºC for 1 hour. The sample was plated on LB agar plate supplemented with a respective antibiotic and incubated at 37 ºC overnight. The positive colonies were picked next day and grown in 3ml of LB with the respective antibiotic. Plasmids were extracted the following day and mutagenesis was confirmed by sequencing.

2.2. Expression and Purification

For the expression of His-tagged recombinant proteins, the plasmids were transformed into competent *E.coli*–BL21 cells. After 45 seconds of heat shock, the samples were added into lysogeny broth (LB) with a complementary antibiotic for 16-18 hours. The starting culture was transferred into 2L LB with antibiotic and grown until OD600 about 0.6 ~ 0.8 at 37 ºC, then the temperature was adjusted to 16 ºC and cells were induced with 0.5mM IPTG for the overexpression of the recombinant proteins for overnight. The next day, cultures were harvested by centrifugation at 4000g (Avanti JXN series, Beckman Coulter) for 20 minutes at 4ºC. Cell pellets were collected and resuspended with lysis buffer (20mM Tris-HCl, pH8.0, 300mM NaCl, 20mM imidazole, and 10% glycerol). Cells were then lysed by Emulsiflex-C3 for 3-4 cycles and spin down by centrifugation at 30,000g (Avanti JXN series, Beckman Coulter) for 30 minutes at 4 ºC. In the way, the soluble fraction was separated from the pellet and collected for further protein purification. Ni-NTA agarose beads (Qiagen) were incubated with lysis buffer and then added into the soluble fraction for incubation for 1 hour at 4ºC. The 6xHis-tagged protein bound to the Ni-NTA beads were retained on the column bed. The beads then were washed with lysis buffer for more than 200 ml and eluted with elution buffer containing imidazole (100mM, 150mM, 200mM, 250mM, and 300mM). To further purify the recombinant proteins, size-exclusion chromatography (Superdex 200 increase, GE healthcare) was performed in the buffer (20mM Tris-HCl, pH8.0, 150mM NaCl, and 1mM

DTT). At this step, the oligomeric peak was collected and the purified proteins were prepared as active seeds of CARD containing proteins. These seeds were carefully collected and flash frozen with liquid nitrogen in small aliquots for further experiments.

2.3. Oligomerization Assay

The purified CARD domain proteins (NLRC4 CARD or RIP2 CARD) were collected and concentrated to ~10 mg/ml. Each 200ul concentrated seeds were mixed with 1.3ml 7M Guanidine hydrochloride (Sigma-Aldrich) which was then incubated at 37ºC shaker for 30mins. The protein sample was transferred to 12~14kD tubing (Spectrum Labs) for dialysis against 200ml buffer A for half an hour and 200ml buffer B for 30 mins. Buffer A consists of (20mM Tris-HCl, 3M NaCl, 0.5mM EDTA, 10% Glycerol, 50mM β-mercap), Buffer is consisted of (20mM Tris-HCl, 1M NaCl, 0.5mM EDTA, 10% Glycerol, 50mM β-mercap). After dialysis, the protein sample was collected from tubing bag and spin down for 1 min at a speed of 14,000xg. The supernatant was collected and added with 10ul fresh prepared 0.5M DTT, which was then filtered by 0.25 um syringe filters (Merck millipore). In this way, these proteins were regarded as monomers.

Monomers were labelled with Alexa Fluor 647 (New England Biolabs) and seeds were incubated with Alexa Fluro 488 (New England Biolabs) for 10 mins separately. 1ul of 100uM BG-Alexa dye stocks (dissolved in water containing 5%DMSO) were added into every 100ul of pre-labelled protein stock at a concentration of 20uM. To check whether seeds can interact with monomers, for example, NOD1 CARD and RIP2 CARD, fluorescently labelled monomeric SNAP-RIP2-CARD (10uM) was mixed with 5 or 10uM NOD1-CARD-SANP for 15 mins at room temperature before analysis by Bir-Tris native gel (Life) or 15% SDS-PAGE gel. The double fluorescently labelled gel was run at a voltage of 200V for 1 hour. Then the gels were scanned and visualized by Typhoon FLA7000 (GE Healthcare) with 100um pixel size at channels of Alexa 488 and Alexa 647 with PTM 600.

To assembly CARD long filament (200-500nm), ~20uM monomeric CARD proteins were incubated with unlabelled and active CARD seeds at a molar ratio of 10:1 for overnight to extend to long filaments. Later on, in-house-made 3C protease was added to remove peripheral snap-tag proteins to expose rigid filament for high-resolution structural determination. Digestion process was at the 4ºC for 8 hours. Protease and removal snap proteins were separated from filament after further purification by size-exclusion column Superose 6 (GE Healthcare). In this way, single filaments were ready for structural analysis.

2.4. Cell Culture and Cellular Assay

Luciferase assay

HEK293T cells were plated into 24-well plates (Greiner) 24 hr prior to transfection. Dual luciferase assays were carried out with the dual luciferase reporter assay system (Promega). Cells were harvested 24 hr post transfection and lysed using 1x Passive lysis buffer (Promega). The cell lysates were aliquoted onto 96-well white flat-bottom chimney well plates (Greiner). Luciferase Assay Reagent II (Promega) was firstly added to each well and the plate was read in Tecan plate reader to record luminescence in each sample. Then Stop and Glow® reagent (Promega) was added to each well to quench firefly luciferase activity while allows measurement of luminescence from *Renilla* luciferase by Tecan plate reader.

The dual luciferase system is consisted of two different reporter genes, firefly (*Photinus pyralis*) and *Renilla* (*Renilla reniformis*) luciferase on two separate plasmids. The gene encoding firefly luciferase is under the control of NF-κB promoter and the gene encoding *Renilla* promoter is fused to a constitutive CMV promoter. The two plasmids were cotransfected into each sample with a ratio of 5:1 for NF-κB-firefly vector: CMV- *Renilla* co-reporter vector combinations. Twenty-four hours post-transfection, the cells were harvested, and the activities of luciferases were measured sequentially from a single sample.

The relative light units were first calculated as the ratio of firefly to *Renilla* luciferase activity. Then the data were presented as relative light units of induced cells/relative light units of control cells. The blank control samples in each experiment were cells mock-transfected with empty vectors. For each plot, the data represented the means of three independent assays with the bars indicating standard errors in each sample.

RIP2 knock-out cells

All single guided RNA (sgRNA)-expression vectors were built on the pSpCas9 (BB)-2A-Puro (PX459) V2.0 backbone (Addgene plasmid no. 62988). sgRNAs were designed with the GUIDES web-based CRISPR design tool. As required, DNA sequences for the guides were modified at position 1 to encode a G, owing to the transcription-initiation requirement of the human U6 promoter.

HEK293T cells were transiently transfected with Lipofectamine 2000 (Invitrogen) per manufacturer's recommendations. As demonstrated by Agudelo at el, Ouabain (Sigma) prepared to a concentration of 50mM in DMSO, was added directly to the cells during the culture-medium change at day 4 after the transfection, replenished every 3 or 4 days and maintained for 10 days. Desired clones were enriched in the negative selection screen. HEK293T cells transiently co-transfected with the dual SpCas9 and tandem U6-driven sgRNA expression vectors targeting ATP1A1 and RIPK2 were subsequently used for the downstream experiments. Sequences for SpCas9 guides:

Target	Sequence
ATP1A1 G2	GATCCAAGCTGCTACAGAAG
RIPK2 G1	GATAATGTATAGTGTGTCACA
RIPK2 G2	GACTATTTTCATGGAGCTGAG
RIPK2 G3	GAGATCATACGTGCTCGGTG

RIPK2 G4 GAGTTTCCTGCAGTTGAGAG

Tissue culture and transfection

All cells were maintained at 37°C with 5% CO_2 in DMEM (Gibco) supplemented with 10% (v/v) fetal bovine serum (Gibco). HEK293T cells were plated at a density of 5×10^5 cells per well for poly-L-lysine (Sigma-Aldrich) coated 6 well plate or 1×10^5 cells per well for 24 well plate 24 hr prior to transfections. Plasmids were transfected into HEK293T cells using FuGENE HD (Promega) with a '5:1' ratio according to manufacturer's instructions.

Western blot

HEK293T cells were plated into 6-well plates (Corning) 24 hr prior to transfection. Cells were harvested 24 hr post transfection and lysed using RIPA buffer (150 mM NaCl, 50 mM Tris pH 8, 1 mM EDTA, 1% (v/v) Triton X-100, 0.1% (w/v) Sodium dodecyl sulfate, 0.5% (w/v) Sodium deoxycholate) on ice for 30 min with vortex every 5 min. Cell lysates were centrifuged for 30 min at 18000 g 4^0C, and each component was subjected to SDS-PAGE. Transblotting was done by the Mini Trans-Blot® Cell (Bio-Rad) onto PVDF membrane (Bio-Rad), which was then blocked by 10% (w/v) blocking grade powder (Bio-Rad) diluted in TBST (50mM Tris-HCl pH 7.4, 140mM NaCl, 0.1% Tween20). Next the blot was incubated with primary antibodies in 1x TBST with 5% (w/v) BSA (Biowest) at room temperature for 1hr or 4°C overnight. Secondary antibody incubation was performed for 1hr at room temperature. WesternBright Sirius, femtogram HRP Substrate (Advansta) was added to each blot and left for 1 min. The blot was visualized with Chemi-Doc (Bio-Rad).

Immunoprecipitation

HEK cells transfected with pcDNA3 full-length RIP2 and NOD2 were harvested and lysed using passive 1x lysis buffer. The whole cell lysate was then incubated with anti-FLAG Nanoparticles (Nvigen) at room temperature for 1 h. The beads were collected with magnets and washed three times with wash buffer. The proteins were eluted with 1.5mg/mL 3X FLAG® Peptide (Sigma-Aldrich).

Immunofluorescence

293T cells were seeded at ~70% confluence on poly-L-lysine coated coverslips. All cells were grown in complete media and allowed to adhere overnight. Coverslips were fixed with 3.7% paraformaldehyde in 1xPBS and permeablized with 0.5% Triton-X in 1x PBS. Coverslips were incubated with Alexa Fluor™ 647 Phalloidin (Invitrogen) diluted in PBS with 1% BSA for 30 min at room temperature. DAPI stain was then performed on the coverslips at room temperature for 5 min. Coverslips were mounted with VECTASHIELD HardSet Antifade Mounting Medium (Vector Laboratories).

2.5. Electron Microscopy

Negatively stained EM

The protein samples are diluted to suitable concentration (~0.02mg/ml for single particle, ~0.1mg/ml for oligomeric complexes) and absorbed onto a carbon-coated formvar film which is attached to a metal specimen grid (Electron Microscopy Sciences). The surface of the carbon grid is hydrophobic and is difficult to bind with charged samples. So the grids glow discharged before applying samples onto the grid surface, in this way, electrons are hit the carbon to make the carbon surface hydrophilic in the environment of vacuum chamber of a vacuum evaporator. After about 60 seconds, extra samples are blotted off by filter paper and immediately the grid is covered with 4ul staining solution (2% Uranyl acetate) for another 60 seconds. Extra staining buffer are removed by filter paper. The prepared grids are air-dry for

10 mins and stored in a grid box and labelled properly. These grids were imaged on the Tecnai 12 electron microscope and recorded with an Eagle CCD camera operating at 120kV (Nanyang Technological University Microscopy Facility).

Cryo-EM

For cryo-EM grid preparation, Quantifoil R2/2 holey carbon grid (Quantifoil, R2/2 300 mesh, copper, Electron Microscopy Sciences) was glow-discharged Vitrobot was switched on and set humidity to 100% and temperature to 4 ºC. The quantifoil grid was then secured with a specific tweezer which was attached to the Vitrobot machine. A pre-cooled ethane pot was placed into plunge freezing position on Vitrobot. The grid was treated with 5ul sample at a concentration of about 3mg/ml for 30s, which was then blotted for 2s and plunged into precooled liquid ethane by FEI vitrobot. The grid was then clipped for autoloader and imaged in a FEI Arctica microscope operating at an acceleration voltage of 200kV (Nanyang Technological University Microscopy Facility). Cryonic-EM data were collected automatically on a K2 summit direct detector camera (Gatan) in counting mode. For data collection. Cs = 2.0 mm, and binned 2x when doing motion correction. The sub-frame time is 200 ns and total exposure time was 7 seconds, thus 35 frames per stack. The pixel size on the final image is 1.23 Å. The dose rate is 8e/pixel/s.

2.6. Data Collection, Structure Determination and Refinement

For cryo-EM data, super-resolution image stacks were gain normalized and binned by 2× to a pixel size of 1.23 Å prior to drift and local movement correction using MotionCorr252. Date processing software Relion 2 was used for CTF determination, particle picking, 2D classification, 3D classification, and refinement procedures. Totally, 3100 micrographs were collected and analyzed. We manually picked out ~18,000 filaments and windowed out segments of 220 × 220 pixels, yielding 653,110 particles for 2D classification. After several

iterations, bad particles were removed, and we used 236,877 particles for 3D classification. Ab initio low resolution helical structure was generated using a Gaussian cylinder as an initial model and good 2D class averages, which employed exhaustive searches for orientations of segments that are strictly constrained by the known helical symmetry. This reconstruction served as an initial reference model for 3D classification and auto-refinement in Relion. Finally, 142,230 particles were chosen to calculate our RIP2 filamentous model. All 3D refinements were carried out following the gold-standard procedure where the data set was divided into two half-sets. After refinement was converged, a mask was calculated and applied to the final data set and the corrected Fourier shell correlation (FSC) was calculated to estimate the resolution about 4.1 Å by using FSC = 0.143 criterion. In the final model, parameters of the RIP2 filament were calculated to yield a 4.936 Å of the axial rise per asymmetric unit and an azimuthal rotation per subunit of −101,373°.

Model building

The initial monomer structure model of RIP2-CARD was adopted from PDB 2N7Z, with truncations and modifications reflecting the actual constructs used in this EM investigation. Initial fitting of 12 monomers into the central segment of the density was done using chimera, with local rigid body adjustment. Then the central segment density surrounding the 12 monomers was cropped out and converted to .mtz file for further qseudo-crystallographic statistics analysis. Phenix real space refinement was used to perform refinement to obtain the final PDB model best reflecting the density.

Step 1 was the monomer docking. The RIP2–CARD monomer structure (PDB accession code: 2N7Z) was used at this stage. The residue numbers were renumbered and the terminal residues were deleted to match the length of the density. The individual helix was manually shifted (rigid body movement) according to the locations of three large aromatic side chains.

These three residues (W439, Y474, and F501) are highlighted in the RIP2 filamentous structure. The density map at this resolution enabled us to unambiguously locate these residues. This step was done in Coot.

In Step 2, a tetramer containing the Type I, II, and III interfaces (a centrally located monomer and three other monomers forming Type I, II, and III interfaces with the central one) was built. After building four monomers in this way, we obtained a tetramer that could be used to refine the surface interactions. Phenix real space refinement was done without rigid body refinement. Different parameters were tested, a torsion-rotational angle NCS constraint (Phenix default auto setting) was used at this step. In this way, all surfaces of the central monomer could be refined.

During Step 3, a tetramer model was built that is in agreement with the data from the cellular activity assays, given particular emphasis in charge-reversal experiments.

In Step 4, a 12mer model was built. The central monomer from Step 3 was copy-and-pasted to occupy the entire 60 Å segment density. In the end, 12 identical monomers were added to the density. Phenix real space refinement with default NCS torsion-rotational constraint was performed. After several rounds of refinement, a model with reasonable statistics was obtained. Step 5: final refinement. The clash score was >16 after Step 4 and when inspecting this model in detail, some interactions were rebuilt and then Step 4 was repeated until satisfactory statistics and density interpretation were achieved.

2.7. The experimental workflow and optimization process

For both RIP2 and NLRC4 projects, the experimental method was similar from plasmids design to data processing. The workflow for these two projects was described in Figure 2.1. The constructs were obtained as described above. RIP2-CARD and NLRC4-CARD plasmids were transfected and expressed in competent *E. coli*–BL21 cells. Targeted proteins were

extracted and purified for the refolding experiment to obtain monomeric RIP2-CARD and NLRC4-CARD.

These monomers were further purified by size-exclusion chromatography and then incubated with RIP2-CARD and NLRC4-CARD seeds for the extension of long filaments. These samples were examined by negative staining EM for quality assessment. Constructs optimization was continuously conducted until straight and single filaments were obtained. The optimized filamentous sample was loaded to cryo-grid and examined by cryo-EM. Data was collected by Titan Krios and processed to solve the filamentous structure of RIP2-CARD and NLRC4-CARD.

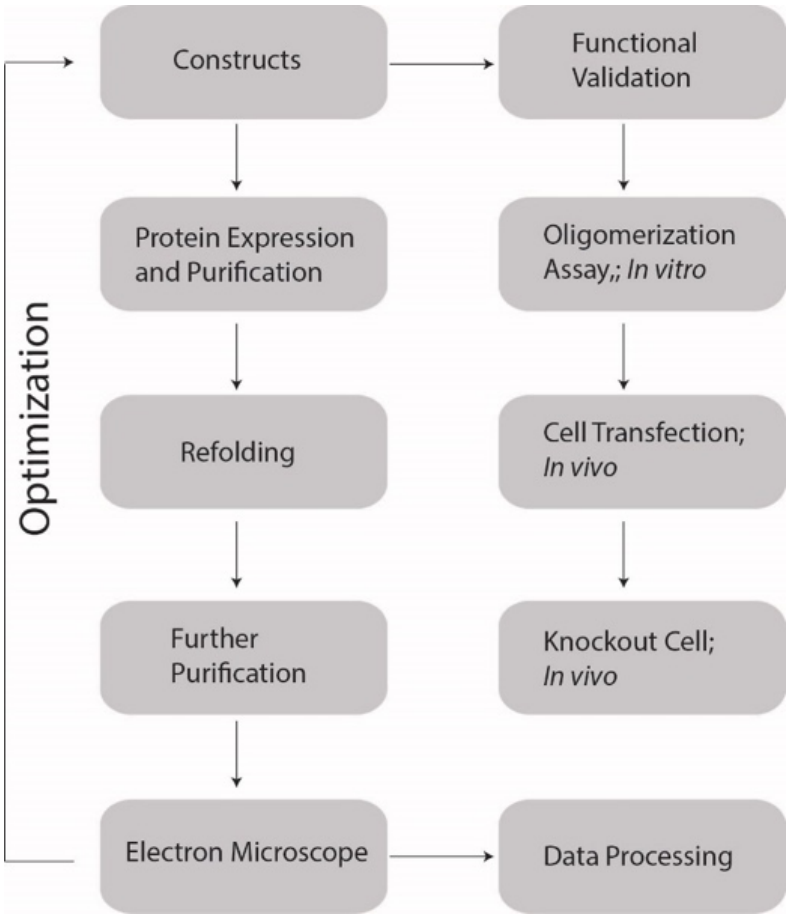

Figure 2.1 Experimental workflow. The constructs were engineered to obtain filamentous structure and examine the function in vivo and in vitro.

These constructs were assessed by biochemical and cellular assays, which demonstrated the function of RIP2-CARD and NLRC4-CARD *in vitro* and *in vivo* and also validated the filamentous structures. RIP2-CARD monomers were examined by oligomerization assay to demonstrate that RIP2 monomers could by induced by NOD1-CARD, NOD2-CARD and RIP2-CARD seeds. For *in vivo* experiments, RIP2 plasmids were transfected into HEK293 cells to confirm its function to activate NF-κB signal. RIP2 knock-out cells were engineered by Crispr-Cas9 technology to show that NF-κB immune signals were dramatically when full-length NOD1/NOD2 were transfected.

For the optimization experiment, many efforts were made to obtain single filament instead of bundling filament (Figure 2.2).

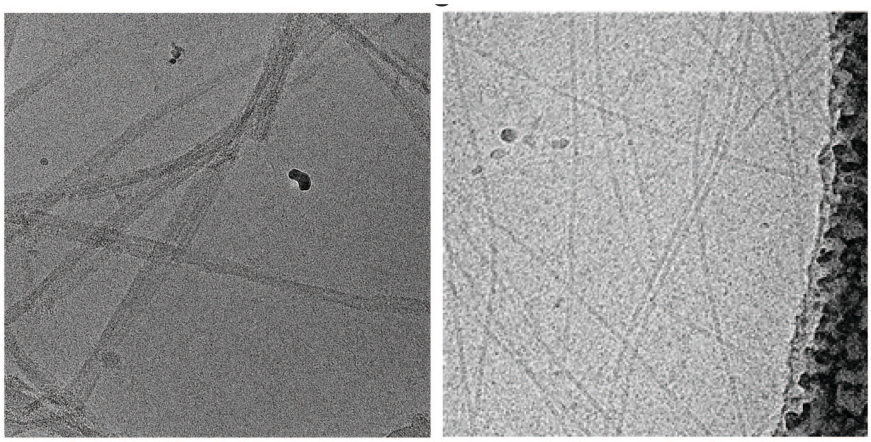

Figure 2.2. RIP2 CARD filaments with different constructs. Left image is bundled RIP2 CARD; Right image is single filaments of RIP2.

In the beginning, RIP2-CARD filaments were constructed from residue 432 to residue 540. Bundled filaments were observed under EM, which was a difficult sample to solve the high-resolution structure. The hydrophobic surface of RIP2-CARD filaments caused the bundling aggregation. To reduce the hydrophobic surface area of filaments, a 13aa tag was inserted into the N-terminal of RIP2 CARD, and a Flag-tag was inserted into the C-terminal of RIP2 CARD; however, the bundling problem was reduced but still existed. The flexible C-terminal tail was carefully examined from residue 522 to residue 540 (EILVVSRSPSLN LLQNKSM).

The C-terminal tail consists of many hydrophobic amino acids. The C-terminal truncated RIP2-CARD was engineered to form filaments. In this way, straight and single RIP2-CARD filaments were achieved and were used for cryo-data collection.

Chapter 3. Structural and Biochemical Characterization of RIP2 in Innate Immunity

3.1. Functional Studies of RIP2 in Signaling Pathway

In PRRs, NOD1 and NOD2 were the first proteins to be well studied in innate immunity; In the presence of invading bacteria, NOD1 and NOD2 recognize peptidoglycans from bacterial cell wall including iE-DAP and MDP, and propagate immune signals to their common downstream adaptor protein RIP2 (Inohara, del Peso et al. 1998, Thome, Hofmann et al. 1998). The architecture of RIP2 consists of two domains: an amino-terminal kinase domain for dimerization and phosphorylation of downstream factors including TAK1 and NF-κB, and a C-terminal domain for oligomerization (Figure 3.1a/b) (Kobayashi, Inohara et al. 2002, Boyle, Parkhouse et al. 2014). It is reported that polymorphisms of NOD1, NOD2, and RIP2 have been associated with inflammatory diseases including Lupus and Crohn's Disease (Franchi, Warner et al. 2009, Caruso, Warner et al. 2014). Besides the role in classical immune responses with NOD1/2, RIP2 is also reported to play an important role in other non-canonical events independently, such as regulating signals for some Toll-like receptors, Autophagy and activation of neuronal cells (Zhang, Wang et al. 2003, Pandey, Yang et al. 2009). Although there are several studies about the function of RIP2 based on computational and cellular assays (Fridh and Rittinger 2012, Maharana, Dehury et al. 2015), the molecular mechanism of how RIP2 is activated by upstream signals is still unknown. These studies have exhibits that there are many disruptive mutations located on the surface areas of NOD1, NOD2, and RIP2 CARD domains. However, it is still unknown whether the first CARD domain or the second CARD domain of NOD2 is responsible for RIP2 recruitment and activation.

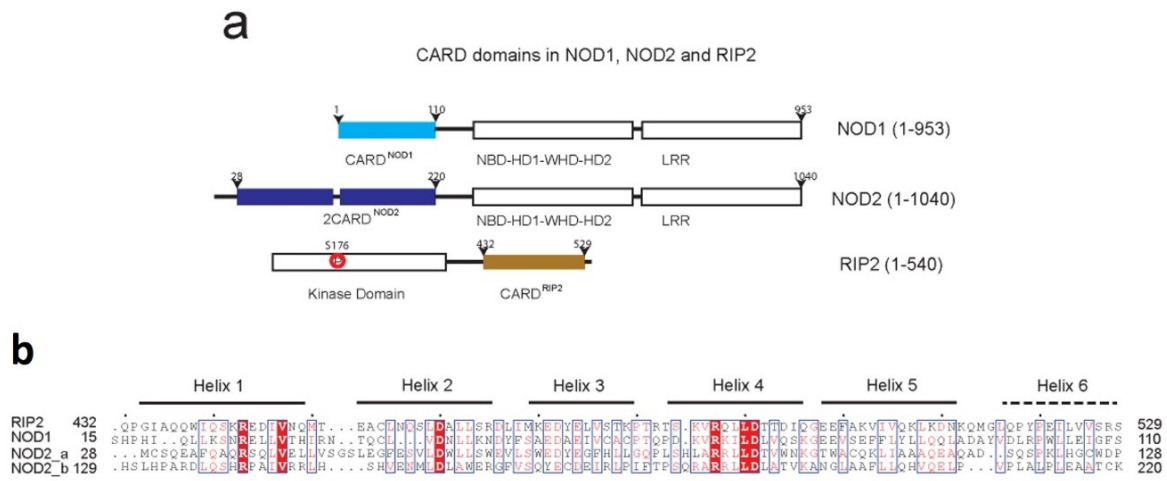

Figure 3.1. Domain architecture of NOD1/2 and RIP2. (a) Illustration of protein domain structure of human NOD1, NOD2 and RIP2. The CARD domains are highlighted in colours (light blue for NOD1 CARD, blue for NOD2 CARD and orange for RIP2 CARD). (b) Sequence alignment of RIP2 CARD, NOD1 CARD, NOD2 CARDa and NOD2 CARDb. Conserved residues are highlighted in red.

There are many efforts using drugs, like ponatinib, to inhibit the RIP2 signaling, however, mostly from the point-of-view of inhibiting kinase activities. Understanding how NOD1 and NOD2 interact with RIP2 would also significantly enhance our understanding of disease-related mutations in these proteins (Vasseur, Sendid et al. 2011). For example, the reported mutations associated with the inflammatory disease are not within CARD domains of NOD1/2 and RIP2, but they indeed participate in the mediation of CARD-CARD interactions for immune responses (Caruso, Warner et al. 2014). Additionally, RIP2 is a typical example to demonstrate how two different upstream proteins converge their immune signals to the same adaptor in innate immunity, similar to the roles of MAVS in the signaling pathway of RIG-I and MDA5. In this way, the mechanism of how innate immune signals are regulated can be elucidated by understanding the activation of RIP2 by NOD1 and NOD2.

Initially, I, with my colleagues, overexpressed human RIP2 in HEK293T cells and extracted RIP2 complexes from cells, which were observed and confirmed to form filaments to

propagate immune signals by the stimulation of NOD1/2. To achieve a high-resolution structure of RIP2 proteins, I reconstituted RIP2 CARD filaments *in vitro* and solved the structure by cryo-EM at a resolution of 3.6 Å. To validate this high-resolution model, mutagenesis and biochemical assays have been conducted.

3.2 CARD domain from NOD1/2 and RIP2 are important for signaling

NOD1 and NOD2 can activate RIP2 to trigger NF-κB signaling pathways. To examine their ability in cells, NF-κB transcriptional activities were monitored to validate the functional roles of CARD domains in NOD1/2 and RIP2. Overexpression of the full-length proteins and the CARD domain constructs (Figure3.2 a/b) triggered NF-κB activation, as measured with a luciferase reporter assay. The luciferase reporter assay is to measure the activation level of NF-κB induced by overexpressed CARD domains and full-length proteins in mammalian HEK293T cells. NOD1 CARD and NOD2 CARD could independently trigger NF-κB signals for immune responses (Figure3.2a). In comparison with other constructs, RIP2-CARD was less potent at activating NF-κB, probably due to its lack of kinase domain, which may further dimerize and presumably interacts with further downstream factors. To further examine the activation level of endogenous RIP2 *in vivo*, HEK293T cells were directly transfected with different concentrations of NOD1-CARD, NOD2-CARD, and RIP2-CARD (Figure 3.2c). Transfected HEK293T cells were lysed and separated the cellular fraction from nucleus complexes after 24 hours of transfection. Separated fractions were collected and loaded onto the native gel, which could separate protein samples according to their different oligomeric state. Western blotting experiment was conducted and anti-Phos-RIP2 antibodies were used to detect phosphorylated RIP2 in HEK293T cells. The results demonstrated that the increased phosphorylation and oligomerization level of RIP2 proteins were induced by an increased amount of NOD1/2 CARD and RIP2 CARD transfected into HEK293T cells (Figure 3.2c).

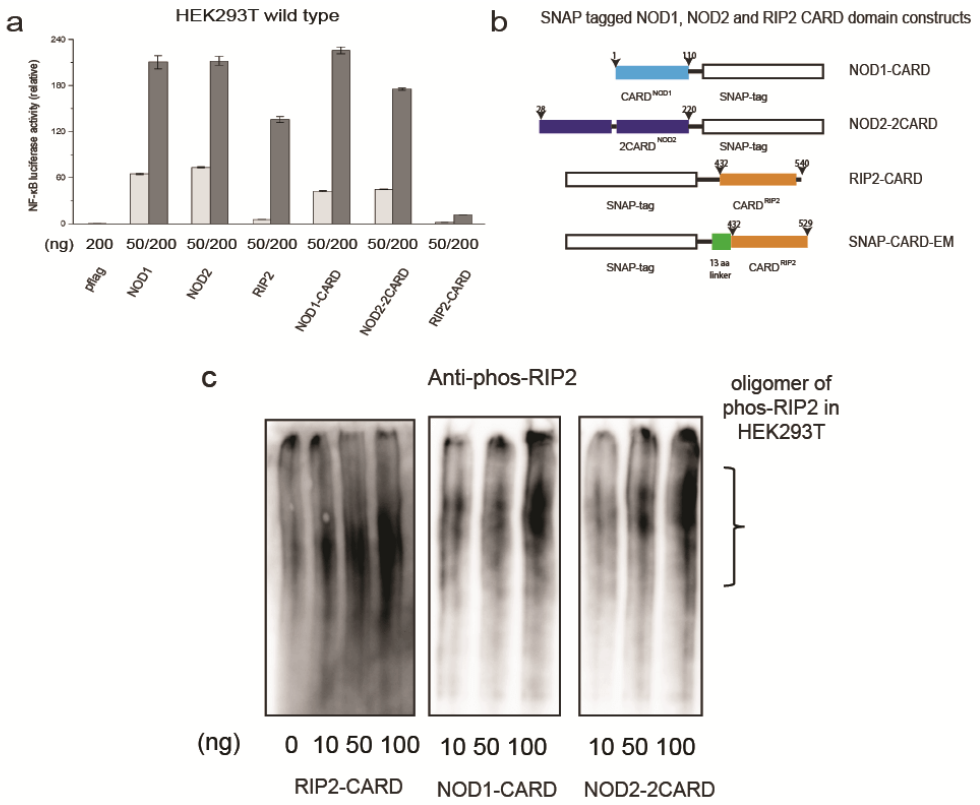

Figure 3.2. NF- κB promotor activation by NOD1, NOD2 and RIP2. (a) Full-length NOD1, NOD2, RIP2 and their corresponding CARD domain plasmids are used to transfected HEK293T cells to activate NF- κB promoter. (b) Schematic illustration of recombinant CARD domain constructs. SNAP tags were fused to the C-terminal of NOD1-CARD and NOD2-2CARD to replace the rest of the domains. SNAP tag was at the N-terminal of RIP2-CARD to better represent the domain architecture and replace the kinase domain. There is a 3C protease cleavage site in the linker between the CARD domains and SNAP. In SNAP-RIP2-CARD-EM construct, 13 amino acids 'VDEALREAQTKSA' were added in front of the CARD domain to stabilize the end, and C-terminal boundary of the RIP2-CARD was truncated to residue 529 to remove the flexible non-structured end. (c) Increased RIP2 phosphorylation and oligomerization level induced by a larger amount of CARD constructs. HEK293T cells were transfected with an increased amount of CARD domain constructs and the total amount of plasmids used for transfection of each sample was calibrated with empty vector. Cells were harvested 24 hr post-transfection and analyzed by anti-phospho-RIP2

western blot. Cellular fractions were loaded onto Bis-Tris native gel to separate molecular complexes based on size and charges. Increased level of oligomerized phosphorylated RIP2 was detected when HEK293T cells were transfected with more CARD proteins. Error bar represents standard deviation values of three independent repeats.

To further demonstrate the importance of RIP2 for propagating immune signals from NOD1 and NOD2, a gene-editing tool based on CRISPR-Cas9 technology was designed and engineered to knock out RIP2 genes from HEK293T cell by four sgRNAs (Figure 3.3a/c). Among these four sgRNAs, two of them (sgRNA1/2) successfully reduced the expression of RIP2 genes from HEK293T cells, confirmed by the results of western blot (Figure3.3b). Another two (sgRNA3/4) failed to block the NF-κB signals induced by NOD1-CARD. With the cellular experiments with RIP2 knockout HEK293T cell line, it demonstrated that neither full-length NOD1/2 or CARD domains of NOD1/2 were able to trigger the activation of NF-κB, confirmed by luciferase reporter assay. It exhibits that RIP2 is the dominant adaptor of NOD1 and NOD2 to propagate their immune signals.

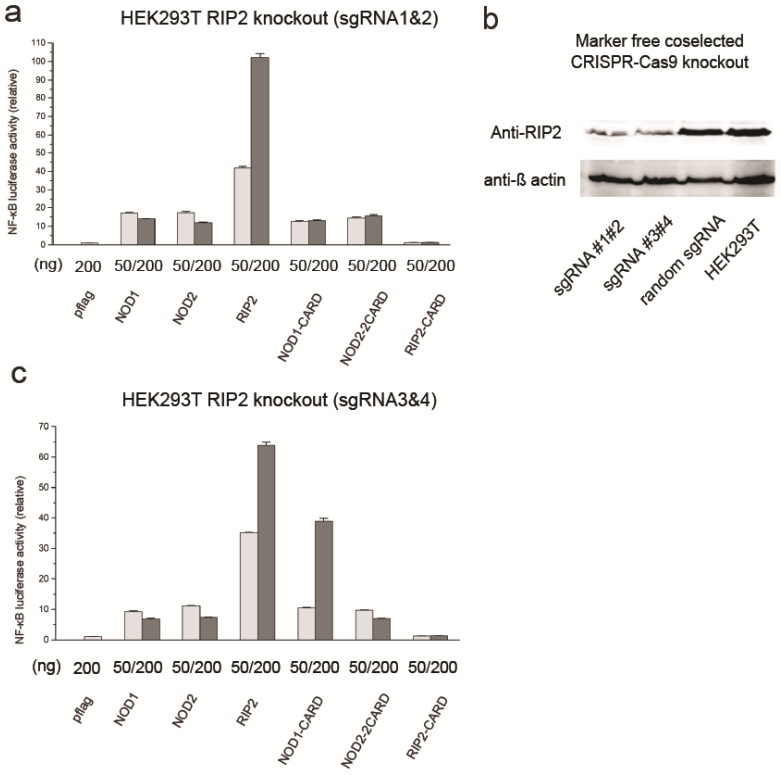

Figure 3.3. NF-κB promoter activation by NOD1, NOD2, RIP2 proteins, and their CARD domains in HEK293T RIP2 KO cell lines. (a) HEK293T RIP2 KO (sgRNA1&2) cells were transfected with empty pflag vector or NOD1, NOD2, RIP2, RIP2-CARD, NOD1–CARD, and NOD2–CARD together with pGL4.32 NF-κB-RE vector, and CMV-Renilla vectors. The amount of plasmids transfected was calibrated with pFlag plasmids to ensure that the same amount of plasmids were used in each transfection. Cells were harvested 24 h post-transfection and the level of NF-κB promoter activity was measured by dual luciferase assay according to the manufacturer's instructions. Error bar represents standard deviation values of three independent repeats. (b) Four sgRNAs were tested their ability to knock out endogenous RIP2, confirmed by western blotting. (c) HEK293T RIP2 KO (sgRNA3&4) cells were used to do the repeated experiment described in (a).

To validate the importance of RIP2-CARD for NF-κB signals, the residues of lysine 513 is substituted with Glutamic acid, located on the CARD domain of RIP2. This RIP2 mutant lost its function to induce the activity of NF-κB (Figure 3.4). In this way, K513E is a loss-of-function mutation for RIP2. To elucidate how RIP2 CARD domain dominates the function of RIP2 in innate immunity, RIP2 CARD domain was replaced with NLRC4 CARD for two reasons. One is that human NLRC4 is impotent to induce the activation of NF-κB signaling pathway in HEK293T cells. Another reason is that NLRC4 CARD has been reported to form filamentous oligomers as an active form (Diebolder, Halff et al. 2015). In this case, NLRC4 acts as an ideal negative control in the experiments of domain replacement. The fusion construct of the RIP2 kinase domain and NLRC4 CARD domain successfully obtained the ability of activation of NF-κB, confirmed by luciferase reporter assay (Figure3.4). This ability was significantly reduced when RIP2 kinase was fused with a loss-of-function mutant of NLRC4 CARD, loss of the ability to form NLRC4 CARD filaments (Figure3.4). These results illustrate that RIP2 is dependent on its CARD domain for signaling propagation and

RIP2 kinase domain alone is unable to trigger the activation of downstream signaling pathway.

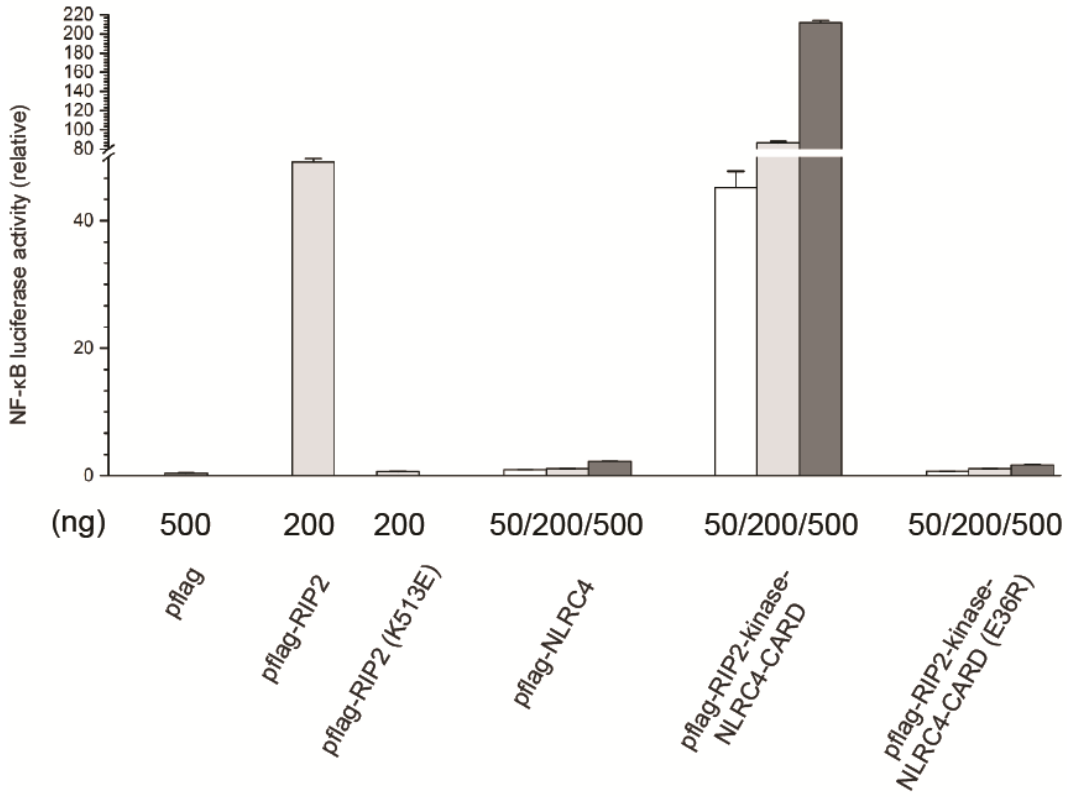

Figure 3.4. NF-κB promotor activation by domain swap chimeric constructs of RIP2. HEK293T cells were transfected with empty pflag vector, wild-type RIP2, and chimeric RIP2 together with pGL4.32 NF-κB-RE vector and CMV-Renilla vectors. Human NLRC4–CARD (1–100) was used to replace the RIP2–CARD domain (432–540) in human RIP2. Human NLRC4–CARD (E36R) is a monomeric mutant. Error bar represents standard deviation values of three independent repeats.

3.3 RIP2–CARD oligomerization activates downstream signaling

CARD domains play essential roles in the regulation of immune signals. To demonstrate the importance of RIP2 CARD in triggering NF-κB activity, crude sedimentation experiments were conducted for RIP2, which were examined by MAVS before (Wu, Peisley et al. 2014).

The mechanism of this experiment is based on the size of protein complexes. The active form of MAVS is an oligomer with a large molecular weight, which is packed in the pellet fraction after centrifugation with a low speed (Figure 3.5a). According to the convincible results of MAVS, I applied this experiment to RIP2, exhibiting a similar manner as MAVS. Starting with transfection of HEK293T cells with RIP2 plasmids, transfected cells were cultured for 24 hours and then harvested for cell lysis. Cell lysates were collected and spin down for five minutes at a speed of 10,000xg. The results showed that active RIP2 proteins were concentrated and packed in the pellet instead of in the soluble fraction. The construct of the RIP2 kinase domain fused with NLRC4 CARD was also examined in the same way, which showed that the majority of them were located in the pellet fraction (Figure3.5a). However, most of proteins were in the soluble fraction when RIP2 kinase domain was fused with a disruptive NLRC4 CARD domain (Figure 3.5a). These results were aligned well with the previous experiments about their ability to trigger NF-κB signals by luciferase assay (Figure3.2).

According to other studies, the indications for RIP2 activation in innate immunity depend on several activities, including the formation of oligomeric form of phosphorylated and ubiquitinated RIP2 kinase (Dorsch, Wang et al. 2006, Yang, Wang et al. 2013). To have a better understanding of the relation between oligomerization and phosphorylation of RIP2, HEK293T cells were transfected with NOD1, NOD2, and RIP2 CARD plasmids for analysis. According to the results of native gel western blotting for detection of phosphorylated RIP2, the increasing amount of oligomeric RIP2 was observed when HEK293T cells were transfected with more RIP2 plasmids. The oligomeric RIP2 complexes were phosphorylated and located in the top area of native gel due to their large size. The phosphorylated RIP2 oligomers demonstrated that RIP2 oligomerization was correlated with phosphorylation for signals propagation.

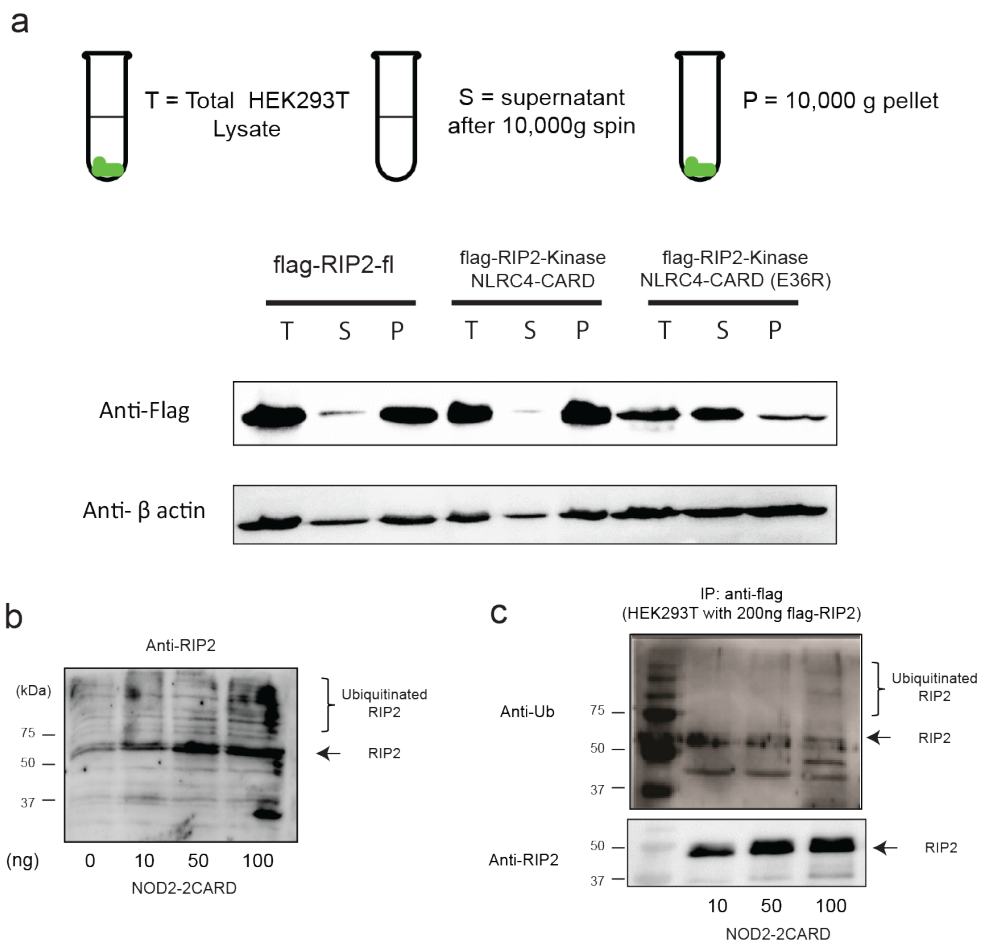

Figure 3.5. Active RIP2 was ubiquitinated to induce downstream signaling. (a) HEK293T cells were transfected with flag-tag wild-type RIP2 or chimeric RIP2 constructs. Total cellular extracts (T) were subjected to 10,000 × g precipitation for 5 min to isolate the supernatant fraction (S) and the pellet fraction (P). Western blots were representative of three independent experiments. (b)Increased number of higher molecular bands were induced by an increased amount of NOD2-2CARD-SNAP. HEK293T cells were transfected with an increased amount of NOD2-2CARD-SNAP constructs and the total amount of plasmids used for transfection for each sample was calibrated with empty vector. Cells were harvested 24 hr post-transfection and levels of endogenous RIP2 in each sample were measured by anti-RIP2 antibody. Western blots were representative of 3 independent experiments. (c) I Increased ubiquitinated RIP2 level was induced by an increased amount of NOD2-2CARD-SNAP. HEK293T cells were transfected with an increased amount of NOD2-

2CARD-SNAP constructs and the same amount of Flag-RIP2 constructs and the total amount of plasmids used for transfection for each sample was calibrated with empty vector. Cells were harvested 24 hr post-transfection and RIP2 was harvest by anti-Flag immunoprecipitation. Levels of RIP2 ubiquitination and RIP2 in each sample were measured by anti-ubiquitin and anti-RIP2 antibody. Western blots were representative of 3 independent experiments.

To demonstrate of RIP2 ubiquitination, different amount of NOD2 CARD plasmids were used to transfect HEK293 cells for 24 hours. Harvested cells were analysed with western blot. With an increased amount of NOD2 CARD plasmids, more and more oligomeric RIP2 were detected by anti-RIP2 antibodies, and the ubiquitination signal of RIP2 was enhanced (Figure3.5b). An immunoprecipitation experiment was conducted to examine the ubiquitination of RIP2, which was detected by anti-ubiquitin antibodies (Figure 3.5c). The amount of ubiquitin was aligned with the amount of RIP2. The results of both western blot experiments indicate that RIP2 oligomerization is probably a prerequisite for the phosphorylation and ubiquitination of RIP2 to trigger immune signals.

3.4 Oligomerized RIP2 forms a filamentous structure

The importance of RIP2 in immune responses for invading bacteria is addressed in many studies. It is necessary to investigate the structure of oligomeric RIP2 complexes in *vivo*. HEK293T cells were transfected with amino-terminal flag inserted RIP2 plasmids for 24 hours. HEK293T cells were harvested and lysis with RIPA buffer, which was gently centrifuged at a low speed to get rid of cell debris and nucleus. The supernatant was collected and mixed with anti-flag M2 agarose beads for extraction and purification of RIP2 complexes, which was then concentrated and observed under the field of negative stain EM (Figure 3.6, left panel). The results illustrated that full-length RIP2 was able to form a

filamentous structure to perform its function in innate immunity. These filaments formed by RIP2 full length were wide about 12nm and adopted a helical symmetry. To further ensure that these filaments were formed by RIP2 proteins, an MBP tag was engineered to insert at the N-terminus of RIP2. The MBP-tagged RIP2 construct was expressed and purified to demonstrate that filaments were still observed with a thicker width at a diameter of 16nm (Figure 3.6, right panel), which was aligned well with the expected diameter. The size of MBP-tagged RIP2 filaments was larger than that of RIP2 full-length alone.

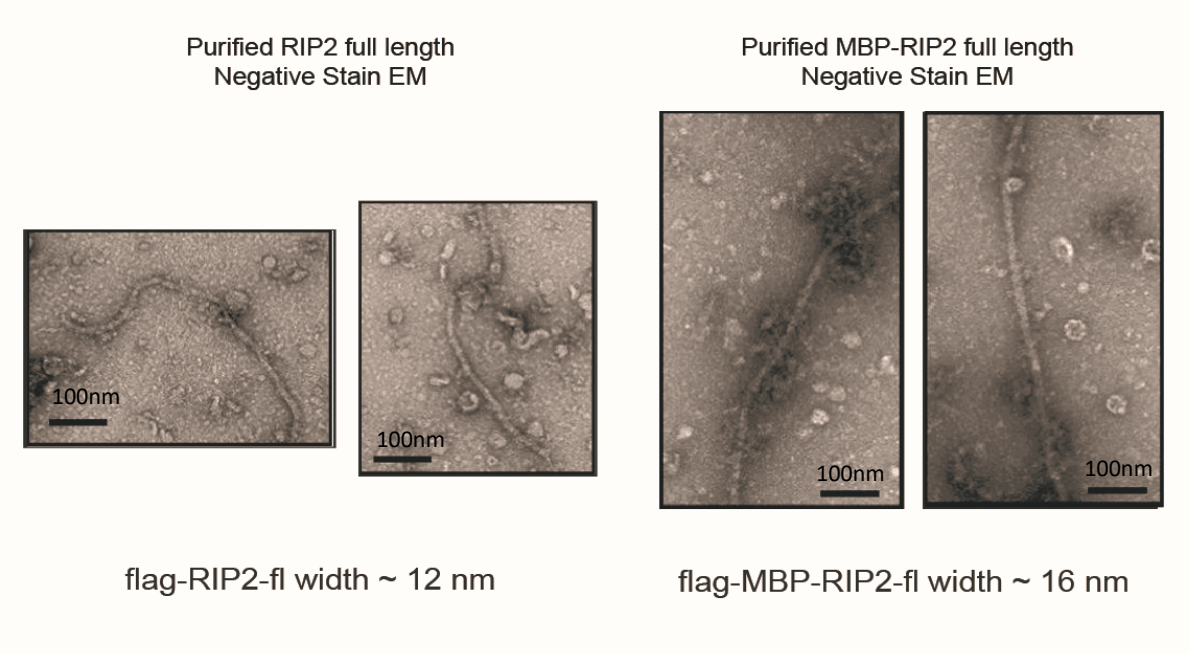

Figure 3.6. Active RIP2 forms filamentous structure in vivo. Negative stain EM images of flag-RIP2 and flag-MBP–RIP2 purified from HEK293T transfected cellular extracts. Flag-RIP2 filaments are about 12-nm thick. The diameter of flag-MBP–RIP2-fl filaments is wider at 16 nm. Scale bar: 100 nm.

Besides, when HEK293T cells were transfected with RIP2 kinase domain plasmids or the plasmids of the RIP2 kinase domain fused with NLRC4 monomeric CARD mutation, no filamentous object was shown under the field of EM after transfected cells were purified and prepared in the same way. These observations of different constructs were aligned with their performances in the crude sediment experiments, respectively. Only containing functional

CARD domains of these constructs, filamentous structures were observed and located in the pellet after centrifugation. The full-length RIP2 and MBP-RIP2 filaments extracted from transfected HEK293T cells provided with the basic information about the size and morphology of RIP2 filaments under EM. Due to low density and poor homogeneity of the protein sample, it was restricted to solve the high-resolution structure of RIP2 full-length filamentous structure expressed by HEK239T cell with the powerful tool of electron microscopy. The data obtained from negatively staining EM only determined the limited structural parameters, such as the distance between two protruding points. The high-resolution structure could provide more information about the protein sample.

To obtain more detailed structural information of active RIP2-CARD filaments, a reconstitution assay was developed to recapitulate the RIP2 activation process *in vitro*. According to the architecture of RIP2 full length, the new construct was engineered with an N-terminal SNAP protein to improve the protein stability in the process of chemical refolding, following with a C-terminal RIP2 CARD domain for structural study. To generate sufficient and pure RIP2 CARD filaments, the chemical refolding was adopted to reconstitute active and pure RIP2 CARD monomers with a resting state, which were quickly recruited and extended by RIP2 CARD seeds after incubation together (Figure 3.7a).

These recombinant SNAP-RIP2-CARD seeds (pre-activated oligomer) and monomers (resting state) were prepared using a slightly modified protocol from previous MAVS studies (Dorsch, Wang et al. 2006, Peisley, Wu et al. 2014, Wu, Huoh et al. 2016). Different from the protocol of MAVS monomer preparation, the concentration of guanidine was decreased to 7M, which was enough to reduce the precipitation and misfolding of RIP2 CARD in the reconstitution system (Figure 3.7a). Without the presence of stimuli, monomeric RIP2 CARD was able to maintain its state for more than one week at 4ºC. When they were incubated with RIP2 CARD seeds, monomeric RIP2 CARD proteins were recruited and extended the pre-

oligomeric RIP2 CARD seeds to form long filaments with various lengths in the dependence of the different molar ratio of monomers and seeds (Figure 3.7b. middle panel). The reconstitution system was operated iteratively to generate straight and homogeneous filamentous complexes until most monomers participated in the formation of long filaments (Figure 3.7b, middle panel).

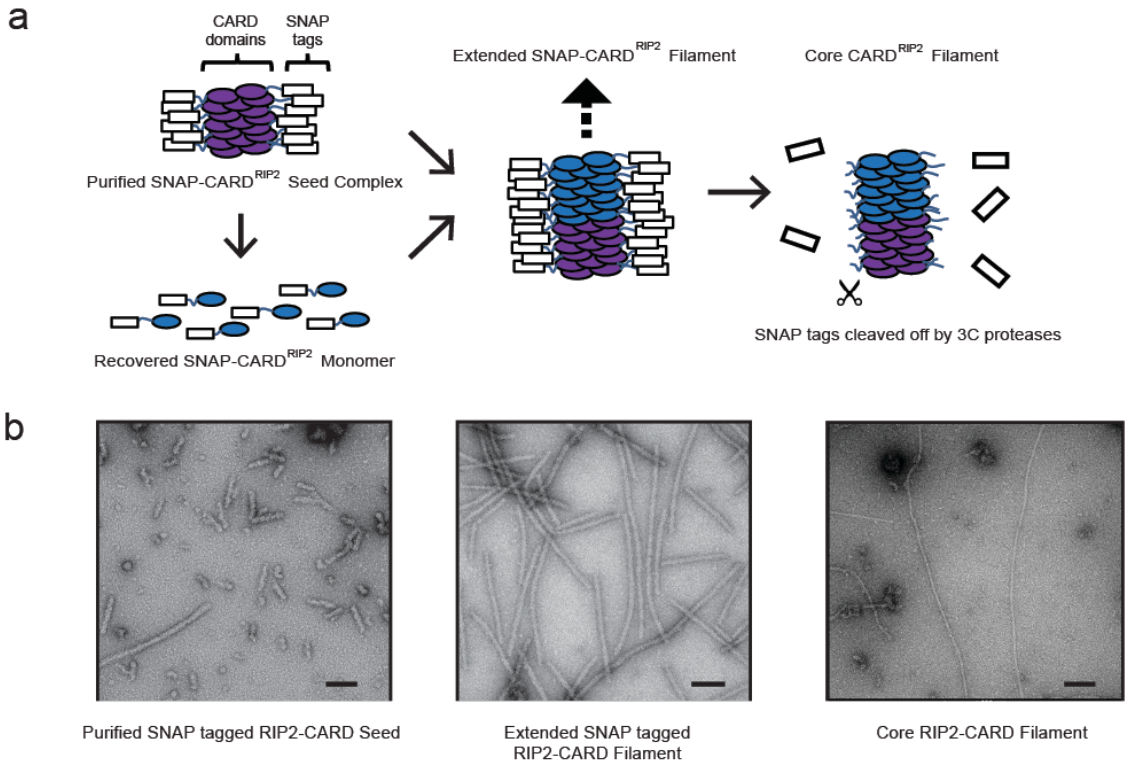

Figure 3.7. Preparation of recombinant RIP2–CARD filament in its signaling active form. (a) Cartoon illustrations showing how recombinant RIP2–CARD filaments were prepared. The oligomeric seed fraction of SNAP–RIP2–CARD was purified and refolded into functional monomers at resting state. Extended filaments were prepared by co-incubating monomers and seeds together. Once extended filaments formed, 3C proteases were used to remove the peripheral SNAP fusion tags. The ordered core RIP2–CARD filaments were revealed afterward. (b) Negative stain EM images of SNAP–RIP2–CARD seeds (left panel), extended SNAP–RIP2–CARD filaments (middle panel), and the core RIP2–CARD filaments (right panel) at 49,000× magnification. The core RIP2–CARD filaments were much thinner (~7 nm) compared to SNAP–RIP2–CARD filaments (~11 nm).

To expose the RIP2 CARD filamentous core for high-resolution structure, SNAP protein located at the periphery of filamentous core was digested and removed (Figure 3.7, right panel). From the results of circular dichroism spectrum analysis, the spectrum showed that the most apparent spectral signatures for α-helix were negative bands at 222 nm and 208 nm. Both the RIP2-CARD seeds and monomers shared similar curves and contained mostly α-helix. (Figure 3.8a).

Wild-type SNAP-RIP2-CARD seeds readily recruited refolded SNAP-RIP2-CARD monomers to their ends and formed long filaments. This growth of filaments was also observed with native gel EMSA (Figure 3.8b).

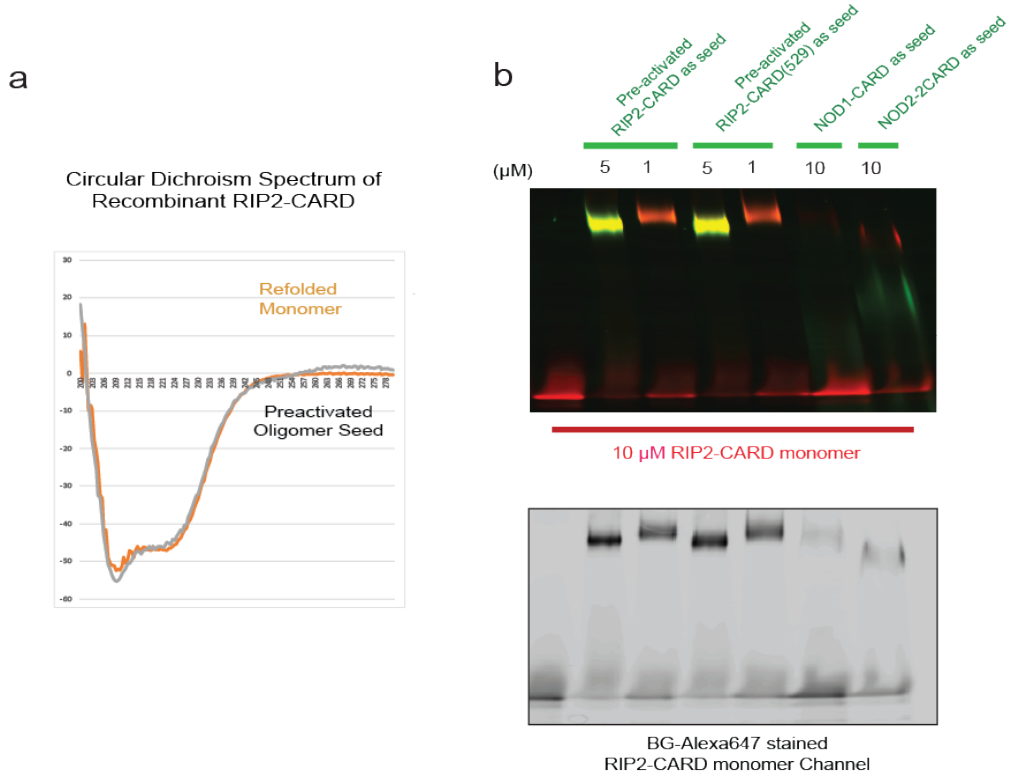

Figure 3.8. Capture of the interaction between monomeric RIP2-CARD and NOD1-CARD, RIP2-CARD and NOD-CARD. (a) Refolded monomer (yellow) and oligomer seed (black) were examined by Circular Dichroism spectrum. They shared similar curves and contained mostly α-helices. (b) Dual-colour stained Bis-Tris native gel demonstrating how different

seeds, including SNAP–RIP2–CARD (1 or 5 μM), SNAP–NOD1–CARD (10 μM), and SNAP–NOD2–CARD (10 μM), coloured in green, triggered the induced oligomerization process of SNAP–RIP2–CARD (10 μM) monomers, coloured in red. Monomer channel was shown in the lower panel in black and white.

These different lengths of filaments were examined by native gel, which could separate them by their different sizes and observed directly by negatively staining EM (Figure 3.8b). For the monomer channel of EMSA, monomers alone were the smallest molecules that had the highest migration speed compared to other mixed protein samples. With a different ratio of monomers and seeds, these filaments had varied sizes with different migration speeds in the native gel. Similar to RIP2 CARD seeds, recombinant NOD1 CARD and NOD2 CARD were able to induce the formation of RIP2 CARD filament without any other factors, examined by their performances in native gel and observations under EM. These results illustrated their ability to propagate immune signals. It was also observed from native gel image that RIP2 CARD filaments induced by NOD1 CARD or NOD2 CARD did not migrate with them together and shifted in a faster migration speed, which was different from that of RIP2 CARD (Figure 3.8b). It was probably that the interaction of NOD1/2 CARD with RIP2 CARD existed but transient in this situation.

The RIP2 CARD filaments induced by NOD1 CARD and NOD2 CARD were unstable compared with the ones by RIP2 CARD seeds, leading to their shorter length and heterogeneity examined by negatively stained EM (Figure 3.9a). In conclusion, this assay produced active RIP2 CARD monomers, which were able to form filaments by the stimulation of recombinant NOD1/2 CARD and RIP2 CARD seeds independently.

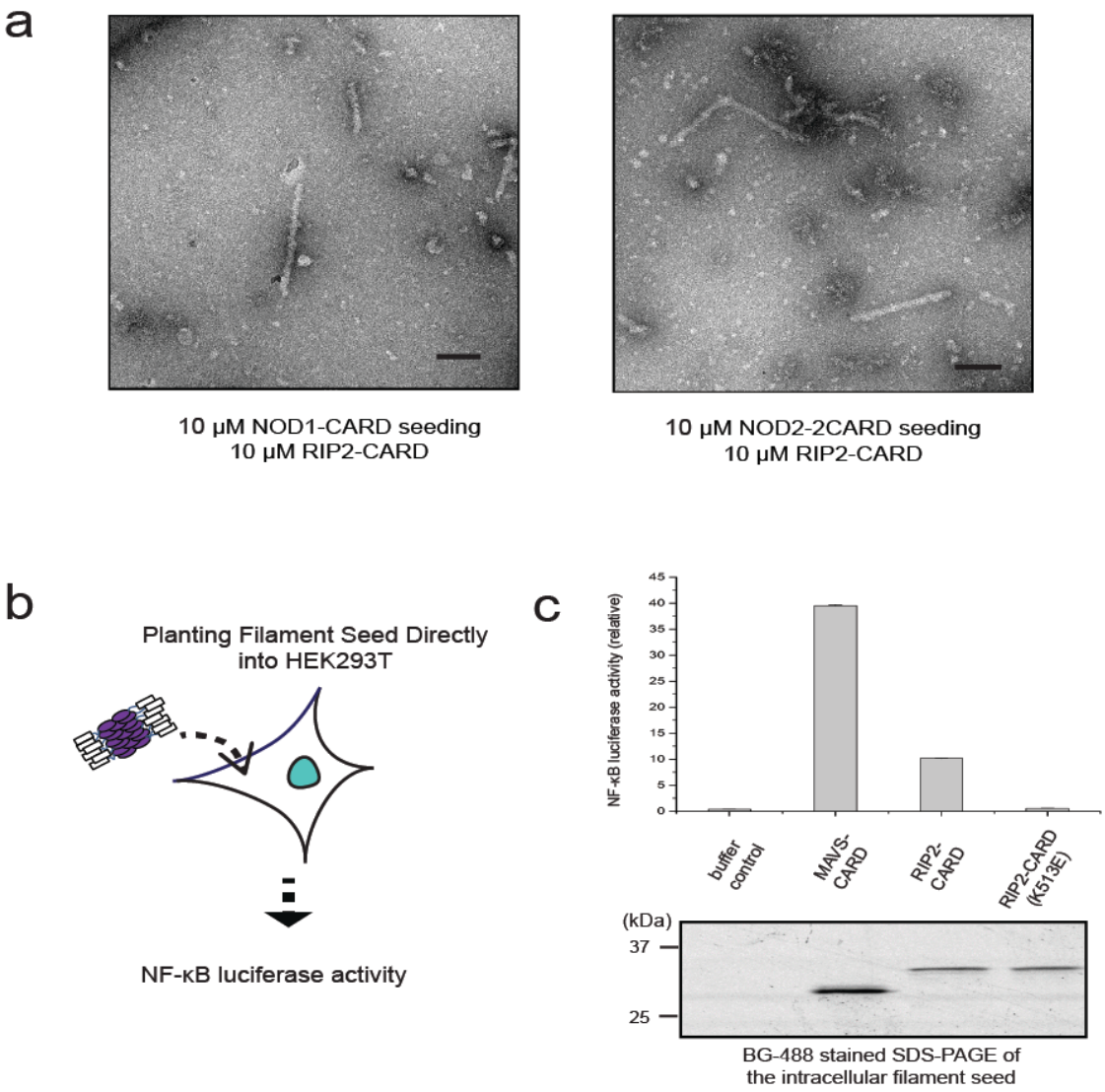

Figure 3.9. NF-κB can be activated by intracellular recombinant RIP2–CARD seeds. (a) Negative stain EM images showed that 10 μM RIP2–CARD proteins were induced to form filaments by 10 μM NOD1–CARD or 10 μM NOD2–CARD. Scale bar: 100 nm. (b) Cartoon illustration of NF-κB promoter luciferase assay with SNAP–RIP2–CARD protein seed directly electroporated into the cells. (c) SNAP–RIP2–CARD seeds, SNAP–RIP2–CARD (K513E) seeds, and MAVS–CARD–SNAP were electroporated into HEK293T cells, together with pGL4.32 NF-κB-RE vector and CMV-Renilla vectors. The same amount of proteins was transfected in each sample. BG-Alexa 488 dye stained SDS-PAGE conferring that the similar

level of recombinant seeds was catapulted into the reporter cells. Error bar represents standard deviation values of three independent repeats.

To examine whether the reconstituted RIP2 CARD filaments were the representative state of endogenous RIP2 in active form, these filaments were electroporated into mammalian HEK293T cells for (Figure 3.9b), which demonstrated that oligomeric RIP2 CARD proteins successfully induced the activation of NF-κB signals *in vivo* by luciferase reporter assay (Figure 3.9c). In this experiment, purified MAVS CARD protein sample from *E.coli* acted as a positive control to demonstrate that the ability of RIP2 CARD filaments was sufficient to activate NF-κB pathway, while the disruptive mutants of RIP2 CARD (K513E) were impotent to form filamentous structure and activate immune signals (Figure 3.9c). In conclusion, the reconstituted RIP2 CARD filaments are capable of triggering the intrinsic signals in HEK293T cells for immune responses.

3.5 Structural Studies of RIP2-CARD Filament

The homogeneity of the in vitro-reconstituted RIP2-CARD filaments allowed the structure determination of this filament. Long and straight core RIP2-CARD filaments were generated by optimization of the CARD domain boundaries. A 13 amino acid tag was added to the N-terminal of residue 432 of RIP2-CARD and the last 11 amino acids at the C-terminal end of RIP2-CARD were removed to stabilize the core RIP2-CARD filament and prevent filament bundling on the EM grid. This construct is called RIP2-CARD-EM. After removal of the Snap fusion tag, the core RIP2-CARD-EM filaments were further purified by size-exclusion chromatography and then vitrified onto EM grids and images by Titan Krios (Figure 3.10a). To analyse the data, Relion 2.0 software was used to do helical reconstruction for RIP2 CARD filaments. In Relion 2.0, filamentous objects were picked manually and segmented to obtain more than 600,000 particles for 2D classification. Several 2D classes emerged

consisting of obvious features and good density after several rounds of 2D classification (Figure 3.10b). The particles classified in the good 2D classes were selected and combined for 3D helical reconstruction and further for 3D refinement.

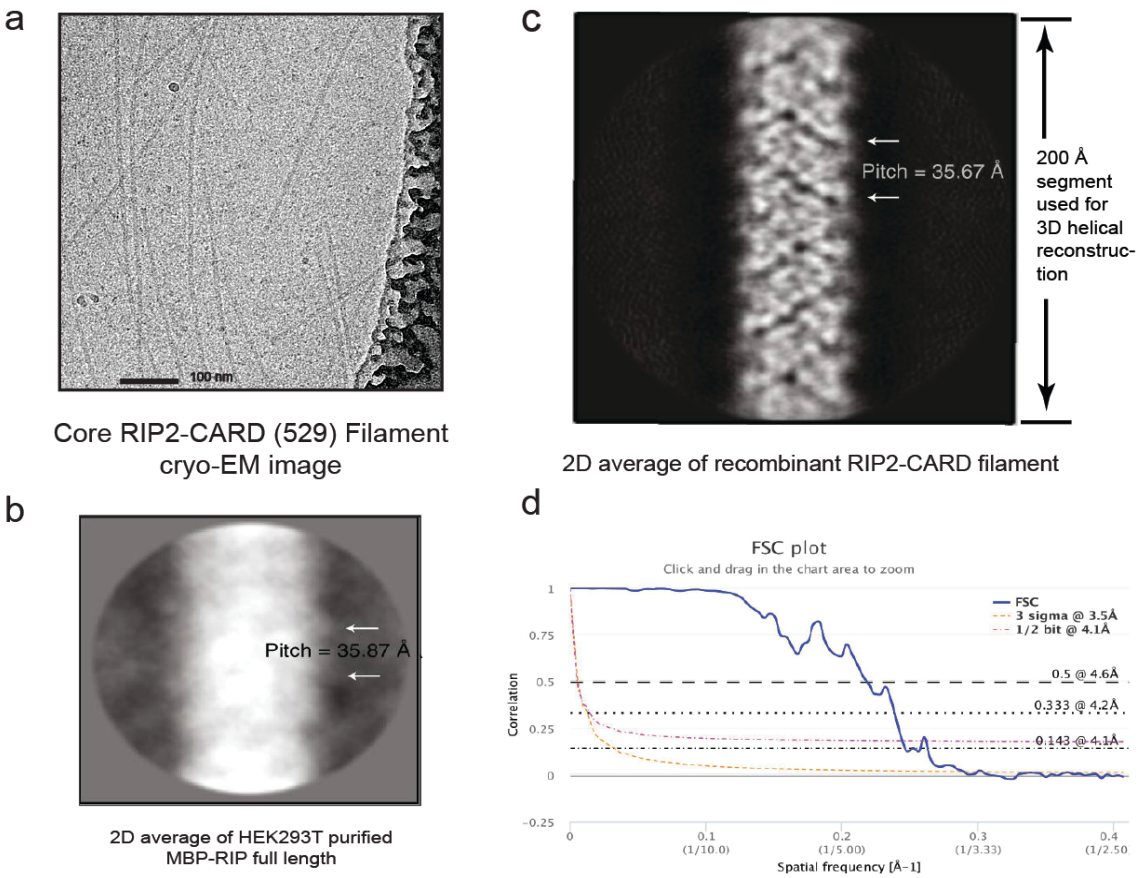

Figure 3.10. Electron density of RIP2–CARD filament resolved using helical reconstruction. (a) Cryo-EM micrograph of core RIP2–CARD–EM construct. Scale bar: 100 nm. (b) 2D class image of the core RIP2–CARD–EM generated when picking 140,000 segments. (c) Representative 2D class average of MBP–RIP2 extracted from HEK293T cells. About 500 segments were used to generate this preliminary 2D average class. By manual counting of the pixels between the two protrusions along the filament. Visual helical pitch was found to be about 35.87 Å. (d) The FSC plot showed that the resolution for the overall density of the entire segment is 4.1 Å, at FSC = 0.143 gold standard.

Previous data of MBP-RIP2 filaments produced by the expression of HEK293T cells was analyzed to form images of the 2D class, which was poor quality (Figure 3.10c). It is worth and reliable to analyze the limited parameters among different filamentous structures participated by RIP2 CARD such as the pitch size to demonstrate that the reconstituted RIP2 CARD filaments were identical with the parameters of *in vivo* RIP2 full-length construct. For MBP-RIP2 filaments imaged by negatively stained EM, the 2D averaged class gave a distance of about 17 pixels, with 2.11 Å per pixel, which was about 35.87 Å (Figure 3.10b). For RIP2-CARD-EM imaged by cryo-EM, the parameter is 29 pixels with 1.23 Å per pixel, which is 35.67 Å. For the final density map of the RIP2 CARD filamentous structure, the two protruding points have a distance of about (720/101.36)*4.96 = 35.23 Å. These three numbers, including 35.87 Å, 35.67 Å and 35.23 Å are very close, suggesting that the RIP2 CARD-EM filaments generated *in vitro* have successfully reflected the native state of MBP-RIP2 full-length filaments expressed by mammalian cell. To obtain the helical parameters of RIP2 CARD filament, helical rise and rotation were narrowed down to a restricted range by analyzing the map of power spectrum according to the instructions from Relion2.0 manual book (Scheres 2012) and previous similar structural work (Wu, Peisley et al. 2014, He and Scheres 2017). With the help from SPRING40 software, the parameters were further restricted with a range of 4.9–5.1 Å for the helical rise and about -101º for the helical twist. To obtain a better resolution, 3D refinement and other post-processing of the segment density were performed by Relion2.0, suggesting that RIP2 CARD filament adapts the helical symmetry of single left-handed helicity (Figure 3.10d).

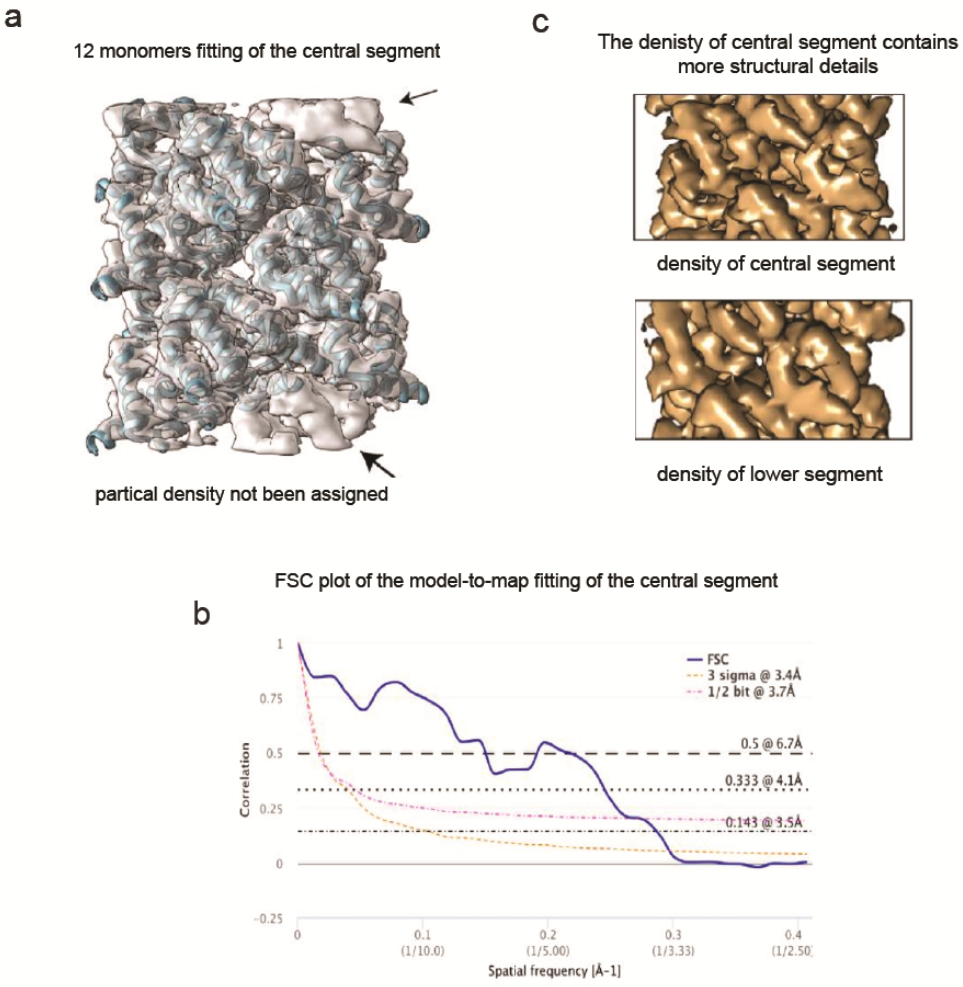

Figure 3.11. The central density of RIP2 CARD filament. (a) The final RIP2-CARD 12mer model (PDB: 5YRN) fit to the central segment of the cryo-EM density. There are chunks of density not assigned to any amino acids during pseudo-crystallographic refinement. (b) Map-to-model FSC plot of the central segment. FSC=0.143 when the resolution cut-off was 3.5 Å. (c) Schematic view of the central segment density as well as another section slightly away from the centre. RELION refined filament density has non-uniform density features along the z-axis.

To have a better demonstration for the formation of RIP2 CARD filament, the density in the central segment was cropped out to represent and assign with twelve monomers of RIP2 CARD by Chimera, which was conducted with pseudo-crystallographic refinement by the real-space refinement of Phenix. The final density model illustrates with detailed structural

information at a high resolution of 3.6 Å, with a helical rise of 4.936 Å and a helical rotation at −101.4° (Figure 3.11a,b,c) (Table 2).

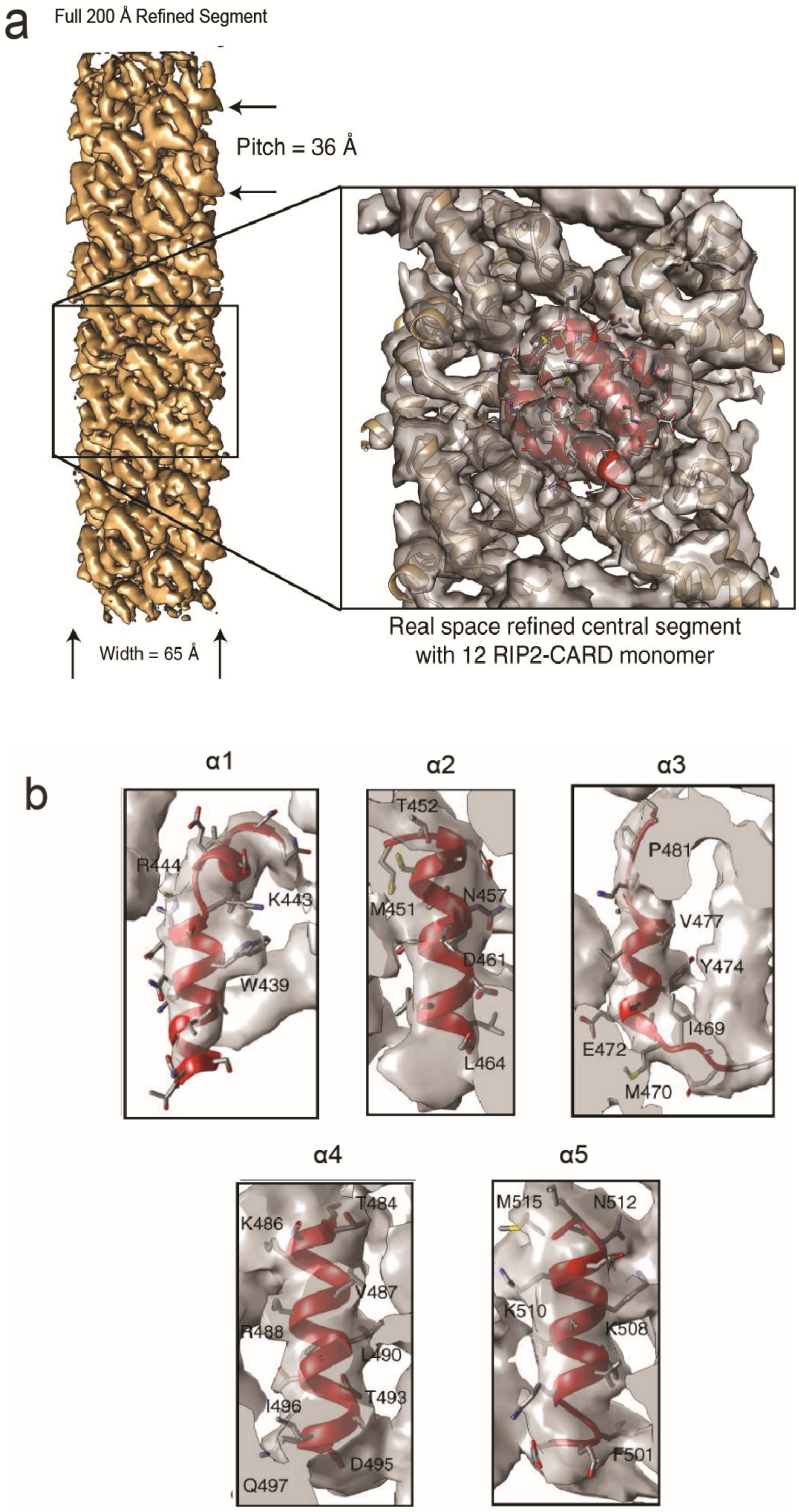

Figure 3.12. A RIP2-CARD 12mer structure based on cryo-EM density. (a) Cartoon illustration of the average segment density of activated RIP2–CARD filamentous structure

(EMDB code: 6482). The image was prepared using Chimera with auto-adjusted contour level. Twelve monomers of RIP2–CARD was fitted into the central segment according to the protocol. (b) Close view of the electron density. Five different α-helices from RIP2–CARD fitted nicely into the density map, with the aromatic side chains at important references for determining the registry.

According to the final density map, it was shown that RIP2 CARD filament was a left-handed helical symmetry object (Figure 3.12a). Similar to other filamentous structures of death domain family, the formation of RIP2 CARD filament was supported by three different types of interfaces including Ia/Ib, IIa/IIb and IIIa/IIc interfaces (Ferrao and Wu 2012). For the central density of RIP2 CARD filament, 12 monomeric models of RIP2 CARD were fitted to analyse the detailed features of RIP2 CARD filamentous density further. In this model, all the five α-helices of RIP2 CARD were able to fit into the density map with the bulky side chains of their amino acids well assigned (Figure 3.12b).

To have a better understanding of the RIP2 CARD monomeric structure solved by cryo-EM, the structure was superposed with a monomer structure solved by NMR(PDB: 2N7Z) (Lin, Tann et al. 2015), showing a small difference on the overall domain architecture (Figure 3.13a, b). This observation was also found in other death domain family members, suggesting that a gentle conformation change happened from monomeric form to oligomeric form (Zhang, Chen et al. 2015). To identify the interactions among these interfaces of RIP2 CARD filament, it was necessary to obtain reasonable conformations of side-chain by real space refinement (Figure 3.13c, d).

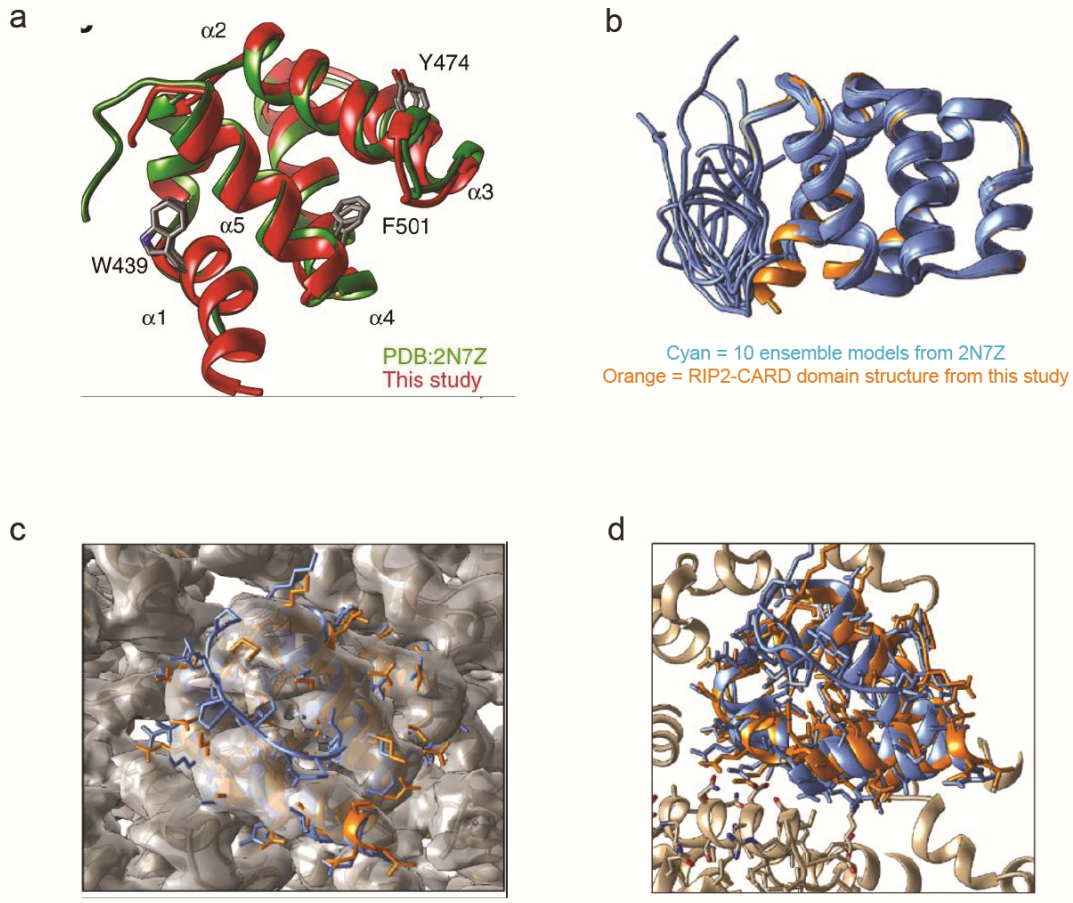

Figure 3.13. Superposition of RIP2-CARD from 2N7Z and 5YRN. (a) Comparison of RIP2–CARD monomer models from PDB (green) and this study (red). (b) Overlapped view of 10 conformational states from 2N7Z with the J chain of 5YRN as the reference. (c) Monomer structure from 2N7Z is not suitable for direct interpretation of the cryo-EM density, due to disordered amino acids towards the ends. (d) Side chains from 2N7Z monomers are not compatible with interdomain interfaces. Local refinement based on cryo-EM density is necessary to build the RIP2-CARD oligomer model.

After a comparison of different known oligomers of the CARD domain, including pro-caspase-1, MAVS and RIP2, it is observed that their helical parameters were almost the same with a helical rotation of around −101° and a helical rise of about 5 Å (Figure 3.14). This

observation could be a coincidence with all adapting a geometry favoured by the globular CARD domain, or this observation might hint that potential structure crosstalk was possible among these innate immune players. Further investigations are needed to test this hypothesis.

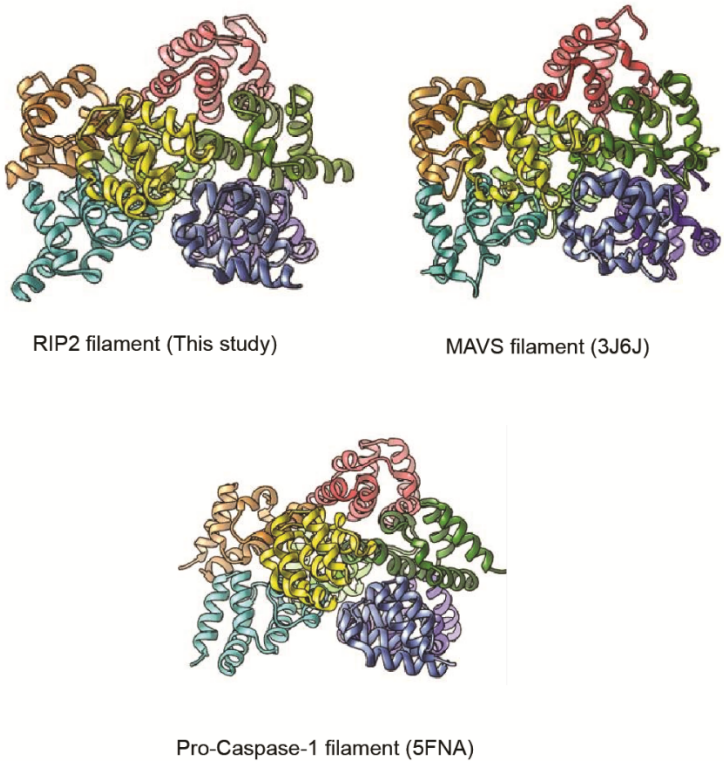

Figure 3.14. Different filamentous structures composed of CARD-containing proteins including RIP2, MAVS, and pro-caspase-1. It was quite apparent to notice their shared helical symmetry.

In the RIP2 CARD filamentous structure, Type I interaction (orange and red) and Type II interaction (orange and blue) made the most contribution to the formation of interdomain binding (Figure 3.15a). Several pairs of residues located in the interfaces of these two interaction types were identified and examined their importance to trigger NF-κB signals by luciferase reporter assay (Figure 3.15a). It is reasonable for one residue to interact with several residues located on the other interface due to the flexibility of the surface area.

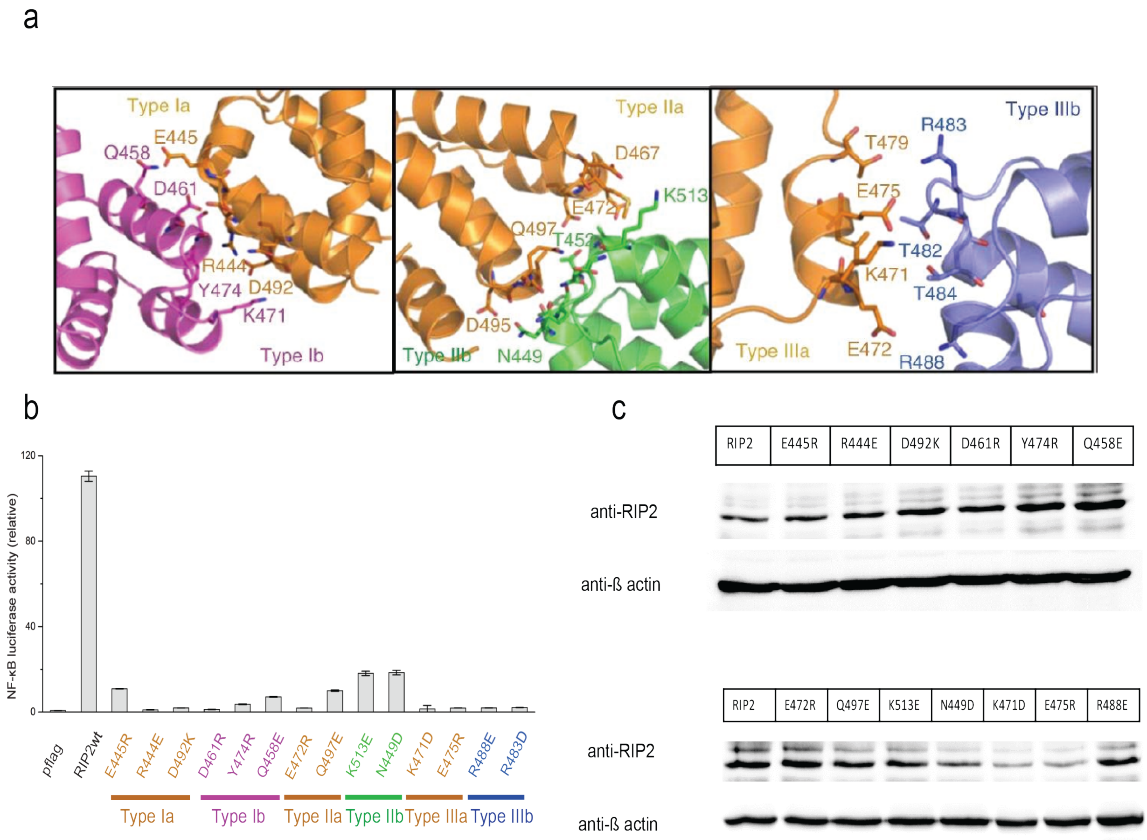

Figure 3.15. Interdomain surface interactions within the RIP2–CARD filament. (a)Cartoons illustrated the details of Ia:Ib, IIa:IIb, and IIIa:IIIb interactions in RIP2-CARD filament. Residues at the interface are shown in stick models. (b) NF-κB promoter activation by RIP2 and RIP2 single-point mutants. These RIP2 point mutations localized on the interaction interfaces and showed loss of function in terms of NF-κB promoter activation. (c) Expression levels of all RIP2 mutants are similar. HEK293T cells were transfected with wild-type RIP2 and RIP2 mutants. Cells were harvested 24 h post transfection. Levels of over-expressed wild-type RIP2 and RIP2 mutants were measured by anti-RIP2 antibody. Western blots were representative of three independent experiments.

In the structure of RIP2 CARD filament, it requires much work to identify all the interaction pairs individually. Critical residues were analysed and determined to stabilize the oligomeric RIP2 CARD. In the interaction of Type I, Type Ia interface consists of residues from helix1 and 4 including R444, E445 and D492 coloured in orange, interacting with Type Ib interface

by charge side chains from helix 2 and 3 including residues of 1458, D461, Y747 and K471 in red colour (Figure 3.15a/b). These residues were reported in the previous studies to demonstrate that they play essential roles in the formation of RIP2 CARD oligomers (Fridh and Rittinger 2012, Mayle, Boyle et al. 2014, Maharana, Pradhan et al. 2017). Also, it was proposed that residues of R444, D461, and D492 in Type I interfaces were required for the CARD-CARD interactions of RIP2 with NOD1 and RIP2 itself (Figure 3.15a/b) (Mayle, Boyle et al. 2014). It was reported that Y474F mutation abolished the function of RIP2, which can be explained by the important role of Y474 in the mediation of Type I interaction with the help of RIP2 CARD filamentous structure (Tigno-Aranjuez, Asara et al. 2010). For Type II interaction, IIa interface (coloured in orange), includes the residues at the turns between helix2/3 and helix4/5 such as D467, E472, D495 and Q497. The residues within the turn between helix 1/2 are located on the IIb interface (coloured in green), including N449, K513 and T452. Type III (orange and blue) interface was relatively weak, and it was stabilized by interactions between residues from helix 2 (orange, Type IIIa, T479, E475, K471, and E472) and coiled turn between helix 3/4 (blue, Type IIIb, R483, T482, T484, and R488). Most of these residues located on the interaction surfaces are important to maintain the immune signals from RIP2 and have been reported to abolish RIP2 signals including E472, E475, R483 and R488 (Fridh and Rittinger 2012, Maharana, Pradhan et al. 2017).

Overall, all the residues located in different interfaces of RIP2 CARD contributed to stabilizing the formation of RIP2 CARD filament by their gathered interactions. It is difficult to predict the interactions of the oligomeric state of CARD domains due to their globular shape and relative locations of their surfaces in different rotation angles by a computational method. With the cryo-EM structure of RIP2 CARD filament, it is facilitated to have a better understanding of signaling complexes in innate immune responses. To validate the filamentous structure of RIP2 in cellular signals, point mutations were engineered in RIP2

full-length constructs and were conducted on the critical residues located on all six interfaces of RIP2, which were analysed by NF-κB luciferase reporter assay. The results were well aligned that the disruptive mutations of RIP2 CARD for interface interactions were impotent to activate cellular signals (Figure 3.15b/c).

Charge-reversal mutations of RIP2 were delicately designed to validate the filamentous model and identify interaction pairs in different interfaces. There were two typical examples of interaction pairs N449/D495 and E445/Q458, which play important roles in cellular activities. The single mutation of any of these four residues caused the abolishment of NF-κB signals (Figure 3.16a-c).

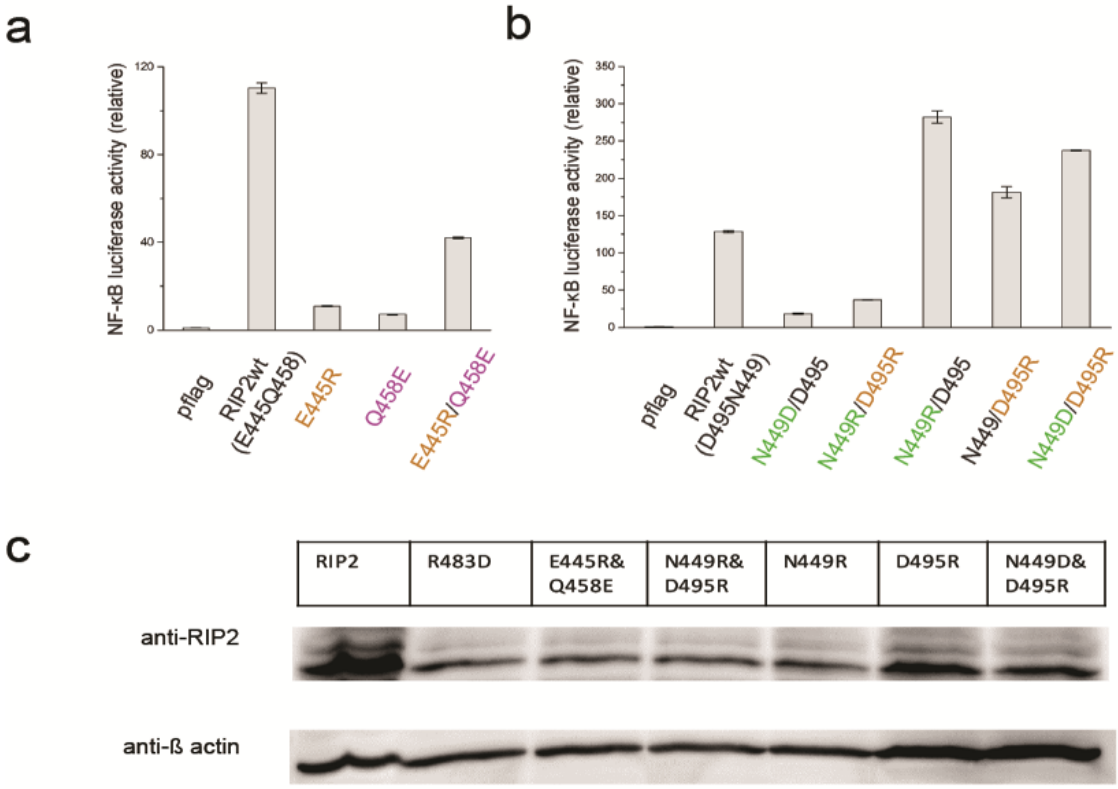

Figure 3.16. Interdomain surface interactions within the RIP2–CARD filament. (a) NF-κB promoter activation by RIP2, RIP2 single-point mutants E445R, R458E, and RIP2 double mutant E445R andR458E. The single mutants all showed loss of ability to activate NF-κB promoter, while the E445R and R458E double mutant partially restored NF-κB promoter activation. Error bar represents standard deviation values of three independent repeats. (b)

NF-κB promoter activation by RIP2 and RIP2 mutants in HEK293T cells. RIP2 single-point mutants N449D and RIP2 double mutant N449R andD495R showed loss of function. While RIP2 single-point mutants N449R, D495R, and double mutant N449D and D495R showed higher NF-κB luciferase activities. Error bar represents standard deviation values of three independent repeats. (c) Similar experiments as described in Figure b.

The signals of cellular activity were six times higher than the single mutations when reverse-charge mutations were introduced as E445R/Q458E, which obtained their signals again. However, the signals were still inactive when repulsive residue pairs were introduced to the position of N449/D495 such as Asp/Asp or Arg-Arg. With the introduction of stronger charged pairs, such as N449/D495 or N449/D495R, RIP2 mutants were more active than wild-type RIP2 in triggering NF-κB signals, demonstrating that the oligomeric tendency of RIP2 regulates its intensity in innate immunity. In conclusion, the results of luciferase reporter assay supported the RIP2 CARD filamentous model and provided insights into the plasticity of CARD surface interactions. The flexible pairing of surface residues serves as the key to the molecular imprinting message, as long as the topology of template lock matches. Additionally, these mutations were engineered and expressed in HEK293T cells with an N-terminal GFP tag for luminance under a confocal microscope. Puncta-like objects were observed when HEK293T cells were transfected with wild-type RIP2 plasmids as well as the two reversal-charged mutations, while the single mutations of E445R and Q458E did not form puncta (Figure 3.17). Together with previous data, the RIP2 CARD filamentous model was validated and supported.

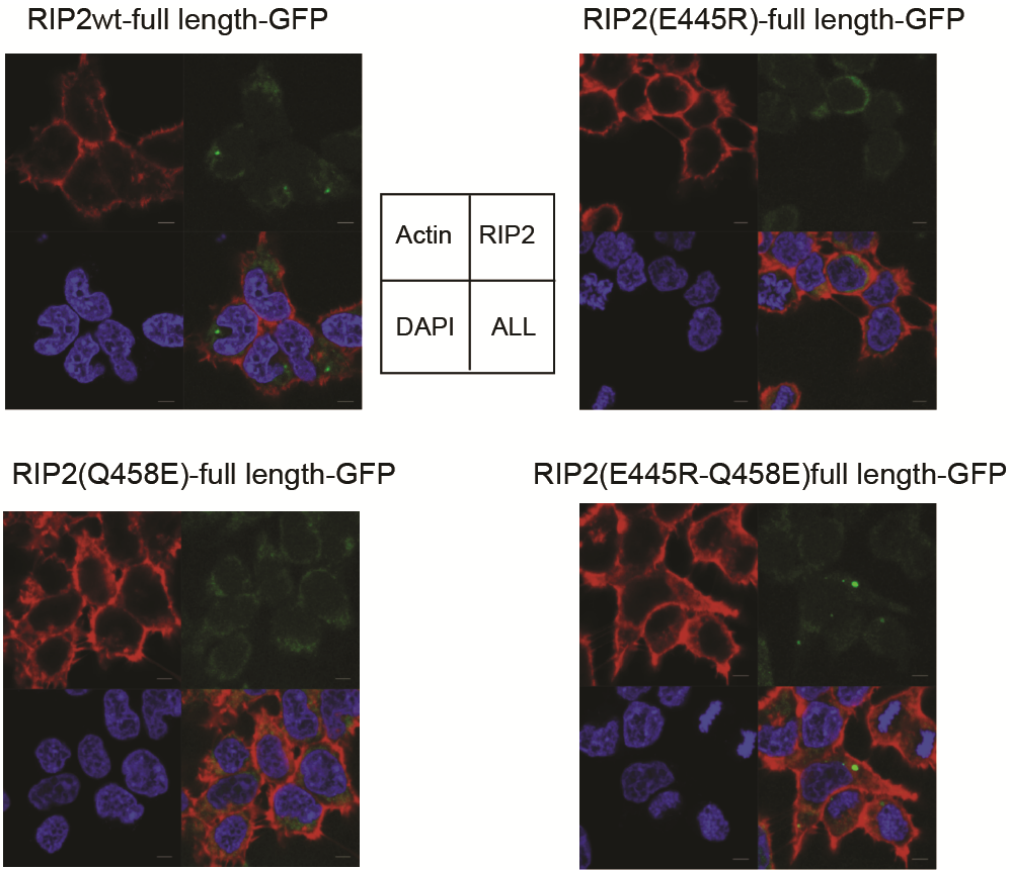

Figure 3.17. Confocal microscope images of wild-type RIP2–GFP, RIP2 (E445R)–GFP, RIP2 (R458E)–GFP, and the double mutant RIP2 (E445R–R458E)–GFP. The charge-reversal double mutant regained the puncta formation activity. Grey scale bar: 5 μm.

3.6 Characterization of Interaction Mode between NOD1/2 with RIP2

From the previous results of *in-vitro* reconstituted assays, recombinant seeds of NOD1 CARD and NOD2 CARD were independent to trigger the oligomerization of RIP2 CARD. RIP2 CARD, NOD1 CARD, and NOD2 CARD seeds were injected into superdex 200 column for size-exclusion chromatographic analysis. All the fractions were analyzed by SDS-PAGE gel (Figure 3.18a). To further confirm the interaction between NOD1/2 and RIP2, refolded RIP2 monomers were incubated with NOD1 CARD and NOD2 CARD seeds. All the samples were also injected into column, and then loaded in to SDS-PAGE for analysis (Figure 3.18b).

a

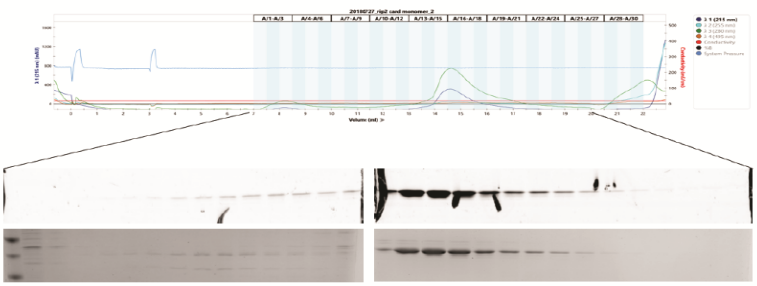

RIP2-CARD-SNAP alone profile

RIP2-BG-647 Stain

Commassie Stain

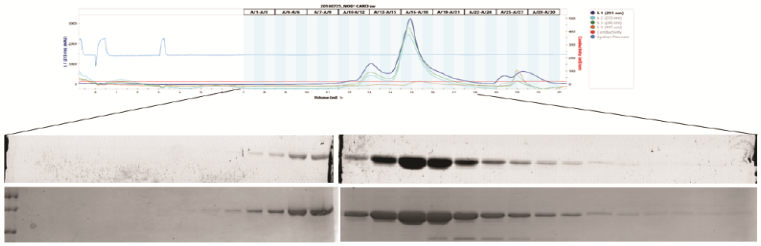

NOD1-CARD-SNAP alone profile

NOD1-BG-647 Stain

Commassie Stain

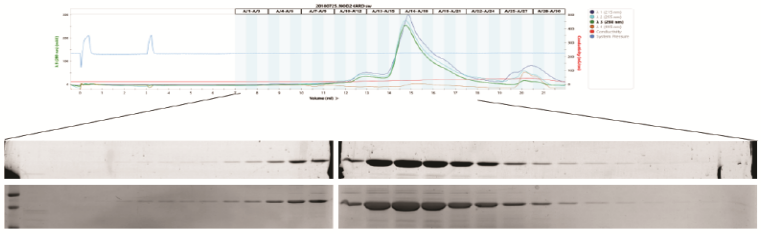

NOD2-2CARD-SNAP alone profile

NOD2-BG-647 Stain

Commassie Stain

b

= Newly induced RIP2-CARD oligomer population

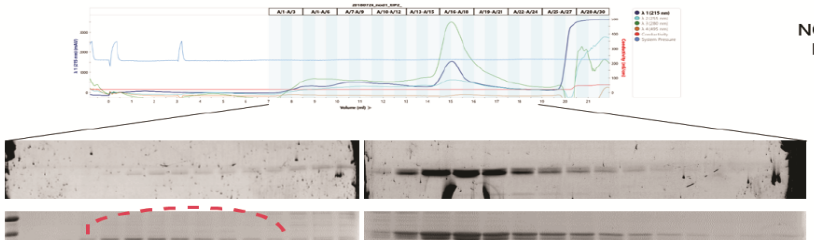

NOD1-CARD-SNAP + RIP2-CARD-SNAP

NOD1-BG-647 Stain

Commassie Stain

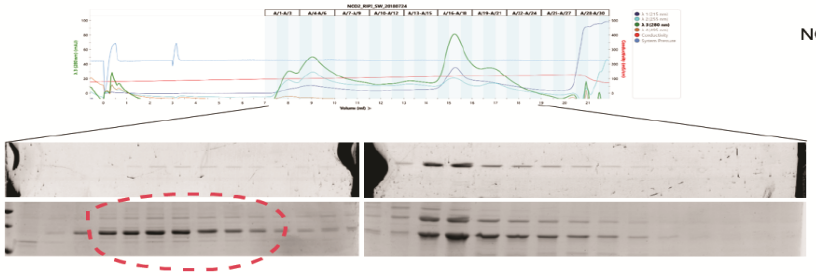

NOD2-2CARD-SNAP + RIP2-CARD-SNAP

NOD2-BG-647 Stain

Commassie Stain

Figure 3.18. (a) Size exclusion chromatographic analysis and SDS-PAGE results of NOD1-CARD, NOD2-2CARD and RIP2-CARD. 600 µl of 20 µM protein solutions dissolved in PBS buffer was injected into 10/300 superdex 200 column. The running profile was recorded using Bio-Rad NGC system. (b) Size exclusion chromatographic analysis and SDS-PAGE results of the mixture of NOD1-CARD/RIP2-CARD, and mixture of NOD2-2CARD/RIP2-CARD. 600 µl of 20 µM protein solutions dissolved in PBS buffer was injected into 10/300 superdex 200 column. The running profile was recorded using Bio-Rad NGC system.

Compared to the NOD1 CARD seeds and NOD2 CARD seeds alone, an extra peak containing oligomeric RIP2 CARD was observed when they were incubated with RIP2 CARD monomers (Figure 3.18a/b). RIP2 CARD monomers could be stimulated by NOD1/2 CARD seeds to form high-order oligomers.

To have a better understanding about the formation of RIP2 CARD filament, RIP2 CARD monomers were incubated with RIP2-CARD-SNAP seeds, which were imaged under EM (Figure b). RIP2-CARD-SNAP seeds formed the short and thick chunks, which were extended by RIP2 CARD monomers to form thin filaments.

Looking insight into the interaction of NOD1/2 and RIP2, the oligomerization of RIP2 CARD was initiated by the stimulated NOD1/2 CARD seeds. However, the newly formed and oligomeric RIP2 CARD have a faster migration speed than NOD1/2 seeds, which was observed and analysed by EM to demonstrate whether NOD1/2 might form a stable complex with stimulated RIP2 CARD oligomers. The EM results supported the observation of heterogeneous complexes formed by NOD1/2 and active RIP2 CARD (Figure b). These complexes were transient and unstable in comparison to the compact and homogenous filaments stimulated by recombinant RIP2 CARD.

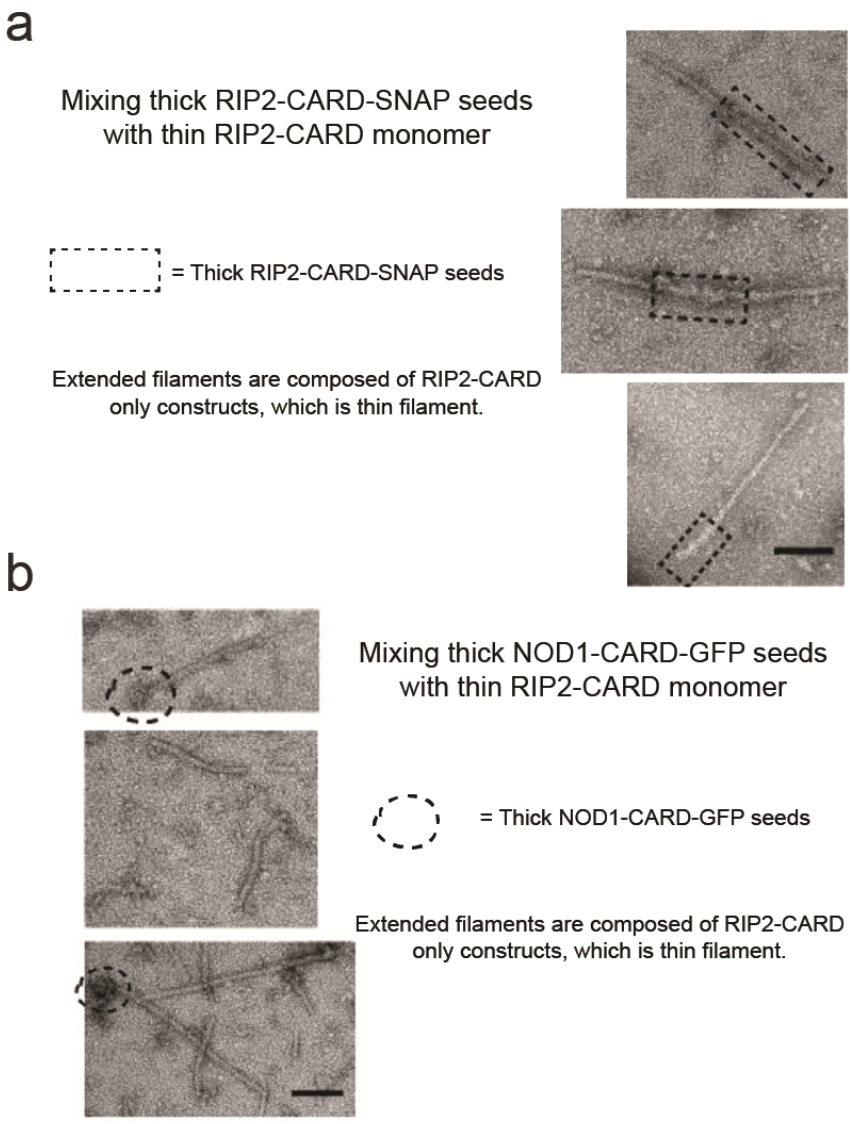

Figure 3.19. (a) Negative stain EM images of thin RIP2-CARD filaments. Thicker diameter of RIP2-CARD-SNAP were used to indicate the location of the seeds. RIP2-CARD-SNAP seeds (highlighted by dash boxes) formed stable complex at the ends of the newly extended thin RIP2-CARD filaments. Scale bar: 100 nm. (b) Negative stain EM images of thin RIP2-CARD filaments seeded by NOD1-CARD-GFP. Thicker diameter of NOD1-CARD-GFP (highlighted in dash circles) indicated the location of the seeds. NOD1-CARD-GFP seeds formed less stable complex with the newly extended thin RIP2-CARD filaments. Scale bar: 100 nm.

To confirm that the stimulated oligomers is not formed by the crowding effects. RIP2 CARD and NLRC4 CARD monomers were used to perform oligomerization assays, exhibiting that

oligomerization happened only when monomers are stimulated with their corresponding seeds (Figure 3.20).

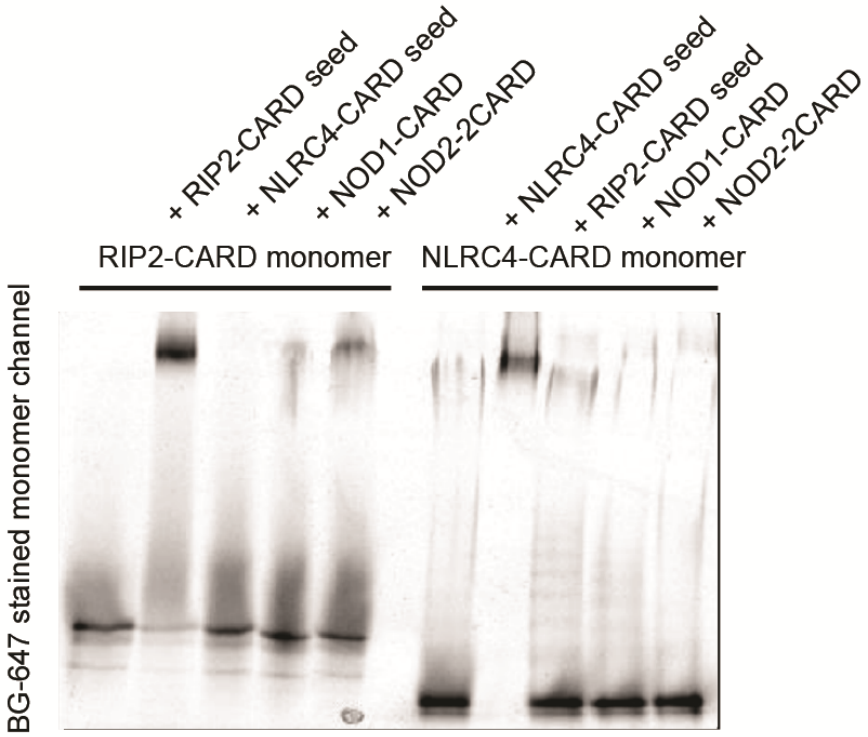

Figure 3.20. CARD-CARD interaction induced oligomerization requires specific pairing of the interaction partners. When coincubation 10 μM RIP2-CARD or NLRC4-CARD monomers with different seed complexes, only their corresponding functionally relevant seeds (NOD1/2 and RIP2 for RIP2, NLRC4 for NLRC4) could efficiently stimulate the oligomerization of the monomers. NLRC4 failed to activate RIP2, and vice versa. 5 μM of different seed complexes were used.

The next goal was to identify how NOD1/2 interacts with RIP2. Primary sequences of CARD domains are poorly conserved, which makes the prediction of the mode of potential interactions difficult. It is still unknown whether it is the first CARD of NOD2 or the second CARD responsible for the recruitment of RIP2 CARD. There are three different ways for CARD-CARD interactions, including top-down, bottom-up and bidirectional modes. Two

sets of fused proteins were produced to identify the interaction mode for NOD1/2 and RIP2 (Figure 3.21a).

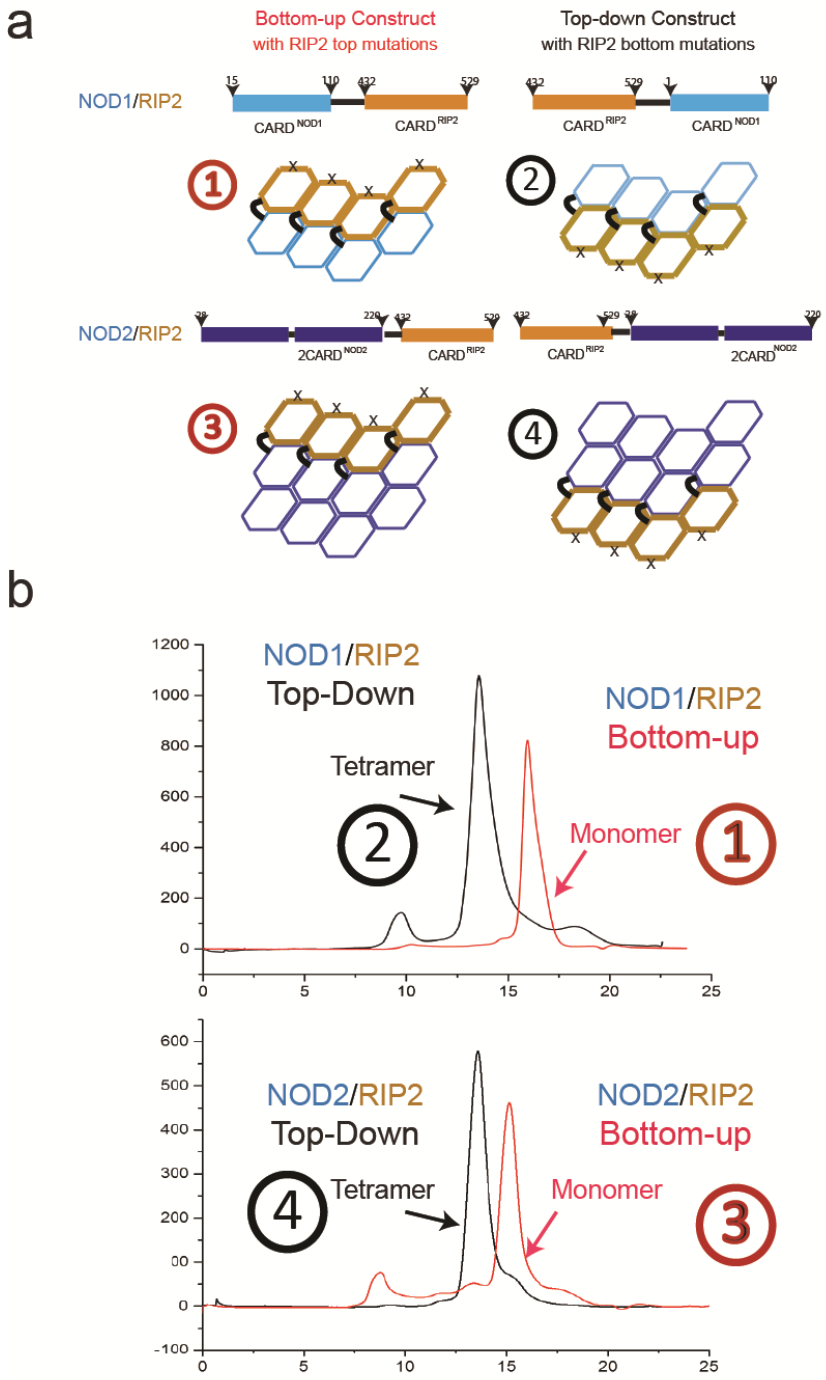

Figure 3.21. Both NOD1 and 2 activate RIP2 in a top-down interaction mode. (a) The design of NOD1/RIP2 and NOD2/RIP2 fusion constructs. According to RIP2-CARD structural model, mutations located on RIP2–CARD surfaces were introduced to prevent aggregation. (b) Size-exclusion chromatographic profiles of bottom-up and top-down constructs of

NOD1/RIP2 and NOD2/RIP2 fusions. Both top-down constructs appeared to form stable tetramers in solution, not the other way around. Since RIP2–CARD tends to self-oligomerize, N449A–K513E mutant of RIP2–CARD domain was used to prevent self-interactions in bottom-up constructs, and R444E–E445R mutant of RIP2–CARD domain was used in top-down constructs. Without incorporating the RIP2–CARD mutations, fusion constructs precipitate.

The first set has C-terminal (up position) RIP2–CARD with either NOD1–CARD or NOD2–CARD at the N-terminal (bottom position). The domain architecture was reversed for the second set of constructs. To prevent possible aggregation of RIP2 CARD, mutations were introduced based on the structure of RIP2 CARD filament. The top mutations N495A/K513E were engineered in the first set of fusion constructs, and R44E/E445R located in the bottom surfaces of RIP2 were designed to second pairs of fusion constructs for the silence of RIP2 oligomerization. These fusion constructs were all expressed and purified, producing a significantly different profile of size exclusion chromatography (Figure 3.21b). The set of top-down constructs reached a peak about ~120kDa, four times bigger than their monomers size, while the bottom-up fusion proteins were still monomeric size about 30kDa. This observation suggested that top-down fusion proteins formed tetrameric complexes stably, suggesting that NOD1 and NOD2 adapts a top-down mode to activate RIP2 by transient and cooperative interactions with top surfaces of RIP2.

The mutations located at either top or bottom of NOD1 and NOD2 were engineered to silence the activity of CARD in cellular signals, assessed by luciferase reporter assays (Figure 3.22a). The top-down mode of interaction for NOD1/2 and RIP2 is consistent with previous observations that Lys67 in NOD1 did not affect the interaction between NOD1 and RIP2, while Arg69 and Lys70 were critical for the interaction (Mayle, Boyle et al. 2014), as well as the hypothesis that NOD2–CARDa was responsible for direct RIP2 interaction (Fridh and

Rittinger 2012). It is reported that several residues located in the first CARD of NOD2 were critical for the interaction of NOD2 and RIP2; however, there was no detectable NOD2 expression in HEK293T cells according to the western blotting experiments (Figure 3.22b).

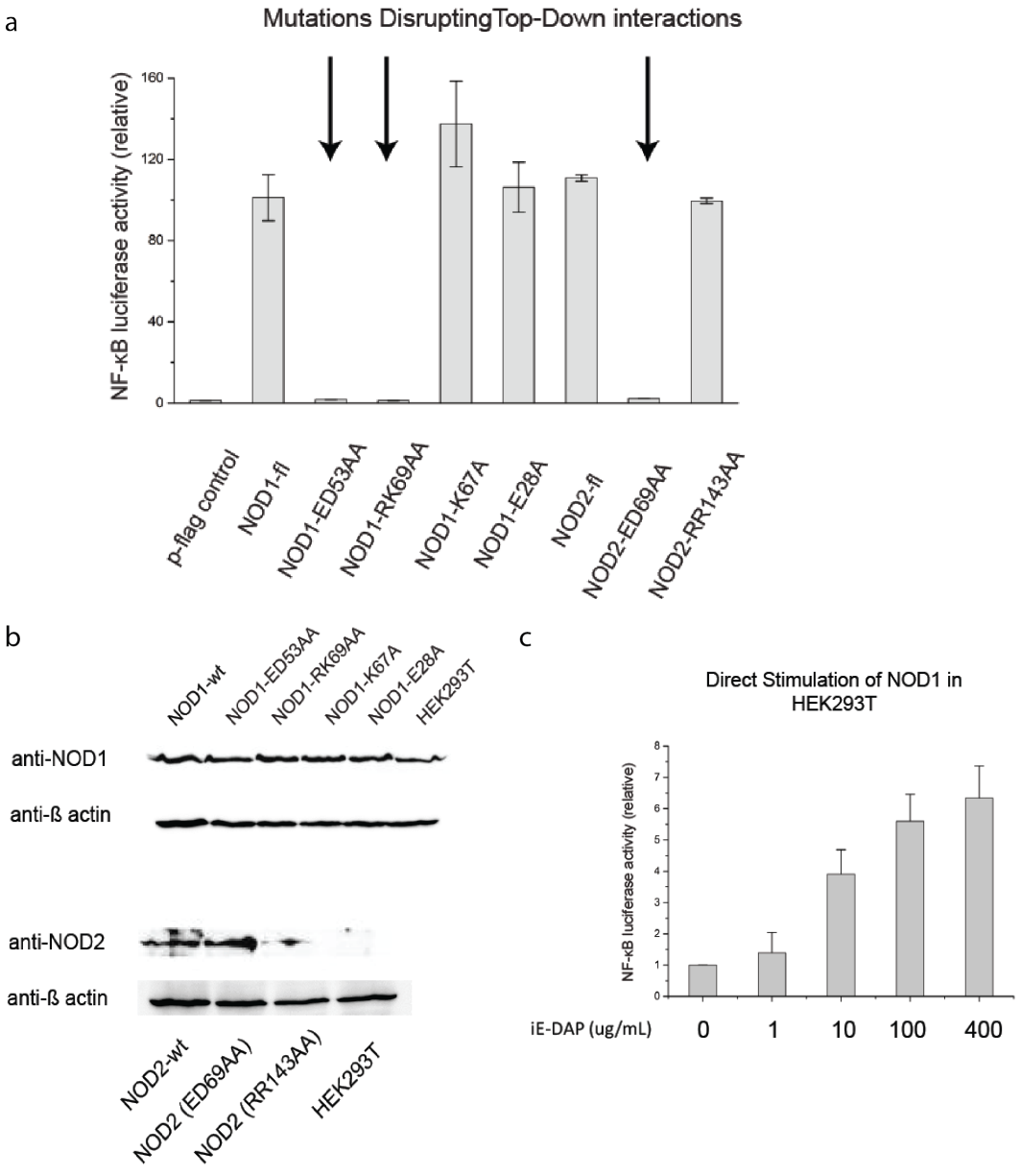

Figure 3.22. NF-κB promoter activation by NOD1, NOD2, NOD1 mutants, and NOD2 mutants in HEK293T cells. HEK293T cells were transfected with empty vector, wild-type NOD1, wild-type NOD2, NOD1 mutants, and NOD2 mutants together with pGL4.32 NF-κB-RE vector and CMV-Renilla vectors. Cells were harvested 24 h post-transfection and the level of NF-κB promoter activity was measured by dual luciferase assay according to the

manufacturer's instructions. (b) Expression levels of NOD1, NOD2 constructs, and their mutants were similar. HEK293T cells were transfected with wild-type NOD1/2 as well as their mutants. Endogenous levels of NOD1 and NOD2 in HEK293T cells were also monitored. Western blots were representative of three independent experiments. (c) NF-κB promoter activation after iE-DAP stimulation in HEK293T cells. Error bar represents standard deviation values of three independent repeats.

A weak signal from NF-κB luciferase reporter assay was detected when HEK293T cells were transfected with iE-DAP, demonstrating that NOD1 is endogenously expressed by cells (Figure3.22c). Mutations on the top surface of NOD1 and NOD2 did not affect the downstream signaling, while the mutations on the bottom surfaces severely abrogated their activities (Figure 3.23). This observation is in agreement with the RIP2 filament models based on the biochemical analysis.

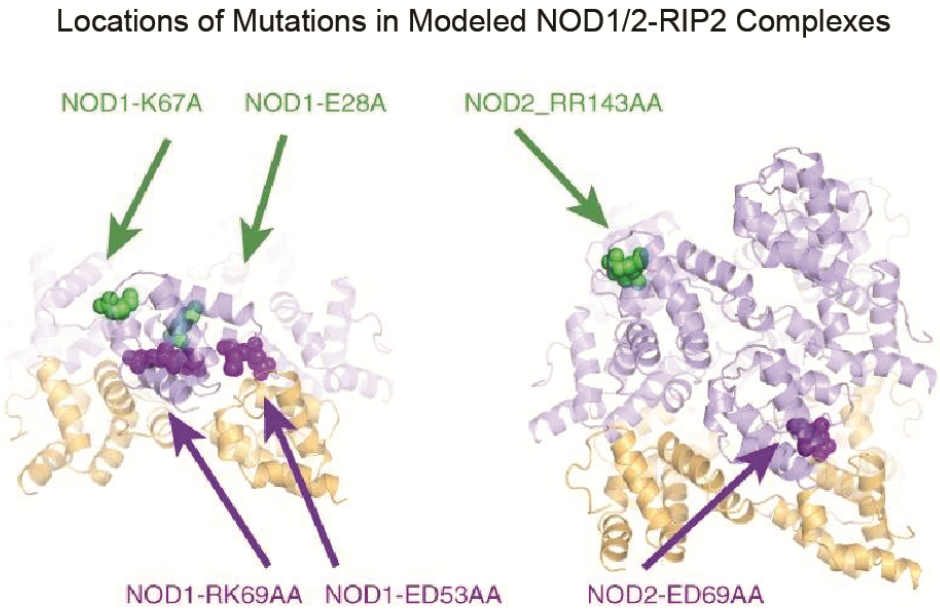

Figure 3.23. Illustrations highlighting the locations of the NOD1/NOD2 mutations tested in Figure a. Green arrows highlighted mutations on the top surfaces of NOD1/2 CARD domains, while purple arrows highlighted the bottom mutations. Only bottom surfaces from NOD1/2

CARD domains were functionally important. RIP2 utilizes the same interface to interact with both NOD1 and NOD2.

Table 2. Data collection, map and model refinement, validation

Data Collection	
Microscope	Tecnai Polara
Voltage (kV)	300
Detector	K2
Pixel size (Å)	1.23
Defocus range (μm)	-2
Electron Dose (e-/A2)	8
Helical Reconstruction	
Software	RELION 2.0
Segment length (Å)	200
Particles	142,230
Helical rise (Å)	4.936
Helical rotation (°)	-101.373
Resolution (Å)	3.6
Coordinate Refinement (mid-segment 12mer)	
Software	Phenix
Unit Cell Dimension (Å)	76.26 x 76.26 x 76.26
Resolution Cut Off	3.5
Rwork	0.4415
Rfree	0.4545
Model	
Number of residues	1044
B-factor overall	202.7
R.M.S. deviation	
Bond length (Å)	0.007
Bond angle (°)	0.994
Validation	
Molprobity clashscore (percentile)	8.18
Rotamer Outliers (%)	0
Cβ deviation (%)	0
CC* central segment density	0.6988
CC* model (5YRN) to map	0.8083
CC* (3.9 – 3.5 Å)	0.1982
Ramachandran plot	
Fovored (%)	95.29

Allowed (%)	4.71
Outliers (%)	0

3.7 Discussion and Conclusion

The signaling pathway stimulated by NOD1/2 and RIP2 has been studied for years in innate immunity (Fridh and Rittinger 2012, Maharana, Pradhan et al. 2017). The molecular mechanism of the oligomeric signaling complexes formed by NOD1/2 and RIP2 was not fully understood in the previous publications. The *in-vitro* reconstituted assay provided with a powerful tool to prepare homogenous and straight filamentous samples, which are suitable for structural studies. The atomic structure demonstrates that the formation of RIP2 CARD filament is contributed by the Type I and Type II interactions.

It is common to find that many filamentous complexes participate in the signaling pathway of cellular immunity. There are several other high-ordered complexes with helical symmetries that act as innate immune adapters, including MAVS in RLR signaling pathways, ASC in canonical inflammasome complexes and Myd88 in TLR signaling pathways. Surprisingly, these complexes consisting of DD superfamily domain (MyD88/ IRAK4, RLR/MAVS, and NOD1/2/RIP2) share strikingly similar helical parameters (Ferrao and Wu 2012, Wu, Peisley et al. 2014). Besides, filamentous complexes formed by ASC CARD were also proposed to have the same helical symmetry (Lu, Magupalli et al. 2014, Li, Fu et al. 2018). It is almost the same for the helical parameters of these oligomeric complexes. These DD containing proteins are reported to mediate versatile signaling events, which are critical for Autophagy, necrosis, pyroptosis, apoptosis, and other life-or-death decisions (Cadwell 2016, Man and Kanneganti 2016). The shared overall helical parameters among different filamentous complexes indicate that death domains potentially play complicated functional roles in cellular activities.

In this chapter, I exhibited that stimulated RIP2 forms a helical oligomeric structure to propagate immune signals. My findings contribute to the understanding of how DD containing proteins interact with each other to facilitate cellular signals.

It is illustrated by biochemical and cellular data that the bottom surfaces of the NOD1 CARD and the second CARD of NOD2 are responsible for the interaction and oligomerization of RIP2. Their interactions are similar to those in RIG-I/MDA5 and MAVS signaling pathways. For both MAVS and RIP2, they interact with their upstream proteins in a transient way.

In the native intracellular signaling environment, the stability of the seeding complexes is enhanced to regulate innate immune activities by cellular cofactors, including bacterial substrates-induced oligomerization of NOD1/2, K63-polyubiquitin and/or virus-induced oligomerization of RIG-I/MDA5 and so on. The high concentration of NOD1/2 seeds was used in the *in-vitro* reconstituted assays to reduce the requirement of the participation of cofactors. Further investigations are required to identify posttranslational modifications and potential cofactors of NOD1/2 and RIP2, providing with more insights into how the innate immune signaling pathways are regulated. The RIP2 CARD filamentous structure solved by cryo-EM in this chapter could help to interpret disease-associated mutations in NOD1/2 and RIP2.

The reason why multiple upstream proteins could activate the same downstream adaptor is due to the flexible surface pairing of the CARD domain by Type I and Type II residues. The MAVS CARD is more homologous with the second CARD of RIG-I and MDA5. RIG-I and MDA5 use their second CARD to mediate the interaction and activation of MAVS CARD. Their interactions are mainly supported by the interfaces of Ia/Ib and IIa/IIb (Wu, Peisley et al. 2014). The hydrophobic residues, including F16 and W56 located at Ia interface of MAVS CARD, contribute to the versatile interaction with Ib interfaces of RIG-I 2CARD and MDA5 2CARD (Wu, Peisley et al. 2014). The type II interactions among them are mediated by

charged residues, including D6/R64/R65/R37 located on the MAVS CARD, E178/ K181/R179 located on RIG-I 2CARD and D133/T188 located on MDA5 (Wu, Peisley et al. 2014). These results in the plasticity of the MAVS surface, allowing its interaction with different upstream proteins to form a convergent signaling pathway. Similar to MAVS, RIP2 also exhibits its versatility to interact with NOD1 and NOD2, mediated by type I and type II interactions. Their flexible side chains indicate the intrinsic mosaicity for such surfaces, and it is possible that their versatile interaction reflects the transient interaction between NOD1/2 and RIP2 CARD for the nucleation of RIP2 filament. NOD1 and NOD2 act as a nucleating template to trigger the formation of multiple RIP2 filaments, leading to the sufficient amplification of immune signals. It is required more investigations and studies to have a better understanding of the CARD-CARD specificity for the convergent signaling pathways.

Chapter 4. Structural Characterization of NLRC4 in Innate Immunity

In the innate immune system, immune responses are essential to fight against the pathogenic attack and drive inflammation for removal pathogens. The inflammasomes are cytoplasmic complexes to perform immune responses by regulatimg the release of cytokines and induction of pyroptosis in a dependent manner of caspase-1 (Rathinam, Vanaja et al. 2012). The inflammasomes assembled by NLRC4 detect the ligands from bacteria, including flagellin and a TTSS rod component (Zhao, Yang et al. 2011). Activated NLRC4 oligomerizes to recruit caspase-1 by homotypic CARD-CARD interaction to form NLRC4-inflammasomes for propagating immune signals (Zhao, Yang et al. 2011).

AIM2 induced inflammasomes are triggered by dsDNA located in the cytosol; NLRP3 dependent inflammasome is stimulated by K^+ efflux; NAIP proteins detect flagellin and component proteins of the bacterial type III secretion system (Zhao, Yang et al. 2011). Activated NAIP proteins recruit downstream adaptor NLRC4, which subsequently engages the immune effector caspase-1. Canonical inflammasomes are dependent on the ASC adaptor, consisting of an N-terminal PYD and a C-terminal CARD. ASC interacts with upstream proteins by its N-terminal PYD and recruits caspase-1 by homotypic CARD-CARD interactions. In contrast, activated NLRC4 uses its N-terminal CARD to recruit caspase-1 for signal propagation directly. Caspase-1 is the universal adaptor for canonical inflammasomes, which results in the activation and dimerization of caspase-1 via its CARD to form filament structures. Activated caspase-1 processes pro-cytokines to mature cytokines for immune responses.

In this study, the filamentous structure of NLRC4 CARD is revealed to form filament that is similar to that of caspase-1 CARD. In this way, the NLRC4 oligomer provides a template for caspase-1 and ASC polymerization. To validate the NLRC4 CARD filament model, mutagenesis and biochemical assays have been conducted. Interestingly, I found that NLRC4

can activate both ASC and caspase-1 to conduct divergent signaling pathway, using the same NLRC4 CARD domain.

In NLRs, there are four members in the NLRC subfamily including NLRC1 (also called NOD1), NLRC2 (also called NOD2), NLRC3, and NLRC4. NLRC3 is a pseudogene. In this way, my thesis covers all NLRCs.

4.1 Structural and Biochemical Studies of Activated NLRC4 CARD

NLRC4 is reported to activate and nucleate the assembly of caspase-1 (Wu, Fernandes-Alnemri et al. 2010). To have a better understanding of the molecular mechanism during the activation process, NLRC4 CARD filaments were prepared for cryo-EM study. To obtain NLRC4 CARD straight and single filaments, SNAP-NLRC4 CARD (residue 1-102) construct was engineered to be overexpressed by *E. coli* (Figure 4.1a). Followed by the same protocol of how to prepare for RIP2 CARD filaments (Gong, Long et al. 2018), NLRC4 CARD-SNAP filaments were obtained and examined under negative staining EM. To achieve high-resolution NLRC4 CARD filament, the SNAP-tag was removed to expose the core filament of NLRC4 CARD (Figure 4.1b).

The sequence alignment was done for NLRC4 CARD, Caspase-1 CARD, ASC CARD, NLRP1 CARD and CARD8. Their sequence similarity was poorly conserved (Figure 4.1c).

To obtain straight and single filaments of NLRC4-CARD, refolded NRLC4-CARD monomers were optimized until all the monomers were recruited by NLRC-CARD seeds to form long filaments.

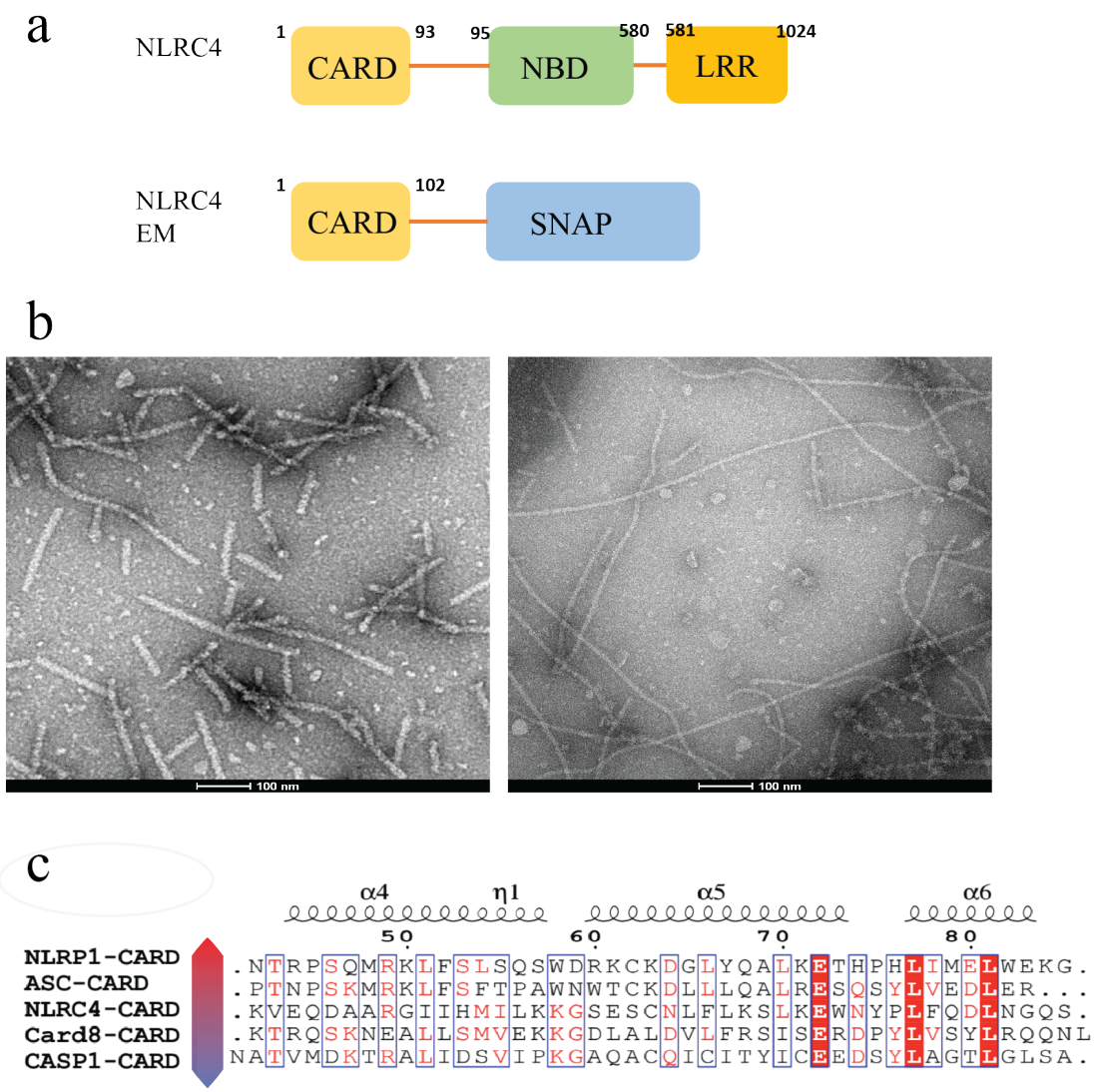

Figure 4.1. Architecture of NLRC4 for filament formation. (a) Architecture of NLRC4 consists of N-terminal CARD domain, followed with nucleotide-binding domain (NBD) and C-terminal LRRs. EM construct for NLRC4 CARD is fused with a C-terminal SNAP protein for stabilization. (b) Negative staining micrographs of NLRC4-CARD SNAP and NLRC4-CARD filaments. (c) Sequence alignment of NLRC4-CARD, ASC-CARD, Caspase-1-CARD, NLRP1-CARD, and NLRP1-CARD. Conserved residues are highlighted in red.

The NLRC4 CARD filaments were imaged by EM. A similar strategy used for RIP2 CARD filament reconstruction was performed to determine the NLRC4 CARD filament structure. NLRC4 CARD filaments images were collected by cryo-EM and thousands of filaments were

picked for 2D classification (Figure 4.2a-c). Based on the power spectrum, the parameters for NLRC4 CARD filament were set as a single-helical symmetry with an azimuthal angle of -100.50º and an axial rise of 5.10 Å per subunit. RELION software was used for 3D classification and refinement. The final volume contains observable α-helices with refined helical symmetry parameters of -100.48º rotation angels and 4.93Å per subunit. After refinement by Coot and Phenix, the resolution was measured at 3.3Å (Figure 4.3a).

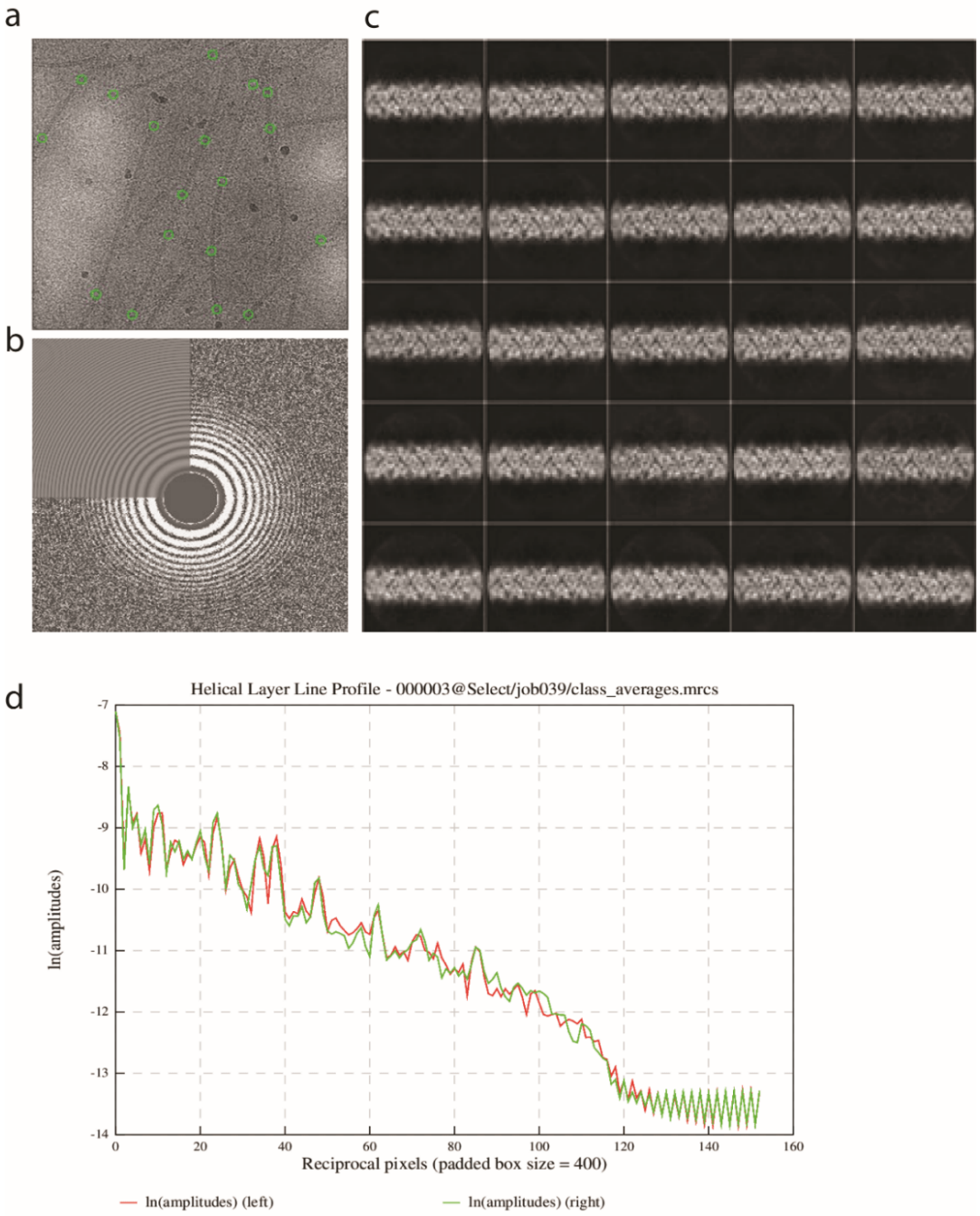

Figure 4.2. Cryo-EM structure determination of NLRC4-CARD filaments (a) Representative images of NLRC4-CARD filaments by cryo-EM. (b) Power spectrum map of cryo-EM micrographs. (c) 2D classification of NLRC4-CARD filaments. (d) Helical layer line profile of NLRC4-CARD filaments.

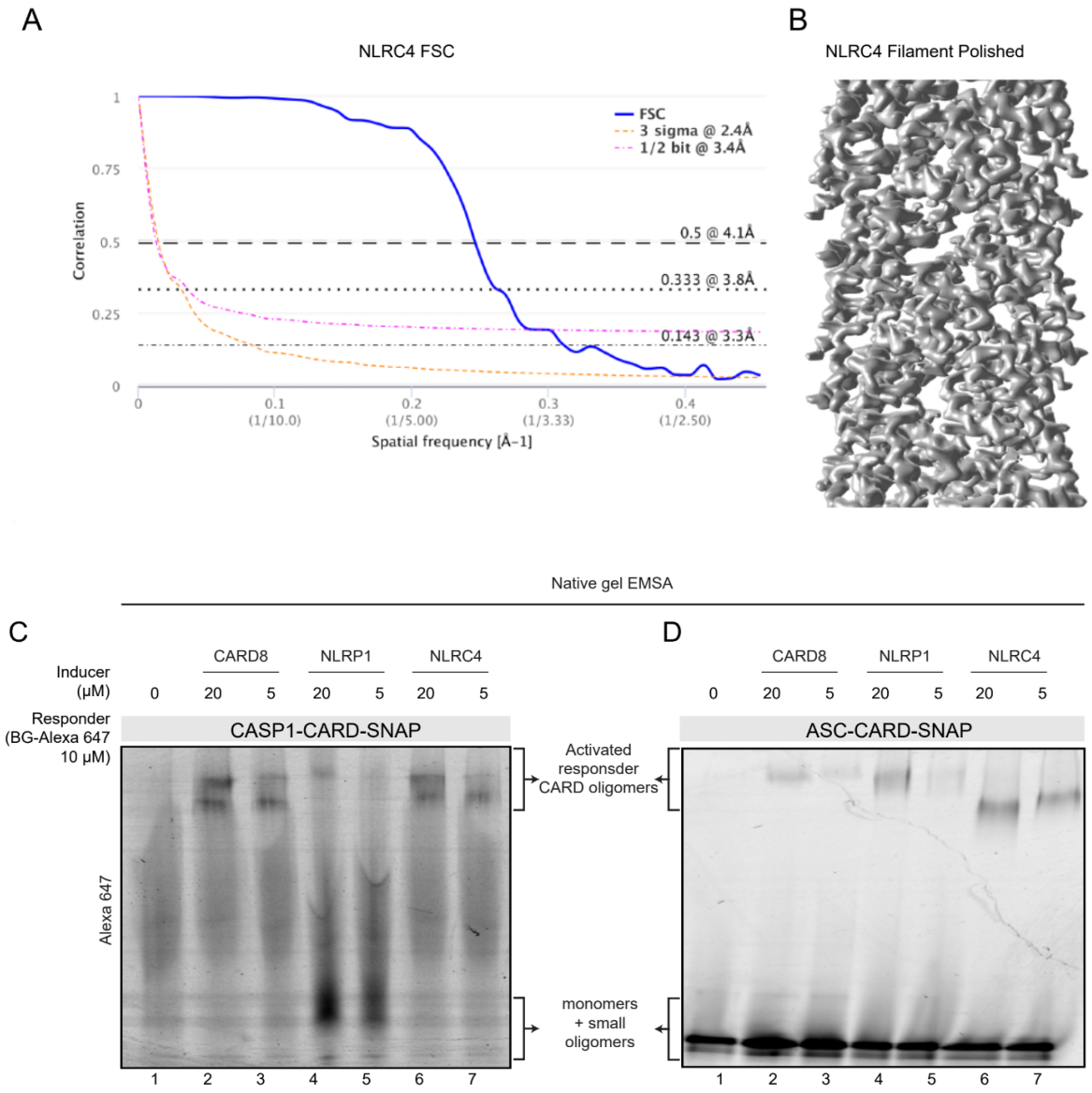

Figure 4.3. Cryo-EM structure of NLRC4-CARD filaments. (A)FSC plot of final, post-refinement NLRC4-CARD filament density. (B) Post-refinement 3D density of NLRC4-CARD filament. (C) Native gel shift assay of recombinant caspase-1-CARD-snap oligomerization induced by NLRC4-CARD. (D) Native gel shift assay of ASC-CARD-snap oligomerization induced by purified NLRC4-CARD.

The NLRC4 CARD filament is similar to the RIP2 CARD filament with a diameter of ~8nm and a central hole (Gong, Long et al. 2018). Wild-type NLRC4 CARD seeds readily recruited refolded Caspase-1-CARD-SNAP and refolded ASC-CARD-SNAP monomers to their ends and formed oligomeric complexes. This interaction between NLRC4 CARD and Caspase-1 CARD/ ASC-CARD was observed with native gel EMSA (Figure 4.3C/D). NLRC4 CARD could activate downstream adaptors ASC and Caspase-2 by homotypic CARD-CARD interaction.

Like RIP2 CARD filament, each subunit of NLRC4 CARD filament interacts with its neighbouring molecules by three different types of interactions (Figure 4.4). These interactions were named as TypeI (Ia:Ib), Type II (IIa:IIb), and Type III (IIIa:IIIB) interactions.

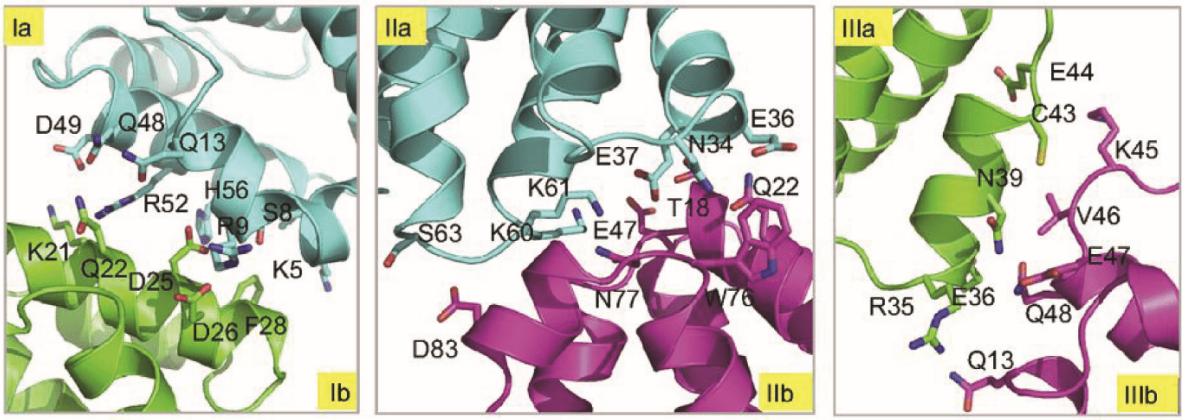

Figure 4.4. Detailed type I, II and III interfaces, respectively, of the NLRC4-CARD filament structure, adapted from (Li, Fu et al. 2018).

In the filamentous structure of NLRC4 CARD, Type III interaction mediates the intrastrand contact, and Type I and II interactions are responsible for interstrand contacts. The type I interaction consists of electrostatic complementary residues of R9, D25, D26, and R52, forming charge-charge interactions at the interface. For the type II interface, K60/K61 and

E47 interact with each other by charge-charge interactions. For type I interaction, the hydrophilic residues are responsible for interactions, including K45 and E44.

To further validate the NLRC4 CARD filament model, the charge-reverse mutagenesis is performed, which is elucidated in the RIP2 CARD filament validation. According to the results of EMSA, R9D mutants cannot induce the oligomerization of WT NLRC4 CARD monomer, while R9D/D26R regains its ability to activate NLRC4 CARD monomer for oligomerization (Figure 4.5).

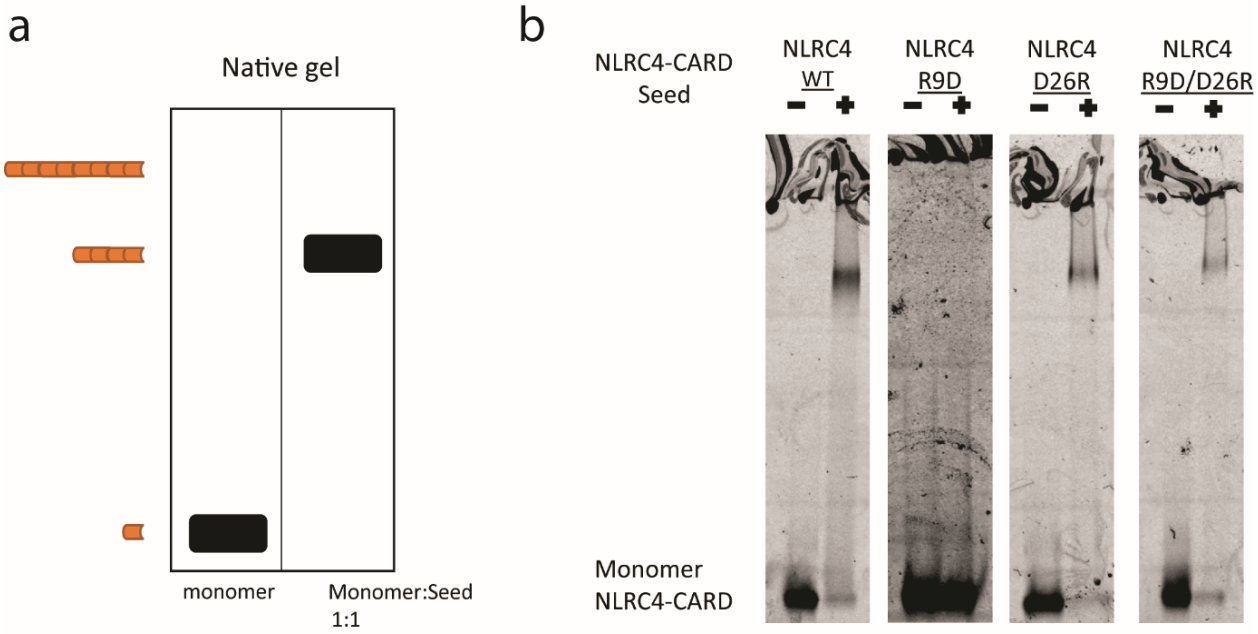

Figure 4.5. Validation of NLRC4-CARD filament structure by reverse-charge mutagenesis. (a) Cartoon demonstration of NLRC4-CARD oligomerization process. Monomers run faster than oligomers and are located in the bottom line of native gel. (b) NLRC4 WT, R9D, D26R and R9D/D26R seeds induce the oligomerization of wildtype of NLRC4-CARD monomers.

Previous studies have shown NLRC4 with deleted N-terminal CARD forms 11- to 12- folded disk-shaped complexes with ligands-bound NAIP proteins, with a central hole of ~8nm in diameter and an outer diameter of ~30 nm (Zhang, Chen et al. 2015). The size of the hole is compatible with the ~8nm diameter of NLRC4 CARD filament structure. Another study has

demonstrated NAIP-activated full-length NLRC4 inflammasome by cryo-electron tomography (cryo-ET) contains a shallow, helical structure with a diameter of ~28.0nm, 11.6 subunits per turn and a helical pitch of 6.5nm (Diebolder, Halff et al. 2015). This structure consists of a rod-shaped volume in the centre that was designated as the CARD column. The NLRC4 CARD filament can be fitted into the cryo-EM structure since they share a similar helical rise per subunit (~5.7 ±0.3Å for NLRC4 full-length and 5.1 Å for NLRC4 CARD filament).

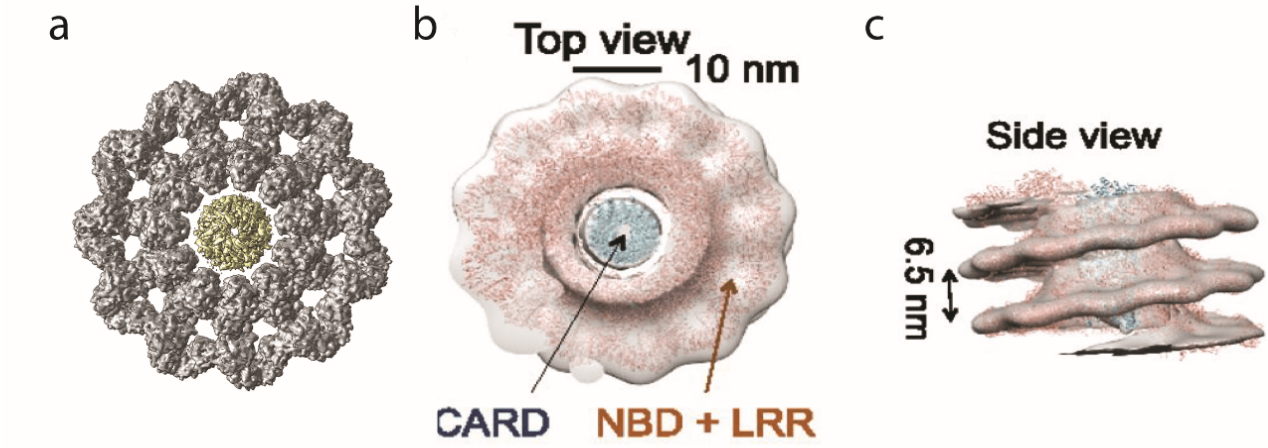

Figure 4.6. Structural analysis of NLRC4. (a) NLRC4-CARD filament is fitted into the 12-disk complex of NAIP activated NLRC4 (ΔCARD) structure, colored by yellow and grey, respectively. (b) Fitting of NLRC4- ARD filament structure (blue) and NLRC4 (ΔCARD) structure into the NLRC4 tomography map with top view. (c) Side view of structure described in (b), adapted from (Li, Fu et al. 2018)

In the process of the NLRC4 CARD filament project, another group published their NLRC4 CARD filament structure online (Li, Fu et al. 2018). We fitted our 3.3Å NLRC4 CARD filament with its 3.58Å structure (Figure 4.6a-c). According to detailed comparison, the two structures are almost identical with similar helical parameters.

Table 3. Data collection, map and model refinement, validation

Data Collection	
Microscope	Tecnai Polara
Voltage (kV)	300
Detector	K2
Pixel size (Å)	1.23
Defocus range (μm)	-1
Electron Dose (e-/A2)	40
Helical Reconstruction	
Software	RELION 2.0
Segment length (Å)	200
Particles	382715
Helical rise (Å)	5.17
Helical rotation (°)	-100.55
Resolution (Å)	3.3
Coordinate Refinement	
Software	Phenix
Resolution Cut Off	3
Rwork	0.2571
Rfree	0.3057
Model	
Number of residues	1020
B-factor overall	248.57
R.M.S. deviation	
Bond length (Å)	0.002
Bond angle (°)	0.364
Validation	
Molprobity clashscore	0.24
Rotamer Outliers (%)	0
Cβ deviation (%)	0
Rfree (model to map)	0.580
Ramachandran plot	
Fovored (%)	98.1
Allowed (%)	1.9
Outliers (%)	0

4.2 Discussion and Conclusion

It has been proposed to be a general mechanism for innate immune signaling pathways dependent on the formation of high ordered complexes. With the structure of NLRC4-CARD filament, more details are elucidated in the nucleation and polymerization of high ordered assemblies. NLRC4-CARD filament shares a similar way with other high order structures, with three different types of interactions (type I, II, and III). NLRC4-CARD can assemble into filaments for downstream caspase-1 CARD recruitment; however, the helical architecture of full-length NLRC4 provides relatively inefficient support for nucleating caspase-1 filament formation. It is found that the longer of the NLRC4 filaments, while the less efficient of its ability is to recruit caspase-1 for signal transduction. It is suggested that only one end of the CARD filament is preferred for caspase-1 recruitment. *In vivo*, it is argued that NLRC4 forms short helices to maximize caspase-1 activation with endogenous expression levels in cells.

NLRC4 activates the downstream signaling pathway in a divergent way, propagating its immune signals to ASC and pro-caspase-1 by CARD-CARD interaction. Type II interfaces contribute most to the stability of NLRC4 filament and interaction with downstream adaptors. Two small aliphatic residues, Asn77 and Gln82, are important for Type II junctions. Thus, the NLRC4 Type IIb surface displays a flexible surface area, which is compatible with both ASC CARD and caspase-1 CARD for their CARD-CARD interactions. In this way, NLRC4 is a typical example that conducts a divergent signaling pathway by CARD-CARD interaction in innate immunity.

Chapter 5. Conclusions and Future Directions

5.1 Conclusions

In innate immunity, CARD-CARD interaction plays a vital role in the production of cytokines for immune responses. Different PRRs recognize different stimuli and mediate different signaling pathways, while multiple different upstream proteins could activate the same adaptor (convergent), or one PRR protein could trigger different adaptors for different cellular activities (divergent). In my thesis, I studied a typical example of a convergent signaling pathway that NOD1 and NOD2 recruit and activate the same adaptor RIP2 to trigger the NF-κB pathway. The divergent signaling pathway is illustrated by NLRC4 in my thesis, which could activate ASC to form specks and directly trigger pro-caspase 1 for pyroptosis.

In the third chapter, NOD1, NOD2, and RIP2 can trigger NF-κB signals *in vivo*, which is aligned with other studies (Kim, Park et al. 2008, Caruso, Warner et al. 2014). The CARD domains in NOD1 and NOD2 could independently trigger NF-κB signals in HEK293 cells, while neither RIP2 CARD domain nor RIP2 kinase domain could activate NF-κB independently. RIP2 signaling requires a pro-oligomeric CARD domain to propagate immune signals, which advances the basic biological knowledge of NOD1/2 and RIP2 signaling pathway. Oligomeric RIP2 CARD was optimized to form a long and straight filamentous structure, which was solved at a near-atomic resolution of 3.6Å. The high-resolution structure of RIP2-CARD filament was validated by individual mutagenesis and charge-reversal mutagenesis.

The biochemical and cell-based activity data in chapter three demonstrated that the bottom surface of the NOD1-CARD and NOD2 first CARD are the responsible interaction surfaces mediating oligomerization of RIP2. This interaction resembles those seen in RIG-I/MDA5-MAVS signaling pathway (Wu, Peisley et al. 2014): in both MAVS and RIP2, their activators

interact with these adaptor proteins in a transient way. Under conditions of which little or no stable complexes were observed in native gel or size-exclusion chromatography, oligomerization of the downstream adaptor proteins could be induced efficiently.

In the fourth chapter, NLRC4 CARD filament was generated and imaged by EM. The filamentous structure was solved at a resolution of 3.3 Å. Mutagenesis was conducted to validate the high-resolution structure. The density of NLRC4-CARD filamentous structure was fitted well into the holes of NLRC4ΔCARD and the tomographic structure of full-length NLRC4, which contributes to interpretation the function of NLRC4 in the immune inflammasomes. NLRC4 CARD seeds could trigger the activation and oligomerization of ASC CARD monomers and Caspase-1 CARD monomers. The biochemical analysis was aligned well with the current knowledge about the role of NLRC4 in the innate immunity (Zhao, Yang et al. 2011, Li, Fu et al. 2018).

All in all, the 3D structures of RIP2 CARD and NLRC4 CARD filaments make it possible to elucidate the molecular mechanism of the convergent and divergent interactions in innate signaling pathways, which is difficult to explain based on amino acid sequences. The versatile residues in the interfaces enable the death domain-containing proteins to interact with different molecules, providing a structural basis for potential crosstalk of different signaling pathways. The three-dimensional atomic structure is important to explain the molecular mechanism about the interactions and recruitment of different proteins to improve our understanding of signaling pathways for cellular activities.

In recent years, many studies have shown that the developments in Crohn's disease are associated with gain-of-function mutations in the gene of NOD2 (Vasseur, Sendid et al. 2011). Hyperactive NOD2 triggers RIP2 to release excessive immune signals. In 2014, two groups identified gain-of-function mutations in the gene of NLRC4 in four patients, suffering from recurrent autoinflammation and infantile enterocolitis (Canna, de Jesus et al. 2014,

Romberg, Al Moussawi et al. 2014). It is improved in the understanding of how the NLRC4 inflammasome and interleukin 18 (IL-18) contribute to gut inflammation. All NLRC4 inflamasomopathies are categorically autoinflammatory disorders. Until now, there is still no NLRC-specific therapy. All the treatments are aimed at downstream inflammatory mediators. The NLRC CARD filamentous structure, together with the crystal structure of NLRC4ΔCARD, is possible to provide new drug targets for autoimmune diseases.

In the innate immune system, many oligomeric complexes such as RIP2 and NLRC4 amplify immune signals to trigger downstream signaling pathways. Loss-of-function and gain-of-function mutations in these signaling complexes are associated with immune diseases. The high-resolution structures of these complexes provide with more information about these signaling pathways and potential targets for drug design.

5.2 Future Directions

The future directions for this study could be separated into two paths. One is to solve structures of other receptors related to innate immunity. Another is to understand the relationships of different adaptors in the innate immune system.

- I have determined the cryo-EM structure of RIP2-CARD and NLRC4-CARD filaments. Yet t many pattern recognition receptors are important in innate immunity with unknown structures, as reviewed in Chapter 1. For example, ligand-induced NLRP1 is activated to cleave itself at the site of F1213 located in the FIIND. Cleaved N-terminal fragment (containing CARD domain) recruits ASC to form immune inflammasome for host defence. It is important to look into the molecular structure of NLRP1 to have a better understanding of its roles in innate immunity. Plus, for the NOD1/NOD2 signaling pathway, it is also meaningful to solve the structure of NOD2-CARD to provide molecular information for NOD2 related diseases.
- Filamentous structures are not uncommon in cellular immune signaling, as described in Chapter 1. Interestingly, these independent innate immune seeding complexes composed of DD superfamily domains share striking similarities among them. The helical symmetry parameters of the high-order complexes are almost the same. Beyond innate immunity, these proteins are also crucial for apoptosis, necrosis, pyroptosis, autophagy and other events. It is important to explore whether the potentially shared overall helical symmetry among death domains plays complicated functional roles.
- To maintain the stability of innate immunity, it is important to discover inhibitors for the formation of filamentous structures that recruit lots of effectors to release mature cytokines.

- Currently, my lab members and I are working on other CARD-containing proteins, including CARD16, caspase-9, Apaf-1, to explore their functional forms and how they conduct their activities in innate immunity. Besides, I collaborate with other labs to handle some projects related to single-particle reconstruction.

Appendix

Primer sequences

Vector cloning					
gene	domain	Vector	Restriction site	Forward primer (5'-3')	reverse primer (5'-3')
NOD1	Full length	pcDNA3.1	BamHI/XbaI	ATAAGGATCCATGTACCCATACGATGTTCCAGATTACGCTGAGGAGCAAGGTC	ATAATCTAGATCAAAAGCAGATGATGCGTTTTTCATCTTCATAAACTTTCGC
NOD1	CARD	pcNDA3.1	Kpn1/BamHI	ATAAGGTACCATGGAGGAGCAAGGTCATAGCGAG	ATAAGGATCCGCTGAAACCGATTTCCAGCAGCC
NOD1	CARD	pET47	XmaI/EcoRI	ATAACCCGGGGAGAGCCATCCTCATATCCAGCTGCTGAAGAGC	ATAAGAATTCGCTGAAACCGATTTCCAGCAGCCATGGAC
NOD2	CARD	pet47	XmaI/EcoRI	ATAACCCGGGATGGGTGAGGAGGGTGGTAGCGC	ATAAGAATTCCTACCATCTTACAAGTTGCTGCTTCCAGCG
NOD2	Full length	pcDNA3.1	BamHI/XbaI	ATAAGGATCCATGGGTGAGGAGGGTGGTAGCGCATCTCAT	ATAATCTGAGCAGCAGCAGGCGGGTATCGCGACAGCCCAGTTTATCT
NOD2	CARD	pcDNA3.1	HindIII/XhoI	ATAAAAGCTTATGTGCAGCCAAGAGGCATTCCAG	ATAACTCGAGGGGTCCCTGAAAGAGGACTTCCAGCGGCAG
NOD1	CARD	pET47	EcoRI/XhoI	ATAAGAATTCGAGAGCCATCCTCATATCCAGCTGCTGAAGAGC	ATAACTCGAGGCTGAAACCGATTTCCAGCAGCCATGGAC
NOD2	CARD	pET47	EcoRI/XhoI	ATAAGAATTCGATGTGCAGCCAAGAGGCATTCCAGGCTCAGCGTTC	ATAACTCGAGGGGTCCCTGAAAGAGGACTTCCAGCGGCAG
RIP2	CARD	Vsnap-tagT7(2)	XhoI/NotI	ATAACTCGAGCAGCCTGGTATAGCCCAGCAG	ATAAGCGGCCGCCTAATGGTGATGATGGTGGTGCATGCTTTTATTTTGAAGTAAATTTAAAG
RIP	Full	pcDNA3	HindIII/X	ATAAAAGCTTATGGACTACAAGGACGATGACGATAA	ATAACTCGAGTCACATGCTTTTATTTTGAAGTAAATTT

2	length	.1	hoI	GAACGGGGAGGCCATCTG	AAAG
RIP2	CARD	pcDNA3.1	XhoI/XbaI	GATAACTCGAGATAGCCCAGCAGTGGATCCAGAGC	GATAATCTAGACTATGATCTAGAAACCACAAGTATTTCCGGG
MBP	Full length	pcDNA3.1	HindIII/BamHI	ATAAAAGCTTATGGACTACAAGGACGATGACGATAAGAAAATCGAAGAAGGTAAACTGG	ATAAGGATCCAGTCTGCGCGTCTTTCAGGGCTTCATG
RIP2	Kinase	pcDNA3.1	XmaI/EcoRI	ATAACCCGGGAACGGGGAGGCCATCTGCAGCGCC	ATAACTCGAGACTCTGTAACTTTGTTTTCTTTAGCTG
NLRC4	CARD	pcDNA3.1	EcoRI/NotI	ATAAGAATTCATGAATTTCATAAAGGACAATAGCCGAGCC	ATAAGCGGCCGCTTATTCTGATGTCTGATGAAAAAGACTTTGTCC
NLRC4	Full length	pcDNA3.1	Kpn1/XhoI	ATAAGGTACCATGGACTACAAGGACGATGACGATAAGAATTTCATAAAGGACAATAGCCG	ATAACTCGAGTTAAGCAGTTACTAGTTTAAAAGCACCTGTAATAACACTG
MAVS	CARD	pcDNA3.1	HindIII/XhoI	ATAAAAGCTTATGCCGTTTGCTGAAGACAAGACCTATAAGTATATC	ATAACTCGAGCGAGGTCCGAGGCTGGTAGCTCTGGTAGAC

Mutagenesis		
gene	mutation	primer
NLRC4	E36R	CCTATTTGTATGGAATGTTCTGAATCGCAGGGAAGTAAACATCATTTGCTGCGAGAAG
NOD1	ED53AA not47	GAACGACTACTTCAGCGCGGCGGCCGCTGAGATCGTATGCGCATG
NOD1	RK69AA	CTACTCAGCCTGACAAGGTC GCTGCG ATCCTGGACCTGGTACAAAGC
NOD1	K67A	GCATGTCCTACTCAGCCTGAC GCG GTCCGTAAGATCCTGGACCTG
NOD1	E28A	ATCCAGCTGCTGAAGAGCAACCGTGCCCTGCTGGTAACCCATATCCGTAAC
NOD2	ED69AA	CTTGGGAGGTTCTGTCTTGG GCAGCC TACGAGGGTTTCCACCTGC
NOD2	RR143AA	CTCACCGTCCAGCTATCGTA GCTGCT CTGCATTCCCACGTCGAG
RIP2	E445R	AGCCCAGCAGTGGATCCAGAGCAAAAGGAGAGACATTGTGAAC

		CAAATGACAGAAGCCTG
RIP2	R444E	AGCCCAGCAGTGGATCCAGAGCAAAGAGGAAGACATTGTGAAC CAAATGACAGAAGCCTG
RIP2	D492K	GGACCTCAAAAGTCAGACAATTACTAAAAACTACTGACATCCAA GGAGAAGAATTTGCC
RIP2	D461R	ATGACAGAAGCCTGCCTTAACCAGTCGCTAAGGGCCCTTCTGTC CAGGGACTTGATCATG
RIP2	Y474R	CCAGGGACTTGATCATGAAAGAGGACAGGGAACTTGTTAGTACC AAGCCTACAAGGACC
RIP2	Q458E	AACCAAATGACAGAAGCCTGCCTTAACGAGTCGCTAGATGCCCT TCTGTCCAGGGACTTG
RIP2	E472R	CCTTCTGTCCAGGGACTTGATCATGAAAAGGGACTATGAACTTG TTAGTACCAAGCCTAC
RIP2	Q497E	TCAGACAATTACTAGACACTACTGACATCGAGGGAGAAGAATTT GCCAAAGTTATAGTAC
RIP2	K513E	GTACAAAAATTGAAAGATAACGAGCAAATGGGTCTTCAGCCTTA CCCGGAAATACTTG
RIP2	N449D	ATCCAGAGCAAAAGGGAAGACATTGTGGACCAAATGACAGAAG CCTGCCTTAACCAGTCG
RIP2	K471D	GTCCAGGGACTTGATCATG GACGAGGACTATGAACTTGTTAG
RIP2	E475R	CAGGGACTTGATCATGAAAGAGGACTATCGCCTTGTTAGTACCA AGCCTACAAGGACCTC
RIP2	R488E	TACCAAGCCTACAAGGACCTCAAAAGTCGAGCAATTACTAGAC ACTACTGACATCCAAGG
RIP2	R483D	CTTGTTAGTACCAAGCCTACA GAC ACCTCAAAAGTCAGACAATTA
RIP2	D495R	AGACAATTACTAGACACTACT AGG ATCCAAGGAGAAGAATTTGCC

Statistical data of chart plots, with two decimal numbers

Figure 3.2

		avg	std
NOD1	**50ng**	65.01	1.03
NOD1	**200ng**	210.60	8.66
NOD2	**50ng**	73.70	0.85
NOD2	**200ng**	212.14	5.91
NOD1-CARD	**50ng**	42.74	0.91
NOD1-CARD	**200ng**	225.95	4.62
NOD2-CARD	**50ng**	45.03	0.20
NOD2-CARD	**200ng**	175.43	1.64
RIP2	**50ng**	6.10	0.15
RIP2	**200ng**	135.86	4.20
RIP2-CARD	**50ng**	2.04	0.03
RIP2-CARD	**200ng**	12.01	0.29
pFlag	**200ng**	0.81	0.02

Figure 3.3

	Firefly/Renilla						
	SiRNA#1#2						
	NOD1-FL		**NOD1-CARD**		**NOD2-FL**		
	50ng	**200ng**	**50ng**	**200ng**	**50ng**	**200ng**	
avg	6.35	5.17	4.65	4.83	6.39	4.39	
std	0.11	0.06	0.15	0.12	0.25	0.13	
	NOD2-CARD		**RIP2-FL**		**RIP2-CARD**		**Flag**
	50ng	**200ng**	**50ng**	**200ng**	**50ng**	**200ng**	**200ng**
avg	5.33	5.80	15.46	37.78	0.47	0.49	0.37
std	0.22	0.22	0.33	0.80	0.00	0.01	0.01

	siRNA#3#4						
	Firefly/Renilla						
	NOD1-FL		**NOD2-FL**		**RIP2-FL**		
	50ng	**200ng**	**50ng**	**200ng**	**50ng**	**200ng**	
avg	5.26	3.15	6.89	5.57	25.93	68.05	
std	0.29	2.84	0.22	0.03	0.92	3.18	
	NOD1-CARD		**NOD2-CARD**		**RIP2-CARD**		**pFLAG**
	50ng	**200ng**	**50ng**	**200ng**	**50ng**	**200ng**	**200ng**
avg	3.68	4.68	4.42	4.00	0.46	0.54	0.34
std	0.01	0.19	0.19	0.21	0.02	0.03	0.01

Figure 3.4

	NLRC4-FL			**RIP2 kinase NLRC4 CARD**		
	100ng	**200ng**	**500ng**	**100ng**	**200ng**	**500ng**
avg	0.96	1.12	2.20	45.24	86.74	211.49
std	0.02	0.02	0.09	2.53	1.17	2.63
	RIP2 kinase NLRC4 CARD E36R			**RIP2**	**K513E**	**pFlag**
	100ng	**200ng**	**500ng**	**200ng**	**200ng**	**500ng**
avg	0.66	1.12	1.72	49.25	0.63	0.41
std	0.01	0.01	0.08	0.54	0.03	0.03

Figure 3.9

Firefly/Renilla					
RIP2 protein					
	13aa-529	**13aa-540**	**13aa-540 K513E**	**Flag-IS**	**pFlag**
avg	33.80	10.15	0.59	39.49	0.35
std	6.80	0.03	0.01	0.20	0.02

Figure 3.15

	avg	std
pFlag	0.77	0.02
RIP2	128.67	1.81
N449D	18.43	1.10
N440R/D495R	36.88	0.10
N449R	282.17	8.04
D495R	181.16	7.50
N449D/D495R	237.33	0.77
	Avg/pFlag	Std/pFlag
E445R	10.90	0.14
Y474R	3.64	0.21
Q458E	7.09	0.17
E472R	1.91	0.00
R483D	2.13	0.05
pFlag	1.00	0.08
RIP2	110.38	2.39
R488E	2.06	0.04
R444E	3.79	0.11
N449D	18.09	1.14
D461R	2.61	0.09
D492K	1.93	0.04
R488E	2.67	0.03
K471D	1.56	0.08
E475R	1.90	0.03
Q497E	10.02	0.33
K513E	18.53	0.96

	Avg/pFlag	Std/pFlag
E445R	10.90	0.14
Q458E	7.09	0.17
E445R/Q458E	2.57	0.06
RIP2	110.38	2.39
pFlag	1.00	0.08

Figure 3.16

	iEDAP (ug/ml)				
	1	10	100	400	0
avg	1.42	3.90	5.60	6.34	1.00
std	0.73	0.79	0.86	1.02	0.00

References

Akira, S. and K. Takeda (2004). "Toll-like receptor signalling." Nature reviews immunology **4**(7): 499.

Aksentijevich, I., M. Nowak, M. Mallah, J. J. Chae, W. T. Watford, S. R. Hofmann, L. Stein, R. Russo, D. Goldsmith and P. Dent (2002). "De novo CIAS1 mutations, cytokine activation, and evidence for genetic heterogeneity in patients with neonatal-onset multisystem inflammatory disease (NOMID): a new member of the expanding family of pyrin-associated autoinflammatory diseases." Arthritis & Rheumatism **46**(12): 3340-3348.

Al-Amoudi, A., J. J. Chang, A. Leforestier, A. McDowall, L. M. Salamin, L. P. Norlen, K. Richter, N. S. Blanc, D. Studer and J. Dubochet (2004). "Cryo-electron microscopy of vitreous sections." The EMBO journal **23**(18): 3583-3588.

Albrecht, M., D. Choubey and T. Lengauer (2005). "The HIN domain of IFI-200 proteins consists of two OB folds." Biochemical and biophysical research communications **327**(3): 679-687.

Allen, I. C., J. E. Wilson, M. Schneider, J. D. Lich, R. A. Roberts, J. C. Arthur, R.-M. T. Woodford, B. K. Davis, J. M. Uronis and H. H. Herfarth (2012). "NLRP12 suppresses colon inflammation and tumorigenesis through the negative regulation of noncanonical NF-κB signaling." Immunity **36**(5): 742-754.

Allison, C. C., T. A. Kufer, E. Kremmer, M. Kaparakis and R. L. Ferrero (2009). "Helicobacter pylori induces MAPK phosphorylation and AP-1 activation via a NOD1-dependent mechanism." The Journal of Immunology **183**(12): 8099-8109.

Bai, X.-C., G. McMullan and S. H. Scheres (2015). "How cryo-EM is revolutionizing structural biology." Trends in biochemical sciences **40**(1): 49-57.

Banchereau, J. and R. M. Steinman (1998). "Dendritic cells and the control of immunity." Nature **392**(6673): 245.

Beck, G. and G. S. Habicht (1996). "Immunity and the invertebrates." Scientific American **275**(5): 60-66.

Benko, S., J. G. Magalhaes, D. J. Philpott and S. E. Girardin (2010). "NLRC5 limits the activation of inflammatory pathways." The Journal of Immunology **185**(3): 1681-1691.

Beroukhim, R. and N. Unwin (1997). "Distortion correction of tubular crystals: improvements in the acetylcholine receptor structure." Ultramicroscopy **70**(1-2): 57-81.

Bianchi, M. E. (2007). "DAMPs, PAMPs and alarmins: all we need to know about danger." Journal of leukocyte biology **81**(1): 1-5.

Blasius, A. L. and B. Beutler (2010). "Intracellular toll-like receptors." Immunity **32**(3): 305-315.

Boneca, I. G., O. Dussurget, D. Cabanes, M.-A. Nahori, S. Sousa, M. Lecuit, E. Psylinakis, V. Bouriotis, J.-P. Hugot and M. Giovannini (2007). "A critical role for peptidoglycan N-deacetylation in Listeria evasion from the host innate immune system." Proceedings of the National Academy of Sciences **104**(3): 997-1002.

Boyle, J. P., R. Parkhouse and T. P. Monie (2014). "Insights into the molecular basis of the NOD2 signalling pathway." Open biology **4**(12): 140178.

Brown, S. J. and L. Mayer (2007). "The immune response in inflammatory bowel disease." The American journal of gastroenterology **102**(9): 2058.

Brunette, R. L., J. M. Young, D. G. Whitley, I. E. Brodsky, H. S. Malik and D. B. Stetson (2012). "Extensive evolutionary and functional diversity among mammalian AIM2-like receptors." Journal of Experimental Medicine **209**(11): 1969-1983.

Bürckstümmer, T., C. Baumann, S. Blüml, E. Dixit, G. Dürnberger, H. Jahn, M. Planyavsky, M. Bilban, J. Colinge and K. L. Bennett (2009). "An orthogonal proteomic-genomic screen identifies AIM2 as a cytoplasmic DNA sensor for the inflammasome." Nature immunology **10**(3): 266.

Cadwell, K. (2016). "Crosstalk between autophagy and inflammatory signalling pathways: balancing defence and homeostasis." Nature reviews immunology **16**(11): 661.

Canna, S. W., A. A. de Jesus, S. Gouni, S. R. Brooks, B. Marrero, Y. Liu, M. A. DiMattia, K. J. Zaal, G. A. M. Sanchez and H. Kim (2014). "An activating NLRC4 inflammasome mutation causes autoinflammation with recurrent macrophage activation syndrome." Nature genetics **46**(10): 1140.

Cao, X. (2016). "Self-regulation and cross-regulation of pattern-recognition receptor signalling in health and disease." Nature reviews immunology **16**(1): 35.

Capra, J. D., C. A. Janeway, P. Travers and M. Walport (1999). Inmunobiology: the inmune system in health and disease, Garland Publishing.

Caruso, R., N. Warner, N. Inohara and G. Núñez (2014). "NOD1 and NOD2: signaling, host defense, and inflammatory disease." Immunity **41**(6): 898-908.

Celhar, T., R. Magalhaes and A.-M. Fairhurst (2012). "TLR7 and TLR9 in SLE: when sensing self goes wrong." Immunologic research **53**(1-3): 58-77.

Charnley, A. K., M. A. Convery, A. L. Shah, E. Jones, P. Hardwicke, A. Bridges, M. Ouellette, R. Totoritis, B. Schwartz and B. W. King (2015). "Crystal structures of human RIP2 kinase catalytic domain complexed with ATP-competitive inhibitors: Foundations for understanding inhibitor selectivity." Bioorganic & medicinal chemistry **23**(21): 7000-7006.

Chen, G., M. H. Shaw, Y.-G. Kim and G. Nuñez (2009). "NOD-like receptors: role in innate immunity and inflammatory disease." Annual Review of Pathological Mechanical Disease **4**: 365-398.

Coban, C., Y. Igari, M. Yagi, T. Reimer, S. Koyama, T. Aoshi, K. Ohata, T. Tsukui, F. Takeshita and K. Sakurai (2010). "Immunogenicity of whole-parasite vaccines against Plasmodium falciparum involves malarial hemozoin and host TLR9." Cell host & microbe **7**(1): 50-61.

Cui, Y., M. Li, K. D. Walton, K. Sun, J. A. Hanover, P. A. Furth and L. Hennighausen (2001). "The Stat3/5 locus encodes novel endoplasmic reticulum and helicase-like proteins that are preferentially expressed in normal and neoplastic mammary tissue." Genomics **78**(3): 129-134.

Dambuza, I. M. and G. D. Brown (2015). "C-type lectins in immunity: recent developments." Current opinion in immunology **32**: 21-27.

De Nardo, D. (2015). "Toll-like receptors: activation, signalling and transcriptional modulation." Cytokine **74**(2): 181-189.

De Rosier, D. and A. Klug (1968). "Reconstruction of three dimensional structures from electron micrographs." Nature **217**(5124): 130.

Deguine, J. and G. M. Barton (2014). "MyD88: a central player in innate immune signaling." F1000prime reports **6**.

Demkowicz, W. E., R. A. Littaua, J. Wang and F. A. Ennis (1996). "Human cytotoxic T-cell memory: long-lived responses to vaccinia virus." Journal of virology **70**(4): 2627-2631.

DeRosier, D. and P. Moore (1970). "Reconstruction of three-dimensional images from electron micrographs of structures with helical symmetry." Journal of molecular biology **52**(2): 355-369.

Diebolder, C. A., E. F. Halff, A. J. Koster, E. G. Huizinga and R. I. Koning (2015). "Cryoelectron tomography of the NAIP5/NLRC4 inflammasome: implications for NLR activation." Structure **23**(12): 2349-2357.

Ding, L., G. Dong, D. Zhang, Y. Ni and Y. Hou (2015). "The regional function of cGAS/STING signal in multiple organs: One of culprit behind systemic lupus erythematosus?" Medical hypotheses **85**(6): 846-849.

Dobbs, N., N. Burnaevskiy, D. Chen, V. K. Gonugunta, N. M. Alto and N. Yan (2015). "STING activation by translocation from the ER is associated with infection and autoinflammatory disease." Cell host & microbe **18**(2): 157-168.

Dobro, M. J., L. A. Melanson, G. J. Jensen and A. W. McDowall (2010). Plunge freezing for electron cryomicroscopy. Methods in enzymology, Elsevier. **481:** 63-82.

Dorsch, M., A. Wang, H. Cheng, C. Lu, A. Bielecki, K. Charron, K. Clauser, H. Ren, R. D. Polakiewicz and T. Parsons (2006). "Identification of a regulatory autophosphorylation site in the serine–threonine kinase RIP2." Cellular signalling **18**(12): 2223-2229.

Dos Santos, B., J. Valverde, P. Rohr, O. Monticielo, J. Brenol, R. Xavier and J. Chies (2012). "TLR7/8/9 polymorphisms and their associations in systemic lupus erythematosus patients from southern Brazil." Lupus **21**(3): 302-309.

Drickamer, K. (1988). "Two distinct classes of carbohydrate-recognition domains in animal lectins." J Biol Chem **263**(20): 9557-9560.

Dunne, A., N. A. Marshall and K. H. Mills (2011). "TLR based therapeutics." Current opinion in pharmacology **11**(4): 404-411.

Egelman, E. H. (2000). "A robust algorithm for the reconstruction of helical filaments using single-particle methods." Ultramicroscopy **85**(4): 225-234.

Egelman, E. H. (2015). "Three-dimensional reconstruction of helical polymers." Archives of biochemistry and biophysics **581**: 54-58.

Eisenbarth, S. C., A. Williams, O. R. Colegio, H. Meng, T. Strowig, A. Rongvaux, J. Henao-Mejia, C. A. Thaiss, S. Joly and D. G. Gonzalez (2012). "NLRP10 is a NOD-like receptor essential to initiate adaptive immunity by dendritic cells." Nature **484**(7395): 510.

Eley, T. C., K. Sugden, A. Corsico, A. M. Gregory, P. Sham, P. McGuffin, R. Plomin and I. W. Craig (2004). "Gene–environment interaction analysis of serotonin system markers with adolescent depression." Molecular psychiatry **9**(10): 908.

Ewald, S. E., B. L. Lee, L. Lau, K. E. Wickliffe, G.-P. Shi, H. A. Chapman and G. M. Barton (2008). "The ectodomain of Toll-like receptor 9 is cleaved to generate a functional receptor." Nature **456**(7222): 658.

Fairhurst, A. M., A. E. Wandstrat and E. K. Wakeland (2006). "Systemic lupus erythematosus: multiple immunological phenotypes in a complex genetic disease." Advances in immunology **92**: 1-69.

Feldmann, J. m., A.-M. Prieur, P. Quartier, P. Berquin, S. Certain, E. Cortis, D. Teillac-Hamel, A. Fischer and G. de Saint Basile (2002). "Chronic infantile neurological cutaneous and articular syndrome is caused by mutations in CIAS1, a gene highly expressed in polymorphonuclear cells and chondrocytes." The American Journal of Human Genetics **71**(1): 198-203.

Fernandes, R., C. Tsuda, A. L. Perumalsamy, T. Naranian, J. Chong, B. M. Acton, Z.-B. Tong, L. M. Nelson and A. Jurisicova (2012). "NLRP5 mediates mitochondrial function in mouse oocytes and embryos." Biology of reproduction **86**(5): 138, 131-110.

Fernandez-Leiro, R. and S. H. Scheres (2016). "Unravelling biological macromolecules with cryo-electron microscopy." Nature **537**(7620): 339.

Ferrao, R. and H. Wu (2012). "Helical assembly in the death domain (DD) superfamily." Current opinion in structural biology **22**(2): 241-247.

Fontalba, A., O. Gutierrez and J. L. Fernandez-Luna (2007). "NLRP2, an inhibitor of the NF-κB pathway, is transcriptionally activated by NF-κB and exhibits a nonfunctional allelic variant." The Journal of Immunology **179**(12): 8519-8524.

Franchi, L., N. Warner, K. Viani and G. Nuñez (2009). "Function of Nod-like receptors in microbial recognition and host defense." Immunological reviews **227**(1): 106-128.

Frank, J. (2009). "Single-particle reconstruction of biological macromolecules in electron microscopy–30 years." Quarterly reviews of biophysics **42**(3): 139-158.

Frank, J., J. Zhu, P. Penczek, Y. Li, S. Srivastava, A. Verschoor, M. Radermacher, R. Grassucci, R. K. Lata and R. K. Agrawal (1995). "A model of protein synthesis based on cryo-electron microscopy of the E. coli ribosome." Nature **376**(6539): 441.

Fridh, V. and K. Rittinger (2012). "The tandem CARDs of NOD2: intramolecular interactions and recognition of RIP2." PloS one **7**(3): e34375.

Fritz, J. H., L. Le Bourhis, G. Sellge, J. G. Magalhaes, H. Fsihi, T. A. Kufer, C. Collins, J. Viala, R. L. Ferrero and S. E. Girardin (2007). "Nod1-mediated innate immune recognition of peptidoglycan contributes to the onset of adaptive immunity." Immunity **26**(4): 445-459.

Goh, F. G. and K. S. Midwood (2011). "Intrinsic danger: activation of Toll-like receptors in rheumatoid arthritis." Rheumatology **51**(1): 7-23.

Gong, Q., Z. Long, F. L. Zhong, D. E. T. Teo, Y. Jin, Z. Yin, Z. Z. Boo, Y. Zhang, J. Zhang and R. Yang (2018). "Structural basis of RIP2 activation and signaling." Nature communications **9**(1): 4993.

Gong, Y.-N. and F. Shao (2012). "Sensing bacterial infections by NAIP receptors in NLRC4 inflammasome activation." Protein & cell **3**(2): 98-105.

Gordon, S. (2002). "Pattern recognition receptors: doubling up for the innate immune response." Cell **111**(7): 927-930.

Gray, E. E., D. Winship, J. M. Snyder, S. J. Child, A. P. Geballe and D. B. Stetson (2016). "The AIM2-like receptors are dispensable for the interferon response to intracellular DNA." Immunity **45**(2): 255-266.

Guiducci, C., M. Gong, A.-M. Cepika, Z. Xu, C. Tripodo, L. Bennett, C. Crain, P. Quartier, J. J. Cush and V. Pascual (2013). "RNA recognition by human TLR8 can lead to autoimmune inflammation." Journal of Experimental Medicine **210**(13): 2903-2919.

Hagar, J. A., D. A. Powell, Y. Aachoui, R. K. Ernst and E. A. Miao (2013). "Cytoplasmic LPS activates caspase-11: implications in TLR4-independent endotoxic shock." Science **341**(6151): 1250-1253.

Hasegawa, M., K. Yang, M. Hashimoto, J.-H. Park, Y.-G. Kim, Y. Fujimoto, G. Nuñez, K. Fukase and N. Inohara (2006). "Differential release and distribution of Nod1 and Nod2 immunostimulatory molecules among bacterial species and environments." Journal of Biological Chemistry **281**(39): 29054-29063.

Hashimoto, C., K. L. Hudson and K. V. Anderson (1988). "The Toll gene of Drosophila, required for dorsal-ventral embryonic polarity, appears to encode a transmembrane protein." Cell **52**(2): 269-279.

He, S. and S. H. Scheres (2017). "Helical reconstruction in RELION." Journal of structural biology **198**(3): 163-176.

He, X., S. Mekasha, N. Mavrogiorgos, K. A. Fitzgerald, E. Lien and R. R. Ingalls (2010). "Inflammation and fibrosis during Chlamydia pneumoniae infection is regulated by IL-1 and the NLRP3/ASC inflammasome." The Journal of Immunology **184**(10): 5743-5754.

Herrmann, M., R. E. Voll, O. M. Zoller, M. Hagenhofer, B. B. Ponner and J. R. Kalden (1998). "Impaired phagocytosis of apoptotic cell material by monocyte-derived macrophages from patients with systemic lupus erythematosus." Arthritis & Rheumatism **41**(7): 1241-1250.

Hibino, T., M. Loza-Coll, C. Messier, A. J. Majeske, A. H. Cohen, D. P. Terwilliger, K. M. Buckley, V. Brockton, S. V. Nair and K. Berney (2006). "The immune gene repertoire encoded in the purple sea urchin genome." Developmental biology **300**(1): 349-365.

Hoffman, H. M., J. L. Mueller, D. H. Broide, A. A. Wanderer and R. D. Kolodner (2001). "Mutation of a new gene encoding a putative pyrin-like protein causes familial cold autoinflammatory syndrome and Muckle–Wells syndrome." Nature genetics **29**(3): 301.

Hoving, J. C., G. J. Wilson and G. D. Brown (2014). "Signalling C-Type lectin receptors, microbial recognition and immunity." Cellular microbiology **16**(2): 185-194.

Hruz, P., A. S. Zinkernagel, G. Jenikova, G. J. Botwin, J.-P. Hugot, M. Karin, V. Nizet and L. Eckmann (2009). "NOD2 contributes to cutaneous defense against Staphylococcus aureus through α-toxin-dependent innate immune activation." Proceedings of the National Academy of Sciences **106**(31): 12873-12878.

Hu, Z., C. Yan, P. Liu, Z. Huang, R. Ma, C. Zhang, R. Wang, Y. Zhang, F. Martinon and D. Miao (2013). "Crystal structure of NLRC4 reveals its autoinhibition mechanism." Science **341**(6142): 172-175.

Humphreys, J., R. Beanland and P. J. Goodhew (2014). Electron microscopy and analysis, CRC Press.

Inohara, N., L. del Peso, T. Koseki, S. Chen and G. Núñez (1998). "RICK, a novel protein kinase containing a caspase recruitment domain, interacts with CLARP and regulates CD95-mediated apoptosis." Journal of Biological Chemistry **273**(20): 12296-12300.

Inohara, N. and G. Nuñez (2001). "The NOD: a signaling module that regulates apoptosis and host defense against pathogens." Oncogene **20**(44): 6473.

Inohara, N., Y. Ogura, A. Fontalba, O. Gutierrez, F. Pons, J. Crespo, K. Fukase, S. Inamura, S. Kusumoto and M. Hashimoto (2003). "Host recognition of bacterial Muramyl dipeptide

mediated through NOD2 IMPLICATIONS FOR CROHN′ S DISEASE." Journal of Biological Chemistry **278**(8): 5509-5512.

Janeway, C. A. (1989). Approaching the asymptote? Evolution and revolution in immunology. Cold Spring Harbor symposia on quantitative biology, Cold Spring Harbor Laboratory Press.

Janeway Jr, C. A. (1992). "The immune system evolved to discriminate infectious nonself from noninfectious self." Immunology today **13**(1): 11-16.

Jerne, N. K. (1973). "The immune system." Scientific American **229**(1): 52-63.

Jones, J. D. and J. L. Dangl (2006). "The plant immune system." Nature **444**(7117): 323.

Jounai, N., K. Kobiyama, M. Shiina, K. Ogata, K. J. Ishii and F. Takeshita (2011). "NLRP4 negatively regulates autophagic processes through an association with beclin1." The Journal of Immunology **186**(3): 1646-1655.

Kang, D.-c., R. V. Gopalkrishnan, Q. Wu, E. Jankowsky, A. M. Pyle and P. B. Fisher (2002). "mda-5: An interferon-inducible putative RNA helicase with double-stranded RNA-dependent ATPase activity and melanoma growth-suppressive properties." Proceedings of the National Academy of Sciences **99**(2): 637-642.

Kato, H., K. Takahasi and T. Fujita (2011). "RIG-I-like receptors: cytoplasmic sensors for non-self RNA." Immunological reviews **243**(1): 91-98.

Kawai, T. and S. Akira (2010). "The role of pattern-recognition receptors in innate immunity: update on Toll-like receptors." Nature immunology **11**(5): 373.

Kawai, T. and S. Akira (2010). "The role of pattern-recognition receptors in innate immunity: update on Toll-like receptors." Nature immunology **11**(5): 373-384.

Keestra-Gounder, A. M., M. X. Byndloss, N. Seyffert, B. M. Young, A. Chávez-Arroyo, A. Y. Tsai, S. A. Cevallos, M. G. Winter, O. H. Pham and C. R. Tiffany (2016). "NOD1 and NOD2 signalling links ER stress with inflammation." Nature **532**(7599): 394.

Khare, S., A. Dorfleutner, N. B. Bryan, C. Yun, A. D. Radian, L. de Almeida, Y. Rojanasakul and C. Stehlik (2012). "An NLRP7-containing inflammasome mediates recognition of microbial lipopeptides in human macrophages." Immunity **36**(3): 464-476.

Kilpatrick, D. C. (2002). "Animal lectins: a historical introduction and overview." Biochimica et Biophysica Acta (BBA)-General Subjects **1572**(2-3): 187-197.

Kim, J. G., S. J. Lee and M. F. Kagnoff (2004). "Nod1 is an essential signal transducer in intestinal epithelial cells infected with bacteria that avoid recognition by toll-like receptors." Infection and immunity **72**(3): 1487-1495.

Kim, M. L., H. G. Jeong, C. A. Kasper and C. Arrieumerlou (2010). "IKKα contributes to canonical NF-κB activation downstream of Nod1-mediated peptidoglycan recognition." PloS one **5**(10): e15371.

Kim, Y.-G., N. Kamada, M. H. Shaw, N. Warner, G. Y. Chen, L. Franchi and G. Núñez (2011). "The Nod2 sensor promotes intestinal pathogen eradication via the chemokine CCL2-dependent recruitment of inflammatory monocytes." Immunity **34**(5): 769-780.

Kim, Y.-G., J.-H. Park, M. H. Shaw, L. Franchi, N. Inohara and G. Núñez (2008). "The cytosolic sensors Nod1 and Nod2 are critical for bacterial recognition and host defense after exposure to Toll-like receptor ligands." Immunity **28**(2): 246-257.

Kim, Y. K., J.-S. Shin and M. H. Nahm (2016). "NOD-like receptors in infection, immunity, and diseases." Yonsei medical journal **57**(1): 5-14.

Kingsmore, S. F., J. Snoddy, D. Choubey, P. Lengyel and M. F. Seldin (1989). "Physical mapping of a family of interferon-activated genes, serum amyloid P-component, and α-spectrin on mouse chromosome 1." Immunogenetics **30**(3): 169-174.

Kitamura, A., Y. Sasaki, T. Abe, H. Kano and K. Yasutomo (2014). "An inherited mutation in NLRC4 causes autoinflammation in human and mice." Journal of Experimental Medicine **211**(12): 2385-2396.

Kobayashi, K., N. Inohara, L. D. Hernandez, J. E. Galán, G. Núñez, C. A. Janeway, R. Medzhitov and R. A. Flavell (2002). "RICK/Rip2/CARDIAK mediates signalling for receptors of the innate and adaptive immune systems." Nature **416**(6877): 194.

Koblansky, A. A., D. Jankovic, H. Oh, S. Hieny, W. Sungnak, R. Mathur, M. S. Hayden, S. Akira, A. Sher and S. Ghosh (2013). "Recognition of profilin by Toll-like receptor 12 is critical for host resistance to Toxoplasma gondii." Immunity **38**(1): 119-130.

Kofoed, E. M. and R. E. Vance (2011). "Innate immune recognition of bacterial ligands by NAIPs determines inflammasome specificity." Nature **477**(7366): 592.

Komuro, A. and C. M. Horvath (2006). "RNA-and virus-independent inhibition of antiviral signaling by RNA helicase LGP2." Journal of virology **80**(24): 12332-12342.

Kopp, E. B. and S. Ghosh (1995). "NF-kB and Rel proteins in innate immunity." Advances in immunology **58**(1).

Krumeich, F. (2011). "Properties of electrons, their interactions with matter and applications in electron microscopy." Laboratory of Inorganic Chemistry, disponível em http://www. microscopy. ethz. ch/downloads/Interactions. pdf, consultado em: 3-08.

Kruse, K., C. Janko, V. Urbonaviciute, C. T. Mierke, T. H. Winkler, R. E. Voll, G. Schett, L. E. Munoz and M. Herrmann (2010). "Inefficient clearance of dying cells in patients with SLE: anti-dsDNA autoantibodies, MFG-E8, HMGB-1 and other players." Apoptosis **15**(9): 1098-1113.

Kwon, D., J. H. Yoon, S.-Y. Shin, T.-H. Jang, H.-G. Kim, I. So, J.-H. Jeon and H. H. Park (2011). "A comprehensive manually curated protein–protein interaction database for the Death Domain superfamily." Nucleic acids research **40**(D1): D331-D336.

Laing, K. J., M. K. Purcell, J. R. Winton and J. D. Hansen (2008). "A genomic view of the NOD-like receptor family in teleost fish: identification of a novel NLR subfamily in zebrafish." BMC evolutionary biology **8**(1): 42.

Laroui, H., Y. Yan, Y. Narui, S. A. Ingersoll, S. Ayyadurai, M. A. Charania, F. Zhou, B. Wang, K. Salaita and S. V. Sitaraman (2011). "L-Ala-γ-D-Glu-meso-diaminopimelic acid (DAP) interacts directly with leucine-rich region domain of nucleotide-binding oligomerization domain 1, increasing phosphorylation activity of receptor-interacting serine/threonine-protein kinase 2 and its interaction with nucleotide-binding oligomerization domain 1." Journal of Biological Chemistry **286**(35): 31003-31013.

Lemaitre, B., E. Nicolas, L. Michaut, J.-M. Reichhart and J. A. Hoffmann (1996). "The dorsoventral regulatory gene cassette spätzle/Toll/cactus controls the potent antifungal response in Drosophila adults." Cell **86**(6): 973-983.

Levinsohn, J. L., Z. L. Newman, K. A. Hellmich, R. Fattah, M. A. Getz, S. Liu, I. Sastalla, S. H. Leppla and M. Moayeri (2012). "Anthrax lethal factor cleavage of Nlrp1 is required for activation of the inflammasome." PLoS pathogens **8**(3): e1002638.

Li, Q. and I. M. Verma (2002). "NF-κB regulation in the immune system." Nature reviews immunology **2**(10): 725.

Li, T., J. Chen and I. M. Cristea (2013). "Human cytomegalovirus tegument protein pUL83 inhibits IFI16-mediated DNA sensing for immune evasion." Cell host & microbe **14**(5): 591-599.

Li, X.-D. and Z. J. Chen (2012). "Sequence specific detection of bacterial 23S ribosomal RNA by TLR13." Elife **1**: e00102.

Li, Y., T.-M. Fu, A. Lu, K. Witt, J. Ruan, C. Shen and H. Wu (2018). "Cryo-EM structures of ASC and NLRC4 CARD filaments reveal a unified mechanism of nucleation and activation of caspase-1." Proceedings of the National Academy of Sciences **115**(43): 10845-10852.

Lin, S.-C., Y.-C. Lo and H. Wu (2010). "Helical assembly in the MyD88–IRAK4–IRAK2 complex in TLR/IL-1R signalling." Nature **465**(7300): 885.

Lin, Z., J. Y. Tann, E. T. Goh, C. Kelly, K. B. Lim, J. F. Gao and C. F. Ibanez (2015). "Structural basis of death domain signaling in the p75 neurotrophin receptor." Elife **4**: e11692.

Lu, A., V. G. Magupalli, J. Ruan, Q. Yin, M. K. Atianand, M. R. Vos, G. F. Schroder, K. A. Fitzgerald, H. Wu and E. H. Egelman (2014). "Unified polymerization mechanism for the assembly of ASC-dependent inflammasomes." Cell **156**(6): 1193-1206.

Ludtke, S. J., P. R. Baldwin and W. Chiu (1999). "EMAN: semiautomated software for high-resolution single-particle reconstructions." Journal of structural biology **128**(1): 82-97.

Maekawa, S., U. Ohto, T. Shibata, K. Miyake and T. Shimizu (2016). "Crystal structure of NOD2 and its implications in human disease." Nature communications **7**: 11813.

Magalhaes, J. G., J. H. Fritz, L. Le Bourhis, G. Sellge, L. H. Travassos, T. Selvanantham, S. E. Girardin, J. L. Gommerman and D. J. Philpott (2008). "Nod2-dependent Th2 polarization of antigen-specific immunity." The Journal of Immunology **181**(11): 7925-7935.

Maharana, J., B. Dehury, J. R. Sahoo, I. Jena, A. Bej, D. Panda, B. R. Sahoo, M. C. Patra and S. K. Pradhan (2015). "Structural and functional insights into CARDs of zebrafish (Danio rerio) NOD1 and NOD2, and their interaction with adaptor protein RIP2." Molecular Biosystems **11**(8): 2324-2336.

Maharana, J., S. K. Pradhan and S. De (2017). "NOD1CARD might be using multiple interfaces for RIP2-mediated CARD-CARD interaction: insights from molecular dynamics simulation." PloS one **12**(1): e0170232.

Man, S. M. and T.-D. Kanneganti (2016). "Converging roles of caspases in inflammasome activation, cell death and innate immunity." Nature reviews immunology **16**(1): 7.

Mariathasan, S., K. Newton, D. M. Monack, D. Vucic, D. M. French, W. P. Lee, M. Roose-Girma, S. Erickson and V. M. Dixit (2004). "Differential activation of the inflammasome by caspase-1 adaptors ASC and Ipaf." Nature **430**(6996): 213.

Masumoto, J., K. Yang, S. Varambally, M. Hasegawa, S. A. Tomlins, S. Qiu, Y. Fujimoto, A. Kawasaki, S. J. Foster and Y. Horie (2006). "Nod1 acts as an intracellular receptor to stimulate chemokine production and neutrophil recruitment in vivo." Journal of Experimental Medicine **203**(1): 203-213.

Mayle, S., J. P. Boyle, E. Sekine, B. Zurek, T. A. Kufer and T. P. Monie (2014). "Engagement of nucleotide-binding oligomerization domain-containing protein 1 (NOD1) by receptor-interacting protein 2 (RIP2) is insufficient for signal transduction." Journal of Biological Chemistry **289**(33): 22900-22914.

McCarthy, J. V., J. Ni and V. M. Dixit (1998). "RIP2 is a novel NF-κB-activating and cell death-inducing kinase." Journal of Biological Chemistry **273**(27): 16968-16975.

Medzhitov, R. (2001). "Toll-like receptors and innate immunity." Nature reviews immunology **1**(2): 135.

Medzhitov, R. and C. Janeway Jr (2000). "Innate immunity." New England Journal of Medicine **343**(5): 338-344.

Medzhitov, R. and C. A. Janeway Jr (1997). "Innate immunity: impact on the adaptive immune response." Current opinion in immunology **9**(1): 4-9.

Medzhitov, R., P. Preston-Hurlburt and C. A. Janeway Jr (1997). "A human homologue of the Drosophila Toll protein signals activation of adaptive immunity." Nature **388**(6640): 394.

Meylan, E., J. Tschopp and M. Karin (2006). "Intracellular pattern recognition receptors in the host response." Nature **442**(7098): 39.

Miao, E. A., C. M. Alpuche-Aranda, M. Dors, A. E. Clark, M. W. Bader, S. I. Miller and A. Aderem (2006). "Cytoplasmic flagellin activates caspase-1 and secretion of interleukin 1β via Ipaf." Nature immunology **7**(6): 569.

Miao, E. A., D. P. Mao, N. Yudkovsky, R. Bonneau, C. G. Lorang, S. E. Warren, I. A. Leaf and A. Aderem (2010). "Innate immune detection of the type III secretion apparatus through the NLRC4 inflammasome." Proceedings of the National Academy of Sciences **107**(7): 3076-3080.

Milne, J. L., M. J. Borgnia, A. Bartesaghi, E. E. Tran, L. A. Earl, D. M. Schauder, J. Lengyel, J. Pierson, A. Patwardhan and S. Subramaniam (2013). "Cryo-electron microscopy–a primer for the non-microscopist." The FEBS journal **280**(1): 28-45.

Moore, C. B., D. T. Bergstralh, J. A. Duncan, Y. Lei, T. E. Morrison, A. G. Zimmermann, M. A. Accavitti-Loper, V. J. Madden, L. Sun and Z. Ye (2008). "NLRX1 is a regulator of mitochondrial antiviral immunity." Nature **451**(7178): 573.

Motta, V., F. Soares, T. Sun and D. J. Philpott (2015). "NOD-like receptors: versatile cytosolic sentinels." Physiological reviews **95**(1): 149-178.

Nakamura, N., J. R. Lill, Q. Phung, Z. Jiang, C. Bakalarski, A. de Maziere, J. Klumperman, M. Schlatter, L. Delamarre and I. Mellman (2014). "Endosomes are specialized platforms for bacterial sensing and NOD2 signalling." Nature **509**(7499): 240.

Nanson, J. D., M. H. Rahaman, T. Ve and B. Kobe (2018). Regulation of signaling by cooperative assembly formation in mammalian innate immunity signalosomes by molecular mimics. Seminars in cell & developmental biology, Elsevier.

Ogura, Y., N. Inohara, A. Benito, F. F. Chen, S. Yamaoka and G. Núñez (2001). "Nod2, a Nod1/Apaf-1 family member that is restricted to monocytes and activates NF-κB." Journal of Biological Chemistry **276**(7): 4812-4818.

Ogura, Y., S. Lala, W. Xin, E. Smith, T. Dowds, F. Chen, E. Zimmermann, M. Tretiakova, J. Cho and J. Hart (2003). "Expression of NOD2 in Paneth cells: a possible link to Crohn's ileitis." Gut **52**(11): 1591-1597.

Onoguchi, K., M. Yoneyama and T. Fujita (2011). "Retinoic acid-inducible gene-I-like receptors." Journal of Interferon & Cytokine Research **31**(1): 27-31.

Palm, N. W. and R. Medzhitov (2009). "Pattern recognition receptors and control of adaptive immunity." Immunological reviews **227**(1): 221-233.

Pandey, A. K., Y. Yang, Z. Jiang, S. M. Fortune, F. Coulombe, M. A. Behr, K. A. Fitzgerald, C. M. Sassetti and M. A. Kelliher (2009). "NOD2, RIP2 and IRF5 play a critical role in the type I interferon response to Mycobacterium tuberculosis." PLoS pathogens **5**(7): e1000500.

Pandey, S., T. Kawai and S. Akira (2015). "Microbial sensing by Toll-like receptors and intracellular nucleic acid sensors." Cold Spring Harbor perspectives in biology **7**(1): a016246.

Park, H. H., Y.-C. Lo, S.-C. Lin, L. Wang, J. K. Yang and H. Wu (2007). "The death domain superfamily in intracellular signaling of apoptosis and inflammation." Annual review of immunology **25**.

Park, H. H., E. Logette, S. Raunser, S. Cuenin, T. Walz, J. Tschopp and H. Wu (2007). "Death domain assembly mechanism revealed by crystal structure of the oligomeric PIDDosome core complex." Cell **128**(3): 533-546.

Park, J.-H., Y.-G. Kim, M. Shaw, T.-D. Kanneganti, Y. Fujimoto, K. Fukase, N. Inohara and G. Núñez (2007). "Nod1/RICK and TLR signaling regulate chemokine and antimicrobial innate immune responses in mesothelial cells." The Journal of Immunology **179**(1): 514-521.

Peng, H., B. Chang, C. Lu, J. Su, Y. Wu, P. Lv, Y. Wang, J. Liu, B. Zhang and F. Quan (2012). "Nlrp2, a maternal effect gene required for early embryonic development in the mouse." PloS one **7**(1): e30344.

Poltorak, A., X. He, I. Smirnova, M.-Y. Liu, C. Van Huffel, X. Du, D. Birdwell, E. Alejos, M. Silva and C. Galanos (1998). "Defective LPS signaling in C3H/HeJ and C57BL/10ScCr mice: mutations in Tlr4 gene." Science **282**(5396): 2085-2088.

Poyet, J.-L., S. M. Srinivasula, M. Tnani, M. Razmara, T. Fernandes-Alnemri and E. S. Alnemri (2001). "Identification of Ipaf, a human caspase-1-activating protein related to Apaf-1." Journal of Biological Chemistry **276**(30): 28309-28313.

Proell, M., S. J. Riedl, J. H. Fritz, A. M. Rojas and R. Schwarzenbacher (2008). "The Nod-like receptor (NLR) family: a tale of similarities and differences." PloS one **3**(4): e2119.

Qin, H., S. M. Srinivasula, G. Wu, T. Fernandes-Alnemri, E. S. Alnemri and Y. Shi (1999). "Structural basis of procaspase-9 recruitment by the apoptotic protease-activating factor 1." Nature **399**(6736): 549.

Qu, Y., S. Misaghi, A. Izrael-Tomasevic, K. Newton, L. L. Gilmour, M. Lamkanfi, S. Louie, N. Kayagaki, J. Liu and L. Kömüves (2012). "Phosphorylation of NLRC4 is critical for inflammasome activation." Nature **490**(7421): 539.

Rathinam, V. A., S. K. Vanaja and K. A. Fitzgerald (2012). "Regulation of inflammasome signaling." Nature immunology **13**(4): 333.

Regan, T., K. Nally, R. Carmody, A. Houston, F. Shanahan, J. MacSharry and E. Brint (2013). "Identification of TLR10 as a key mediator of the inflammatory response to Listeria monocytogenes in intestinal epithelial cells and macrophages." The Journal of Immunology **191**(12): 6084-6092.

Rock, F. L., G. Hardiman, J. C. Timans, R. A. Kastelein and J. F. Bazan (1998). "A family of human receptors structurally related to Drosophila Toll." Proceedings of the National Academy of Sciences **95**(2): 588-593.

Rogero, M. M. and P. C. Calder (2018). "Obesity, inflammation, toll-like receptor 4 and fatty acids." Nutrients **10**(4): 432.

Romberg, N., K. Al Moussawi, C. Nelson-Williams, A. L. Stiegler, E. Loring, M. Choi, J. Overton, E. Meffre, M. K. Khokha and A. J. Huttner (2014). "Mutation of NLRC4 causes a syndrome of enterocolitis and autoinflammation." Nature genetics **46**(10): 1135.

Rothenfusser, S., N. Goutagny, G. DiPerna, M. Gong, B. G. Monks, A. Schoenemeyer, M. Yamamoto, S. Akira and K. A. Fitzgerald (2005). "The RNA helicase Lgp2 inhibits TLR-independent sensing of viral replication by retinoic acid-inducible gene-I." The Journal of Immunology **175**(8): 5260-5268.

Scheres, S. H. (2012). "RELION: implementation of a Bayesian approach to cryo-EM structure determination." Journal of structural biology **180**(3): 519-530.

Schneider, M., A. G. Zimmermann, R. A. Roberts, L. Zhang, K. V. Swanson, H. Wen, B. K. Davis, I. C. Allen, E. K. Holl and Z. Ye (2012). "The innate immune sensor NLRC3 attenuates Toll-like receptor signaling via modification of the signaling adaptor TRAF6 and transcription factor NF-κB." Nature immunology **13**(9): 823.

Seger, R. and E. G. Krebs (1995). "The MAPK signaling cascade." The FASEB journal **9**(9): 726-735.

Shatsky, M., R. J. Hall, E. Nogales, J. Malik and S. E. Brenner (2010). "Automated multi-model reconstruction from single-particle electron microscopy data." Journal of structural biology **170**(1): 98-108.

Sigworth, F. J. (2016). "Principles of cryo-EM single-particle image processing." Microscopy **65**(1): 57-67.

Srinivasula, S. M., J.-L. Poyet, M. Razmara, P. Datta, Z. Zhang and E. S. Alnemri (2002). "The PYRIN-CARD protein ASC is an activating adaptor for caspase-1." Journal of Biological Chemistry **277**(24): 21119-21122.

Stark, H., F. Mueller, E. V. Orlova, M. Schatz, P. Dube, T. Erdemir, F. Zemlin, R. Brimacombe and M. van Heel (1995). "The 70S Escherichia coli ribosome at 23 Å resolution: fitting the ribosomal RNA." Structure **3**(8): 815-821.

Sun, L., J. Wu, F. Du, X. Chen and Z. J. Chen (2013). "Cyclic GMP-AMP synthase is a cytosolic DNA sensor that activates the type I interferon pathway." Science **339**(6121): 786-791.

Sun, Y. (1997). "RIG-I, a homolog gene of RNA helicase, is induced by retinoic acid during the differentiation of acute promyelocytic leukemia cell. Thesis, Shanhai Institute of Heamatology, Rui-Jin Hospital, Shanghai Second Medical University." Gene Bank accession number AF038963.

Sutterwala, F. S., L. A. Mijares, L. Li, Y. Ogura, B. I. Kazmierczak and R. A. Flavell (2007). "Immune recognition of Pseudomonas aeruginosa mediated by the IPAF/NLRC4 inflammasome." Journal of Experimental Medicine **204**(13): 3235-3245.

Suzuki, S., L. Franchi, Y. He, R. Muñoz-Planillo, H. Mimuro, T. Suzuki, C. Sasakawa and G. Núñez (2014). "Shigella type III secretion protein MxiI is recognized by Naip2 to induce Nlrc4 inflammasome activation independently of Pkcδ." PLoS pathogens **10**(2): e1003926.

Takeuchi, O. and S. Akira (2010). "Pattern recognition receptors and inflammation." Cell **140**(6): 805-820.

Thay, B., A. Damm, T. A. Kufer, S. N. Wai and J. Oscarsson (2014). "Aggregatibacter actinomycetemcomitans outer membrane vesicles are internalized in human host cells and trigger NOD1-and NOD2-dependent NF-κB activation." Infection and immunity **82**(10): 4034-4046.

Thome, M., K. Hofmann, K. Burns, F. Martinon, J.-L. Bodmer, C. Mattmann and J. Tschopp (1998). "Identification of CARDIAK, a RIP-like kinase that associates with caspase-1." Current Biology **8**(15): 885-889.

Tigno-Aranjuez, J. T., J. M. Asara and D. W. Abbott (2010). "Inhibition of RIP2's tyrosine kinase activity limits NOD2-driven cytokine responses." Genes & development **24**(23): 2666-2677.

Ting, J. P.-Y., R. C. Lovering, E. S. Alnemri, J. Bertin, J. M. Boss, B. K. Davis, R. A. Flavell, S. E. Girardin, A. Godzik and J. A. Harton (2008). "The NLR gene family: a standard nomenclature." Immunity **28**(3): 285-287.

Travassos, L. H., L. A. Carneiro, M. Ramjeet, S. Hussey, Y.-G. Kim, J. G. Magalhães, L. Yuan, F. Soares, E. Chea and L. Le Bourhis (2010). "Nod1 and Nod2 direct autophagy by recruiting ATG16L1 to the plasma membrane at the site of bacterial entry." Nature immunology **11**(1): 55.

Unterholzner, L. and A. G. Bowie (2011). "Innate DNA sensing moves to the nucleus." Cell host & microbe **9**(5): 351-353.

Vance, R. E. (2015). "The NAIP/NLRC4 inflammasomes." Current opinion in immunology **32**: 84-89.

Vasseur, E., M. Boniotto, E. Patin, G. Laval, H. Quach, J. Manry, B. Crouau-Roy and L. Quintana-Murci (2012). "The evolutionary landscape of cytosolic microbial sensors in humans." The American Journal of Human Genetics **91**(1): 27-37.

Vasseur, F., B. Sendid, T. Jouault, A. Standaert-Vitse, L. Dubuquoy, N. Francois, C. Gower-Rousseau, P. Desreumaux, F. Broly and S. Vermeire (2011). "Variants of NOD1 and NOD2 genes display opposite associations with familial risk of Crohn's disease and anti-saccharomyces cerevisiae antibody levels." Inflammatory bowel diseases **18**(3): 430-438.

Venkataraman, T., M. Valdes, R. Elsby, S. Kakuta, G. Caceres, S. Saijo, Y. Iwakura and G. N. Barber (2007). "Loss of DExD/H box RNA helicase LGP2 manifests disparate antiviral responses." The Journal of Immunology **178**(10): 6444-6455.

Ver Heul, A. M., L. Gakhar, R. C. Piper and R. Subramanian (2014). "Crystal structure of a complex of NOD1 CARD and ubiquitin." PloS one **9**(8): e104017.

Wang, P., S. Zhu, L. Yang, S. Cui, W. Pan, R. Jackson, Y. Zheng, A. Rongvaux, Q. Sun and G. Yang (2015). "Nlrp6 regulates intestinal antiviral innate immunity." Science **350**(6262): 826-830.

Weber, C. H. and C. Vincenz (2001). "The death domain superfamily: a tale of two interfaces?" Trends in biochemical sciences **26**(8): 475-481.

Williams, D. B. and C. B. Carter (1996). The transmission electron microscope. Transmission electron microscopy, Springer**:** 3-17.

Wu, B. and S. Hur (2015). "How RIG-I like receptors activate MAVS." Current opinion in virology **12**: 91-98.

Wu, B., A. Peisley, D. Tetrault, Z. Li, E. H. Egelman, K. E. Magor, T. Walz, P. A. Penczek and S. Hur (2014). "Molecular imprinting as a signal-activation mechanism of the viral RNA sensor RIG-I." Molecular cell **55**(4): 511-523.

Wu, C., Z. Su, M. Lin, J. Ou, W. Zhao, J. Cui and R.-F. Wang (2017). "NLRP11 attenuates Toll-like receptor signalling by targeting TRAF6 for degradation via the ubiquitin ligase RNF19A." Nature communications **8**(1): 1977.

Wu, J., T. Fernandes-Alnemri and E. S. Alnemri (2010). "Involvement of the AIM2, NLRC4, and NLRP3 inflammasomes in caspase-1 activation by Listeria monocytogenes." Journal of clinical immunology **30**(5): 693-702.

Wu, J., L. Sun, X. Chen, F. Du, H. Shi, C. Chen and Z. J. Chen (2013). "Cyclic GMP-AMP is an endogenous second messenger in innate immune signaling by cytosolic DNA." Science **339**(6121): 826-830.

Wu, Y.-w., W. Tang and J.-p. Zuo (2015). "Toll-like receptors: potential targets for lupus treatment." Acta Pharmacologica Sinica **36**(12): 1395.

Xiao, T., P. Towb, S. A. Wasserman and S. R. Sprang (1999). "Three-dimensional structure of a complex between the death domains of Pelle and Tube." Cell **99**(5): 545-555.

Xiao, T. S. and K. A. Fitzgerald (2013). "The cGAS-STING pathway for DNA sensing." Molecular cell **51**(2): 135-139.

Yamamoto, M., S. Sato, H. Hemmi, K. Hoshino, T. Kaisho, H. Sanjo, O. Takeuchi, M. Sugiyama, M. Okabe and K. Takeda (2003). "Role of adaptor TRIF in the MyD88-independent toll-like receptor signaling pathway." Science **301**(5633): 640-643.

Yang, J., Y. Zhao, J. Shi and F. Shao (2013). "Human NAIP and mouse NAIP1 recognize bacterial type III secretion needle protein for inflammasome activation." Proceedings of the National Academy of Sciences **110**(35): 14408-14413.

Yang, S., B. Wang, F. Humphries, R. Jackson, M. E. Healy, R. Bergin, G. Aviello, B. Hall, D. McNamara and T. Darby (2013). "Pellino3 ubiquitinates RIP2 and mediates Nod2-induced signaling and protective effects in colitis." Nature immunology **14**(9): 927.

Yarovinsky, F., D. Zhang, J. F. Andersen, G. L. Bannenberg, C. N. Serhan, M. S. Hayden, S. Hieny, F. S. Sutterwala, R. A. Flavell and S. Ghosh (2005). "TLR11 activation of dendritic cells by a protozoan profilin-like protein." Science **308**(5728): 1626-1629.

Yin, Q., Y. Tian, V. Kabaleeswaran, X. Jiang, D. Tu, M. J. Eck, Z. J. Chen and H. Wu (2012). "Cyclic di-GMP sensing via the innate immune signaling protein STING." Molecular cell **46**(6): 735-745.

Yoneyama, M. and T. Fujita (2009). "RNA recognition and signal transduction by RIG-I-like receptors." Immunological reviews **227**(1): 54-65.

Yoneyama, M., M. Kikuchi, K. Matsumoto, T. Imaizumi, M. Miyagishi, K. Taira, E. Foy, Y.-M. Loo, M. Gale and S. Akira (2005). "Shared and unique functions of the DExD/H-box helicases RIG-I, MDA5, and LGP2 in antiviral innate immunity." The Journal of Immunology **175**(5): 2851-2858.

Yoneyama, M., M. Kikuchi, T. Natsukawa, N. Shinobu, T. Imaizumi, M. Miyagishi, K. Taira, S. Akira and T. Fujita (2004). "The RNA helicase RIG-I has an essential function in double-stranded RNA-induced innate antiviral responses." Nature immunology **5**(7): 730.

Yu, G., R. Yan, C. Zhang, C. Mao and W. Jiang (2015). "Single-Particle Cryo-EM and 3D Reconstruction of Hybrid Nanoparticles with Electron-Dense Components." Small **11**(38): 5157-5163.

Zelensky, A. N. and J. E. Gready (2005). "The C-type lectin-like domain superfamily." The FEBS journal **272**(24): 6179-6217.

Zhang, L., S. Chen, J. Ruan, J. Wu, A. B. Tong, Q. Yin, Y. Li, L. David, A. Lu and W. L. Wang (2015). "Cryo-EM structure of the activated NAIP2-NLRC4 inflammasome reveals nucleated polymerization." Science: aac5789.

Zhang, W.-H., X. Wang, M. Narayanan, Y. Zhang, C. Huo, J. C. Reed and R. M. Friedlander (2003). "Fundamental role of the Rip2/caspase-1 pathway in hypoxia and ischemia-induced neuronal cell death." Proceedings of the National Academy of Sciences **100**(26): 16012-16017.

Zhang, X., C. Wang, L. B. Schook, R. J. Hawken and M. S. Rutherford (2000). "An RNA helicase, RHIV-1, induced by porcine reproductive and respiratory syndrome virus (PRRSV) is mapped on porcine chromosome 10q13." Microbial pathogenesis **28**(5): 267-278.

Zhang, X., J. Wu, F. Du, H. Xu, L. Sun, Z. Chen, C. A. Brautigam, X. Zhang and Z. J. Chen (2014). "The cytosolic DNA sensor cGAS forms an oligomeric complex with DNA and undergoes switch-like conformational changes in the activation loop." Cell reports **6**(3): 421-430.

Zhao, Y., J. Yang, J. Shi, Y.-N. Gong, Q. Lu, H. Xu, L. Liu and F. Shao (2011). "The NLRC4 inflammasome receptors for bacterial flagellin and type III secretion apparatus." Nature **477**(7366): 596.

Zhou, R., A. S. Yazdi, P. Menu and J. Tschopp (2011). "A role for mitochondria in NLRP3 inflammasome activation." Nature **469**(7329): 221.